INFORMATION TO USERS

This manuscript has been reproduced from the microfilm master. UMI films the text directly from the original or copy submitted. Thus, some thesis and dissertation copies are in typewriter face, while others may be from any type of computer printer.

The quality of this reproduction is dependent upon the quality of the copy submitted. Broken or indistinct print, colored or poor quality illustrations and photographs, print bleedthrough, substandard margins, and improper alignment can adversely affect reproduction.

In the unlikely event that the author did not send UMI a complete manuscript and there are missing pages, these will be noted. Also, if unauthorized copyright material had to be removed, a note will indicate the deletion.

Oversize materials (e.g., maps, drawings, charts) are reproduced by sectioning the original, beginning at the upper left-hand corner and continuing from left to right in equal sections with small overlaps. Each original is also photographed in one exposure and is included in reduced form at the back of the book.

Photographs included in the original manuscript have been reproduced xerographically in this copy. Higher quality 6" x 9" black and white photographic prints are available for any photographs or illustrations appearing in this copy for an additional charge. Contact UMI directly to order.

UMI®

Bell & Howell Information and Learning
300 North Zeeb Road, Ann Arbor, MI 48106-1346 USA
800-521-0600

Simulation of 3-D Viscous Compressible Flow in Multistage Turbomachinery by Finite Element Methods

Mohamad Sleiman

A Thesis
in
The Department
of
Mechanical Engineering

Presented in Partial Fulfillment of the Requirements
for the Degree of Doctor of Philosophy at
Concordia University
Montreal, Quebec, Canada

April 1999

ABSTRACT

Simulation of 3-D Viscous Compressible Flow in Multistage Turbomachinery by Finite Element Methods

Mohamad Sleiman, Ph.D.
Concordia University, 1999

The flow in a multistage turbomachinery blade row is compressible, viscous, and unsteady. Complex flow features such as boundary layers, wake migration from upstream blade rows, shocks, tip leakage jets, and vortices interact together as the flow convects through the stages. These interactions contribute significantly to the aerodynamic losses of the system and degrade the performance of the machine. The unsteadiness also leads to blade vibration and a shortening of its life. It is therefore difficult to optimize the design of a blade row, whether aerodynamically or structurally, in isolation, without accounting for the effects of the upstream and downstream rows. The effects of axial spacing, blade count, clocking (relative position of follow-up rotors with respect to wakes shed by upstream ones), and levels of unsteadiness may have a significance on performance and durability.

In this Thesis, finite element formulations for the simulation of multistage turbomachinery are presented in terms of the Reynolds-averaged Navier-Stokes equations for three-dimensional steady or unsteady, viscous, compressible, turbulent flows. Three methodologies are presented and compared.

First, a steady multistage analysis using a mixing-plane model has been implemented and has been validated against engine data. For axial machines, it has been found that the mixing plane simulation methods match very well the experimental data. However, the results for a centrifugal stage, consisting of an impeller followed by a vane diffuser of equal pitch, show flagrant inconsistency with engine performance data, indicating that the mixing plane method has been found to be inappropriate for centrifugal machines.

Following these findings, a more complete unsteady multistage model has been devised for a configuration with equal number of rotor and stator blades (equal pitches). Non-matching grids are used at the rotor-stator interface and an implicit interpolation procedure devised to ensure continuity of fluxes across. This permits the rotor and stator equations to be solved in a fully-coupled manner, allowing larger time steps in attaining a time-periodic solution. This equal pitch approach has been validated on the complex geometry of a centrifugal stage.

Finally, for a stage configuration with unequal pitches, the time-inclined method, developed by Giles (1991) for 2-D viscous compressible flow, has been extended to 3-D and formulated in terms of the physical solution vector U, rather than Q, a non-physical one. The method has been evaluated for unsteady flow through a rotor blade passage of the power turbine of a turboprop.

Acknowledgments

I would first like to offer my special thanks and appreciation to Dr. Wagdi Habashi for serving as my Thesis Supervisor. His continuous technical advice, bright ideas, and sense of humor have made my years of studies fruitful and interesting.

My Thesis was carried out at Pratt & Whitney Canada (PWC). I would thus like to express my gratitude to all members of PWC's CFD group, for their helpful technical expertise and many suggestions. In particular, I would like to thank Dr. Djaffar Ait-Ali-Yahia, Martin Peeters and my Thesis co-supervisor, Dr. Michel Robichaud, who assisted me while carrying out my research at PWC. I would also like to thank my dearest friend and co-worker, Dr. Anna Tam, who made laughter part of my daily life at PWC.

I would like to take this opportunity to thank my family, Hussein, Taghrid, Ali, Nader, Louma, Samer, and Nagham for their continuous encouragement during my studies.

Last but not least, I would like to express my deep appreciation to my wife, Dareen Sleiman, for her support, patience and words of encouragement during my graduate studies.

This Thesis is dedicated to my wife, Dareen, who brought joy and happiness to my life ever since I met her.

Table of Contents

List of Figures

List of Tables

Nomenclature

C_p C_v	coefficient of pressure
Ec	Eckert number
e	approximation error
el	element
E	total number of elements
F	'mixed out' fluxes
H_o	stagnation enthalpy
k	thermal conductivity
L	reference length
L_2	L-2 residual norm
M	Mach number
M_θ	circumferential Mach number
M_w	Wheel Mach number
N	finite element shape function
p	pressure
P	blade pitch
Pr	Prandtl number
Q	tilted solution vector
r, θ, z	Cylindrical coordinates
R	gas constant
$\Re$	real numbers
Re	Reynolds number
Res	residual of a differential equation
Sr	Strouhal Number

t	time
T	static temperature
	blade-passing period
T_o	stagnation temperature
u, v, w	Cartesian velocity components
u_r, u_θ, u_z	Cylindrical velocity components
$\mathbf{U}$	Solution vector
$\bar{V}$	velocity vector
V	finite dimensional space
W	Galerkin weight function
$\vec{x}$	position vector of global coordinates
x, y, z	Cartesian coordinates

Greek Symbols

$\vec{\xi}$	position vector of local coordinates
ξ, η, ζ	non-dimensional local coordinates of element
∇	gradient operator
Δ	change in a variable between iterations
Δt	time-step
ΔT	time-lag in periodicity boundary condition
γ	ratio of specific heats
Γ	boundary of Ω
λ	pressure dissipation coefficient
	time-tilting parameter
μ	viscosity
μ_{art}	artificial dissipation coefficient for momentum equations
Ω	domain in $\Re^n$

	rotational speed
ρ	density
ϕ	unknown finite element variable
σ_{ij}	viscous stress tensor

Subscripts

∞	free stream conditions
h	mesh size parameter
i, j	row, column indices

Superscripts

e	elemental quantity
n	Newton iteration number
t	time level

1. Introduction

The flow fields of compressors and turbines in gas turbine engines are quite complex and can only be fully described by unsteady, viscous, and turbulent models. Complex flow features such as boundary layers, wake migration from upstream blade rows, shocks, tip leakage jets, and vortices interact together as the flow convects through the stages. These interactions contribute significantly to the aerodynamic losses of the system and degrade the performance of the machine. It is therefore difficult to optimize the design of a blade row in isolation, without accounting for the effects of the upstream and downstream blade rows.

Aircraft gas turbine engines are designed with two conflicting objectives: low weight and compact size, and high performance and durability. In view of such design objectives, the unsteady nature of the flow field and multistage effects become important considerations in the design process, especially if small, incremental gains in aerodynamic performance are to be attained. Over the past two decades, research efforts by gas turbine engine manufacturers have concentrated on the use of experimental testing as well as computational fluid dynamics to study the flow phenomena within a blade row passage embedded in a multistage environment.

In the following sections, various methods for the computation of steady and unsteady flow in a multistage configuration are described.

1.1 Sources of Unsteadiness in Turbomachinery

The unsteady nature of turbomachinery flow stems from various sources. An understanding of these sources of unsteadiness brings an appreciation of the major difficulties encountered in resolving such complex flows.

The first source of unsteadiness to be considered is due to the interaction of potential fields [1,2]. This inviscid effect is based on the relative motion of blade rows with different fields of lift force. These fields interact in time and primarily affect the flow pattern in the gap region. As shown in figure 1.1, the potential field interaction generated by the stator is felt as an unsteady flow by the downstream rotor and, conversely, the potential field interaction generated by a rotor is felt as an unsteady flow by the upstream stator. These fluctuating forces on blades and vanes are arguably the most obvious unsteady effects in multi-row turbomachines, and they are clearly of great importance from an aeroelastic viewpoint.

Viscous boundary layers, wakes and secondary flows, which all propagate in time across the downstream airfoils, comprise another leading source of unsteadiness. Flow around airfoils creates a total pressure wake which is persistent in time. As the wake leaves the airfoils, it typically compromises a zone of about 1/20th the width of a blade passage, having zero velocity at its center.

Unsteadiness also causes the forced vibration/flutter phenomenon in which a small oscillation of the blade/fan produces an unsteady force and moment on the blade.

Finally, other major sources of unsteadiness are due to the inlet flow variations in time, occurring mainly during takeoff, rotating stall and surge.

1.2 Steady Rotor-Stator Interaction

1.2.1 Through-Flow Method

The Through-Flow method assumes that the flow is steady and represents an interaction between separate 3-D solution domains for individual blade rows and an axisymmetric 2-D (through-flow) plane covering the whole turbomachine. The 3-D effect of the flow is introduced by circumferential averaging of the 3-D equations [3,4]. Although the flow in every blade row is supposed to be linked to an axisymmetric average model, the axisymmetric model for one turbomachine should be unique. For a multi-row machine, the through-flow solution is used to obtain the necessary boundary conditions for individual blade row 3-D solutions while the 3D solutions are used to incorporate loss modeling and blockage effects into the through-flow. Although the scheme has moderate computer requirements, it smears the transport of flow features between blade rows and lacks the complete effect of multistage environment representation while solving for one blade row.

1.2.2 Mixing Plane Method

The Mixing Plane method is seen as an improvement to the through-flow approach, although it retains the steady flow assumption. This method couples the 3-D solutions of adjacent blade rows by averaging, at an inter-row mixing plane, the quantities necessary for conservation laws and then passing them axisymmetrically to the adjacent blade row [5]. The averaging procedure is applied to the exit-plane of the upstream blade row and to the inlet plane of the downstream blade row to extract the so-called "mixed out" flow properties from

the numerical solution [6]. In this approach, the proper interface boundary conditions are specified. Circumferentially-averaged radial profiles of absolute total temperature, density, radial velocity, absolute tangential velocity and axial velocity, obtained from the solution of the upstream blade row, are specified at the inlet plane of the downstream blade row. The circumferentially "mixed out" static pressure, obtained from the solution of the downstream blade row, is then specified at the exit plane of the upstream blade row. The above procedure is repeated at every Newton iteration until the equations are appropriately converged, and the mass flow rate and the circumferentially-averaged radial profiles, obtained from the upstream and downstream blade rows, are matched within a user-specified tolerance [7]. The advantages of this method include its ability to represent a multistage environment, while solving for an individual blade row at a time and the iterative determination, rather than sequential imposition, of inter-row boundary conditions.

1.2.3 Average-Passage Flow Method

The Average-Passage Flow approach considers a time-averaged flow field, over a time interval which ensures temporal periodicity, as seen by an observer whose frame of reference is fixed with respect to a given blade row [8-9]. Relative to an individual blade row's frame of reference, a 3-D solution is defined which represents the domain of the whole turbomachine. The effect of unsteadiness due to other blade rows is accounted for using time and space averaging. Since Euler or Navier-Stokes equations are nonlinear, the time-averaging will include a correlation between time varying flow variables. This correlation represents the effect of unsteadiness on the time-averaged solution and constitutes, with body forces, energy sources and the space-averaging correlation, the closure requirements for the average-passage equations. The average-passage model is

derived by applying three averaging operators to the governing equations: ensemble-averaging, time-averaging and "passage-to-passage" averaging. Ensemble-averaging the Navier-Stokes equations yields the familiar Reynolds-Averaged Navier-Stokes equations. After time-averaging, the periodic unsteadiness in the flow field is filtered out. Finally, "passage-to-passage" averaging is applied to account for the spatially aperiodic components of the flow field [8]. As a result of these averaging procedures, the so-called "deterministic stresses" term appears in the passage-average Navier-Stokes equations.

In contrast to the mixing plane approach, in which the exit plane of the upstream blade row and the inlet plane of the downstream blade row are located at the same axial position, the passage averaging approach uses an overlap between the grids of the upstream and the downstream blade rows to account for body forces and deterministic stresses [8].

The advantage of the average-passage scheme is that temporally and spatially averaged equations are solved on a steady basis and the solution is intended to represent the total effect of all other blade rows. The disadvantages of this method include the complexity and rising cost for multistage cases, as well as the uncertainty concerning the correlation models.

1.3 Fully Unsteady Rotor-Stator Interaction

The simulation of the unsteady flow phenomena present in turbomachinery stages requires fine grids to resolve flow features with very small time scales and to accurately capture turbulence. Such computations are characterized by their

high demand of computer memory and solution time. To reduce their cost, the state of the art description of the flowfield is currently as follows:

- unsteady phenomena occurring at high time frequencies are unresolved
- unsteady interactions between wakes and laminar-turbulent boundary layers are not accounted for in the turbulence modeling
- computations are carried out with the minimum number of rotor and stator passages

In the fully unsteady approach, the time-dependent Reynolds-Averaged Navier-Stokes equations are solved throughout the computational domain, comprising all rotors and stators, with no averaging of flow properties at any interface planes shared by rotor and stator rows. The time-accurate flow properties are communicated via an interpolation procedure which is applied at such interfaces. Although the advantage of the approach lies in the fact that no closure requirements are involved, it is expensive in terms of computing time and memory [10]. This, however, is the most realistic approach and its drawbacks will quickly disappear with the advent of powerful computers.

1.3.1 Flow Periodicity in the Gap Region

The flow field in the gap region, between successive rotor and stator rows, can be described as a function of its spatial and temporal periodicity. To investigate the various time frequencies present in complex single stage configurations, one should consider first the simplified case of inviscid flows, which neglect the unsteady interactions caused by viscous phenomena.

For equal pitches, the flow solution vector U on the upper periodic boundary is identical to that on the lower periodic boundary at the same time, that is,

$$U(r,\theta,z,t) = U(r,\theta+\frac{2\pi}{N},z,t) \tag{1.1}$$

However, a lagged periodic boundary condition is required for unequal pitches. This can be easily understood by viewing figure 1.2, which depicts the stator-rotor configuration at two different instances in time, t=0 and $t=\Delta T$. The relative position of stator2/rotor2 at time $t=\Delta T$ is identical to the relative position of stator1/rotor1 at a previous time t=0. A similar relationship to (1.1) can then be defined, using the time periodicity based on the absolute difference between pitch distances. Thus, the flow solution on the upper periodic boundary at time $t=\Delta T$ is identical to that on the lower periodic boundary at time t=0, that is,

$$U(r,\theta,z,t) = U(r,\theta+\frac{2\pi}{N},z,t+\Delta T) \tag{1.2}$$

$$\Delta T = T_R - T_S = \frac{\theta_R - \theta_S}{\Omega} \tag{1.3}$$

where ΔT is the time lag,

T_R and T_S are the blade-passing periods,

θ_R and θ_S are the pitch angles,

Ω is the angular speed of the rotor.

This description of periodicity in a single stage configuration has been based only on geometric and constant parameters such as blade count and angular speed.

Therefore, it can only describe the periodicity associated with inviscid or potential unsteady interaction. Viscous flow phenomena, however, interact in time and drastically affect the flow field in the gap region. A mathematical description of the unsteady viscous interactions and their corresponding time frequencies is quite difficult to formulate and achieve [6].

1.3.2 Single-Stage Configuration with Equal Pitches

The special case of a single stage configuration with equal blade count, shown in figure 1.3, has been resolved by Gundy-Burlet [11]. However, such a simple configuration, common for hydraulic compressors, blowers, turbines or fans, seldom occur in aircraft applications. Due to the spatial periodicity of the flow solution, the computational domain may encompass only a single blade-to-blade passage. Along the periodic boundaries, a rotation periodic boundary condition may be imposed, as in references [12,13]. The flow solution vector U along line (ab) is identical to the flow solution along line (cd) or vice-versa. The solution is then interpolated and interchangeably used across the interface.

1.3.3 Single-Stage Configuration with Unequal Pitches

In a single stage configuration with unequal pitches, the flow solution vector U does not possess a single blade-to-blade passage periodicity (fig. 1.4). At the expense of extremely large memory requirement and solution time, a complete numerical description of the flow field can be obtained by solving for the entire stage geometry (360° or full annulus). To circumvent this problem, various numerical techniques have been developed to recover the spatial periodicity on a truncated computational domain, using corrected boundary conditions along the periodic boundaries and the sliding interface.

The truncated computational domain contains K_i blade passages for both rotor and stator rows. Using equation (1.2), the boundary conditions along the periodic surfaces can then be defined as

$$U_i(r,\theta,z,t) = U_i(r,\theta+\frac{2\pi K_i}{N_i},z,t+\Delta T_i) \tag{1.3}$$

The next section describes the boundary condition requirements for a "reduced" or truncated computational domain.

1.3.4 Boundary Conditions

For a single-stage configuration, the following boundary conditions may be imposed to uniquely define the unsteady flow on a truncated computational domain:

- At inlet boundary, the flow is assumed to be steady and the total pressure, total temperature and flow angles are specified
- Along the airfoil surface, the no-penetration and no-slip conditions are imposed
- At the exit boundary, the flow may be described by using the radial equilibrium equation, imposing a constant exit static pressure, or imposing a constant mass flow
- The use of a truncated computational domain requires that special treatment of boundary conditions along the sliding interface and the free or "spatially periodic" boundaries, as shown in figure 1.1.

The next section describes the various methods used for the computation of the flow field through a single turbomachinery stage with unequal pitches.

1.3.5 Domain Scaling Method

The time periodicity term of the flow solution vector U is present only for cases with unequal pitches ($N_1 \neq N_2$). The approach taken in the domain scaling method eliminates this time periodicity term by using multiple blade passages with integers K_1 and K_2 such that $\frac{N_1}{K_1} = \frac{N_2}{K_2}$. In doing so, equation (1.3) becomes identical to equation (1.1). A case with blade counts $N_1 = 12$ and $N_2 = 4$ would require the computational domain to have $K_1 = 3$ and $K_2 = 1$ blade passages.

When the blade count of the first row is not a multiple of the blade count of the second, integers are then chosen such that $\frac{N_1}{K_1}$ is very close to $\frac{N_2}{K_2}$, and K_1 and K_2 are kept small compared to N_1 and N_2 so as to reduce memory and solution time. Spatial periodicity of the flow is recovered by scaling the geometry of each blade row by $\frac{N_i}{K_i}$. The pitch-to-chord ratio is kept identical in order to maintain same blade loading. The scaling procedure results in equal circumferential distances on each side of the interface.

The domain scaling method is applied to a stator-rotor configuration in figure 1.4. Figure (1.4a) shows the truncated computational domain consisting of one blade passage on the stator side $K_1 = 1$ and two blade passages on the rotor side $K_2 = 2$. The scaled rotor geometry is presented in figure (1.4b) and the distance covered by two rotor pitches is now identical to that of one stator pitch. At each time step t, the required boundary conditions become:

- The flow solution vector U along the periodic segment (ab) is identical to that along the periodic segment (ef).
- Segment (cd) is shared by rotors 1 and 2 and, hence, has identical boundary conditions
- The conservation of flow variables U should be imposed across the interface, which connects surfaces forming a non-conforming domain.

This methodology has been used by Rai [14,15], who studied a turbine stage with $N_1 = 22$ stator blades and $N_2 = 28$ rotor blades ($\frac{N_1}{N_2} = 0.79$). He assumed that only 22 rotor airfoils were present in the stage geometry. Thus, he scaled the rotor geometry by a factor $\frac{N_2}{K_2} = \frac{28}{22}$ and solved for only one blade passage on either side of the interface. The accuracy of the flow solution obviously depends on the difference between the two ratios. At the expense of larger solution time and memory requirements, Rai and Madavan [16] and Sharma [17] both improved the accuracy of the flow solution obtained earlier by Rai., using a computational domain with $K_1 = 3$ stator and $K_2 = 4$ rotor blades $\frac{K_1}{K_2} = 0.75$.

The Domain Scaling method has been used primarily for two-dimensional flow problems. Its extension to three-dimensions is not trivial, as the variation of radius along hub and shroud boundaries makes the geometry scaling difficult to achieve. Other applications of the methodology have been carried out by Dawes [18], Kelecy [19], Micklow [20], McConnaughey and Griffin [21], Rangwalla [22], and Gundy-Burlet [11].

1.3.6 Gradient Scaling Method

In contrast to the domain scaling method, in which the scaling is applied to the geometry of the computational domain, the approach undertaken in the gradient scaling method applies the scaling to the azimutal gradients of the flow solution vector U. Fourmaux [23], Lemeur [24], Paulon [25] and Billonnet [26] have all used the gradient scaling method, with multiple blade channels K_1 and K_2.

The application of gradient scaling methodology is shown in figure 1.5, using the computational domain presented earlier in figure 1.4. The proper flow information is exchanged across the interface, line (ag) of stator row and line (ae) of rotor row, using a surface interpolation algorithm. The gradient of the primary aerodynamic quantities, along a constant radius at the interface, remains tangentially proportional to the angular sector of the domain under consideration.

The key features of the gradient scaling method may be summarized as follows:

- The gradients of the flow variables are scaled at the interface
- The solution accuracy is improved when $\frac{N_1}{K_1}$ is close to $\frac{N_2}{K_2}$
- Interpolation of flow quantities is required for the exchange of flow information across the interface; and simple rotation periodicity is imposed along the periodic segments
- This technique may be easily extended to multiple rows.

1.3.7 Direct Storage Method

The direct storage technique assumes explicitly that the flow solution vector U is both periodic in time and space in order to define the proper boundary conditions to be applied to the truncated computational domain. As indicated in

figure 1.6, the flow solution, at any particular passage at an instant in time t, is related to the flow solution in another passage at an earlier time.

Erdos [27] and Koya and Kotake [28] used this numerical technique in which the flow solution in the dummy cells of a given periodic boundary is interpolated from the flow solution of the first inner cells of the connected periodic boundary, with a flow solution that was stored at a previous time. In order to resolve only one blade passage for either the stator or rotor sides, the interface boundary is treated in a manner similar to the periodic boundaries. Dummy cells, which overlap the interface surface in the axial direction, are used and the flow solution is saved on either side of the boundary for at least one blade passing period of the row containing the maximum number of blades. The treatment of a two-dimensional interface boundary by the direct storage method is described in [28].

This method requires large data storage for three-dimensional flow applications. The use of boundary data from an earlier time on the opposite periodic surface may also delay the convergence to the unsteady flow solution [29]. In fact, the direct storage method directly imposes that the flow is periodic in time, with a period based uniquely on the blade passing frequency. This treatment of periodic boundary conditions may not be appropriate for viscous flows where unsteady phenomena may occur, at various time frequencies, simultaneously.

1.3.8 Chorochronic Periodicity Method

The chorochronic periodicity method was first proposed by He [30,31] and, He and Denton [32], as having reduced memory requirements compared to the direct storage method.

Along each side of the interface, the flow solution vector is expanded in a double Fourier series for time and spatial periodicity. Since most of the Fourier coefficients are zero, with the space-time periodicity condition, the double summations can be performed with reduced computing time. Momentum and flow conservation at the interface are expressed in terms of Fourier coefficients. In contrast to the direct storage method, at each time increment the Fourier coefficients are stored instead of the flow solution vector U, thus reducing the demands on memory.

The chorochronic periodicity method was generalized for the treatment of the interface boundary by Gerolymos [33], who investigated a test case with 25 Fourier coefficients on each side of the interface.

1.3.9 Time-Inclined Method (TIM)

The time-inclined methodology (fig. 1.7) has been defined by Giles [34] and implemented for rotor-stator flow simulations by Giles and Haimes [35], Jung [36,37] and Stetter [38].

The following reversible time-space variable transformation, shown below,

$$\begin{aligned} r' &= r \\ \theta' &= \theta \\ z' &= z \\ t' &= t - \lambda\theta \end{aligned} \tag{1.4}$$

$$\lambda = \begin{cases} \dfrac{\Delta T}{\theta_S} & \text{stator} \\ \dfrac{\Delta T}{\theta_R} & \text{rotor} \end{cases} \tag{1.5}$$

is applied to each side of the interface. It should be remarked that equation (1.1) is satisfied since the space and time periodicity are expressed directly in the transformation of equation (1.4). The governing flow equations must also be transformed using equation (1.4), yielding for inviscid flows the following expressions:

$$\frac{\partial}{\partial t'}(Q)+\frac{1}{r'}\frac{\partial}{\partial r'}(r'A)+\frac{1}{r'}\frac{\partial}{\partial \theta'}(B)+\frac{\partial}{\partial r'}(C)+\frac{D}{r'}=0 \tag{1.6}$$

$$Q = U-\frac{\lambda}{r}B \tag{1.7}$$

For inviscid flow computations, the vector of conservative flow variables U can be obtained from Q in closed form [39]. However, for viscous flow computations, the vector U cannot be computed from Q since it now includes viscous stress terms. These viscous stress terms are simply neglected in the work of all authors of this method and are comparable in magnitude to those usually neglected in the thin shear-layer Navier-Stokes equations under the high Reynolds number condition.

The time-inclined method can be easily programmed but may only be applied in cases of a single stage. The solution of equations (1.6-1.7) is subject to the following constraint:

$$1-\frac{M_w}{1-M_\theta}\le\frac{\theta_S}{\theta_R}\le 1+\frac{M_w}{1+M_\theta} \tag{1.8}$$

where M_w is the wheel Mach number,

M_θ is the circumferential Mach number

Therefore, stator-rotor configurations with a large difference in their pitch distances cannot be simulated using a single blade passage on either side of the interface.

At the interface boundary, Giles [34], Giles and Haimes [35] and Eulitz [40] considered separate grids for both the rotor and stator parts, and connected them by a one-cell layer. At each time step, each stator grid node along the interface is connected to the nearest grid node from the rotor side boundary, thus forming a cell layer between the two grids. On each grid, the flow solution is computed using local grid-relative variables. Along the interface cell layer, however, all flow variables are converted back to the stator frame of reference, and their basic Lax-Wendroff scheme is modified to consider the shearing of the computational cells. This shearing may, however, produce inaccurate flow solutions. In Jung [36,37] and Stetter [38], a sliding surface is considered with two layers of dummy cells along the axial direction.

1.4 Literature Review

Considerable effort has been devoted to the calculation of unsteady flows in turbomachines. The first significant piece of work was conducted by Erdos in 1977 [27]. In his paper, Erdos presented a calculation of unsteady flow in a fan stage in which he used an algorithm to treat unequal pitches. Unfortunately, this method has some limitations for the assumption of periodicity in time. The method also requires a considerable amount of storage. In 1985, Koya extended Erdos' work to three dimensions [28]. In 1984, Hodson modified a program written by Denton, and then applied Erdos' technique, to calculate wake/rotor interactions in a low speed turbine [41]. The incoming wakes were specified as unsteady boundary conditions. The results reveal that the wake segments, cut by

the turbine rotors, roll up into two counter-rotating passage vortices, and the wake fluid migrates to the suction surface. In 1987, Rai presented a paper on using a Navier-Stokes algorithm to compute the stator/rotor interaction [14]. This paper generated considerable interest and research activity in this field. In 1989, Rai extended his techniques to three-dimensional, viscous calculations [15]. However, Rai, as well as other researchers, assumed a stator/rotor pitch ratio of 1:1 or other simple ratios such as 2:3 or 3:4. Such assumptions allow them to perform calculations with simple periodic boundary conditions, but require that modifications be made to the geometry when applied to actual turbomachinery stages.

There have been much work in this area of research: Fourmaux [42] and Lewis [43], on inviscid, two-dimensional stator/rotor interaction; Jorgensen [44] on viscous, quasi-three-dimensional stator/rotor interaction; Ni [17], on inviscid three-dimensional stator/rotor interaction; and Chen [45], on three-dimensional, viscous stator/rotor interaction.

In 1990, Giles [34] introduced a new method for the two-dimensional computation of unsteady flow through a turbine stage with unequal pitches. He transformed the governing equations from the physical time into the computation time and, therefore, dramatically simplified the periodicity boundary condition on free boundaries. In 1996, Jung and Stetter [36,37,38] extended Giles work into three-dimensions and considered a 1 ½ stage turbine with equal blade count for both stators.

1.5 Objectives and Overview of Thesis

The objective of this Thesis is to develop a capability for the analysis of viscous, compressible, and turbulent flows and solve for the steady and unsteady blade row interaction in a gas turbine engine. In this Thesis, fully implicit finite element formulations for the simulation of multistage turbomachinery have been developed in terms of the Reynolds-averaged Navier-Stokes equations for three-dimensional steady or unsteady, viscous, compressible, turbulent flows [46].

The first contribution of this Thesis is the finite element implementation of a mixing plane model for the analysis of steady flow in axial and centrifugal turbomachinery stages and its validation against available engine data. The mixing plane method represents an intermediate milestone between existing finite element based through-flow axisymmetric codes and the fully unsteady multistage approach, based on the Navier-Stokes equations, requiring enormous computer resources. The mixing plane method has also been used to build loss correlations for the calibration of the through-flow code. While this methodology is extensively used as a powerful analysis tool by the gas turbine community, there is little work published on its validation and application to centrifugal stages. In this work, it has been found that for axial machines, the mixing plane simulation methods match very well the experimental data. However, the results for a centrifugal stage, consisting of an impeller and a vane diffuser of equal pitch, show flagrant inconsistency with engine performance data, indicating that the mixing plane method may be inappropriate for centrifugal machines. This represents a significant contribution of this Thesis.

Consequently, a fully implicit finite element method, which treats non-matching grids at the rotor-stator interface, has been developed and implemented for the

analysis of the unsteady flow in multistage turbomachiners with equal number of blades and vanes. The solution vector U, for momentum vector and pressure field, on rotor and stator grids, is solved simultaneously. The implicit approach, characterized by its superior convergence rate compared to other approaches Erdos [27], Giles [6], and Jung [36,37], is another contribution of this Thesis. It permits the use of a high time-step and hence drastically reduces the computing time required to achieve a time periodic solution. An interpolation procedure at the rotor-stator interface, consistent with the matrix assembly of the governing flow equations, has been developed to ensure continuity of solutions across the interface. The time accuracy of the methodology has been validated against the flow past a circular cylinder at Re=100, and demonstrated on a centrifugal stage, comprising of an impeller followed by a vane diffuser.

Another contribution of the Thesis is the implementation of a time-inclined computational method for the analysis of the unsteady flow in a single turbomachinery stage with unequal number of rotor and stator blades. This method, based on the 2-D viscous compressible work of Giles [6], has been implemented and validated for 3-D viscous flows. In contrast to Giles, the method developed in this Thesis is implicit, uses mismatched grids at interfaces, and is formulated in terms of the physical solution vector U, as opposed to Q, a non-physical variable. The time-inclined U formulation inherits all the properties of the fully implicit equal pitches formulation but has the added advantage of being able, within limits, to handle a stage with arbitrary blade count. The coupling of the time-inclined approach together with the use of mismatched grids at interfaces, and the implicit treatment of the interface, are major offerings of this Thesis. The method has been evaluated on unsteady flow through a rotor blade passage of the power turbine of a turboprop engine. A post-processor

based on Fourier transform theory has been developed to map the finite element solution from the computational space into the physical space.

The work of this Thesis has been embedded in *NS3D*, an efficient, three-dimensional finite element code for the analysis of inviscid and viscous compressible flows, which has been developed by PWC with Concordia University.

The second chapter of the Thesis describes the numerical discretization of the governing Reynolds-Averaged Navier-Stokes equations. The finite element equations, which are based on a Streamwise Upwind Petrov-Galerkin formulation, are derived.

The third chapter describes the mixing plane methodology for the analysis of steady flow in multistage turbomachinery. This is followed by a detailed description of the treatment of the interface region for unsteady flow through a single turbomachinery stage with (a) equal rotor and stator pitches, and (b) unequal rotor and stator pitches.

The fourth chapter on solution procedure provides details of the flow solver algorithm as well as the coupling of the solver with the multistage methods for the analysis of steady and unsteady flows.

The fifth chapter presents validation test cases for the multistage methodology. For all cases, solutions are analyzed and compared to experimental and/or other numerical results.

The sixth and final chapter states the conclusions of the Thesis and discusses future research work.

FIGURES

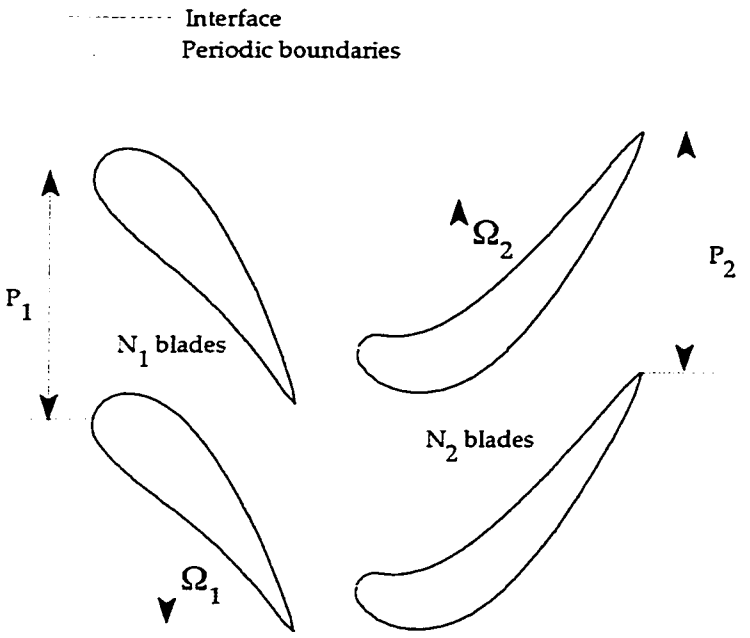

Figure 1.1 Single stage configuration in turbomachinery

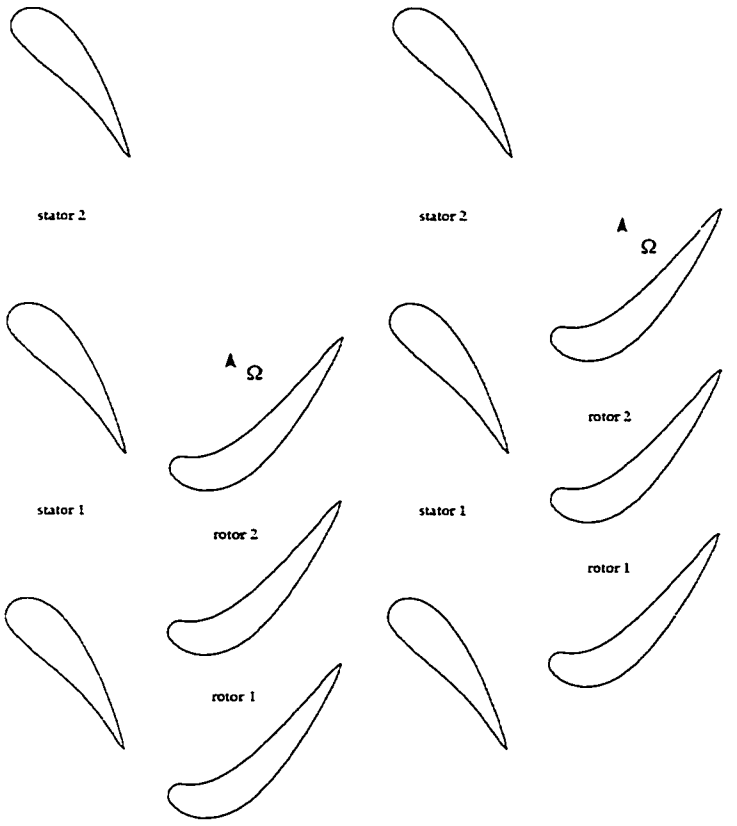

Figure 1.2 Stator-rotor stage configuration at (a) $t = 0$ and (b) $t = \Delta t$

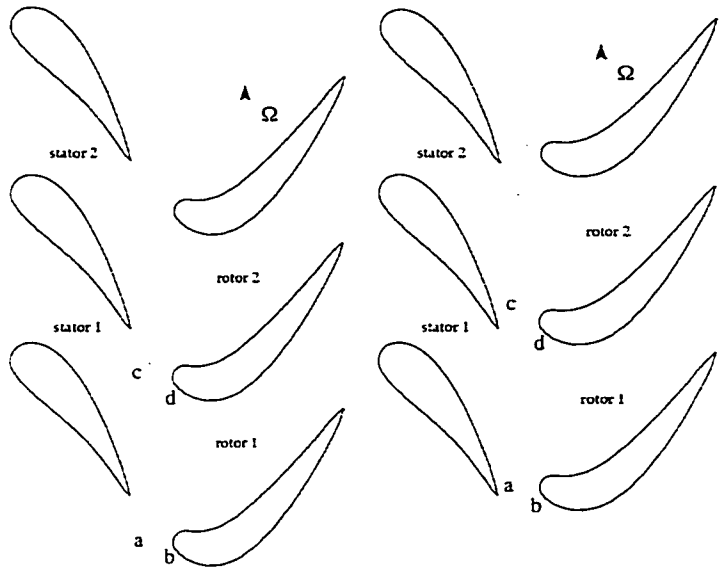

Figure 1.3 Single stage configuration in with equal pitches

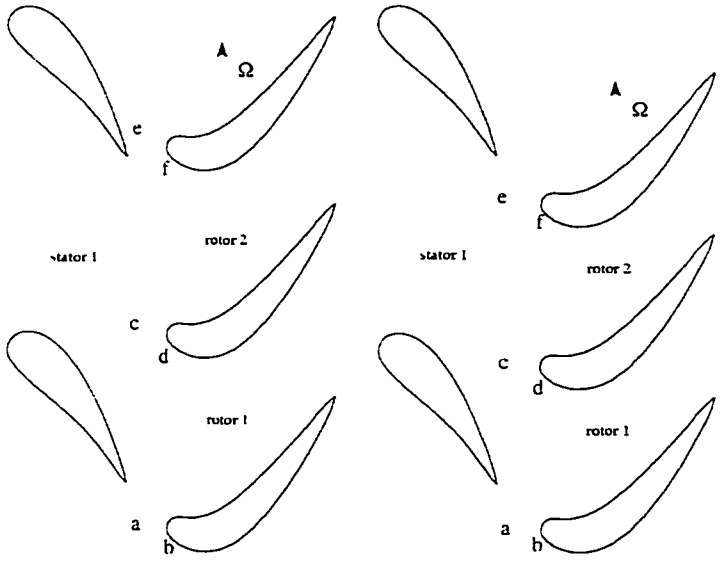

Figure 1.4 Domain scaling method applied to a single stage configuration with unequal pitches; (a) actual geometry, (b) scaled rotor geometry

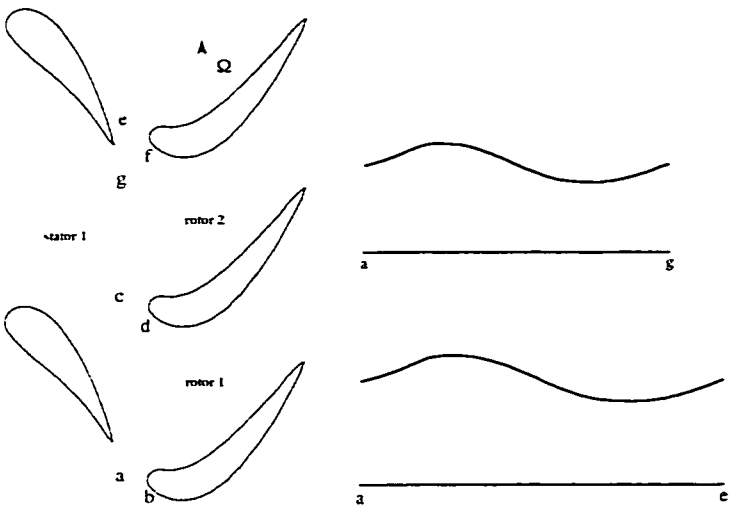

Figure 1.5 Gradient scaling method applied to a single stage configuration with unequal pitches; (a) actual geometry, (b) scaled flow solution on both halves of the interface

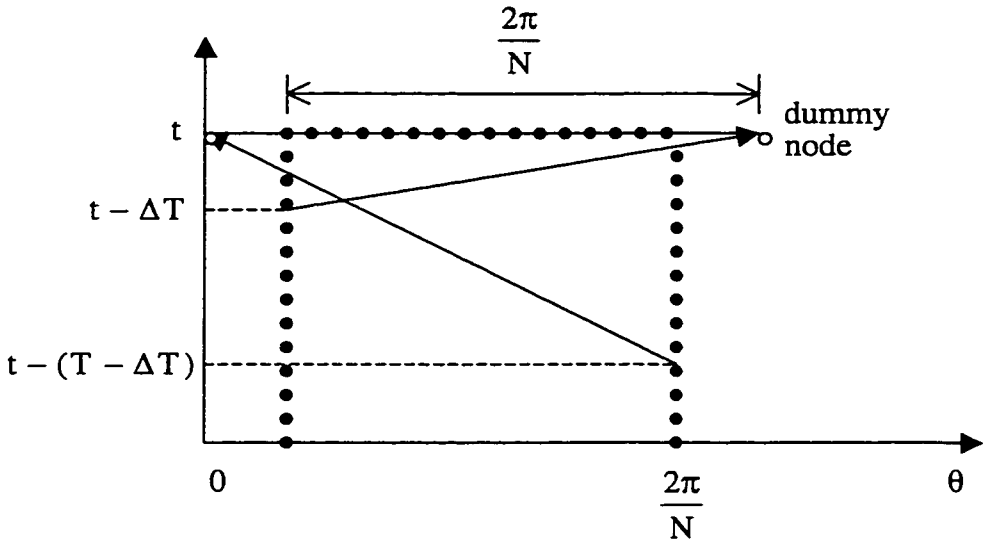

Figure 1.6 Periodic boundary condition by Erdos' method

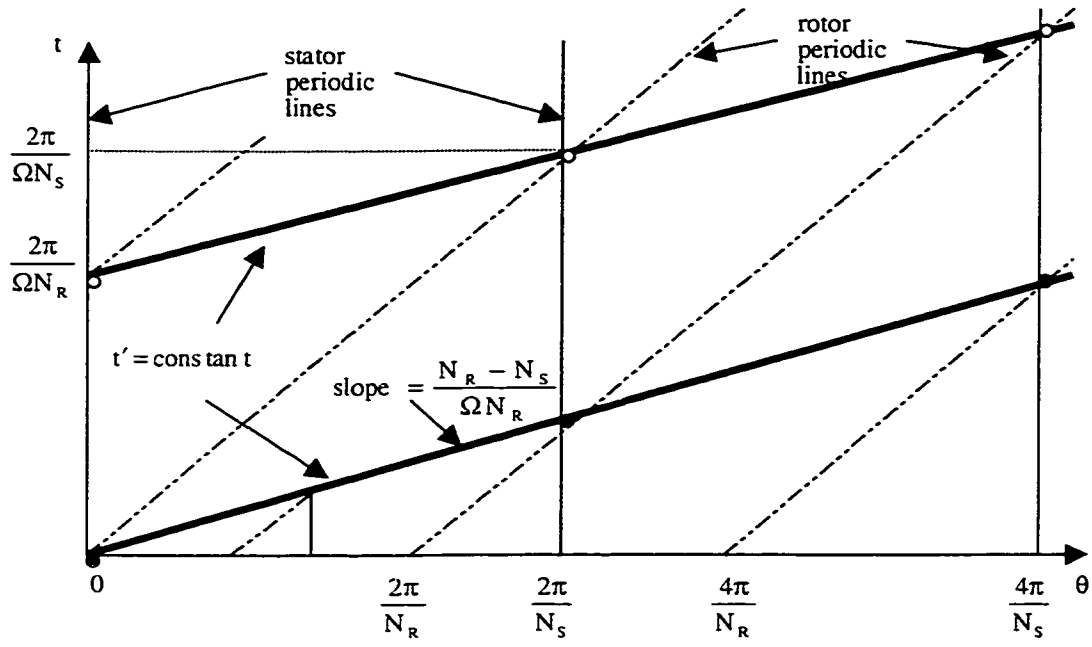

Figure 1.7 Time-inclined computational method; concept is demonstrated via a turbine stage configuration with unequal pitches viewed in the stator frame

2. Governing Flow Equations and Finite Element Discretization

2.1 Introduction

Chapter 2 describes the governing equations for viscous flows and their finite element discretization. The flow solver used in the current work is *NS3D*, which is a 3-D laminar/turbulent, steady/unsteady, compressible Navier-Stokes/Euler code, developed jointly by Concordia University (CFD Laboratory) and Pratt & Whitney Canada [47]. In this thesis, viscous compressible flow of Newtonian fluids will be considered in the context of 3-D blade row interaction in axial and centrifugal turbomachinery stages. *NS3D* solves for the mass flux components variables ρu_r, ρu_θ, ρu_z, pressure p and total enthalpy H_o.

2.2 Navier-Stokes Equations

The fluid dynamics equations arise from the application of the conservation of mass, momentum and energy laws to a fluid flow. These governing equations are often written in non-dimensional form so that the non-dimensional flow variables are usually of the order of magnitude of unity - a convenient means in computational work to minimize numerical roundoff errors resulting from the different flow variable scales. In *NS3D* the following non-dimensionalization has been carried out,

$$x^* = \frac{x}{L} \quad u^* = \frac{u}{V_\infty} \quad \rho^* = \frac{\rho}{\rho_\infty} \quad p^* = \frac{p}{\rho_\infty V_\infty^2} \quad T^* = \frac{T}{T_\infty} \quad C_p^* = \frac{C_p}{C_{p_\infty}} \tag{2.1}$$

where the non-dimensional variables are denoted by an asterisk, free stream conditions are represented by ∞ and L is the reference length used in the Reynolds number.

The full system of Reynolds-Averaged Navier-Stokes equations provides the most commonly used description of viscous fluid flow. This system of equations includes:

Continuity Equation

$$\frac{\partial \rho}{\partial t} + \nabla \bullet \left(\rho \bar{V}\right) = 0 \tag{2.2}$$

Momentum Equations

The body forces are neglected in the following vector form of the viscous momentum equations:

$$\begin{aligned} \rho \frac{D\bar{V}}{Dt} = -\nabla p + \frac{1}{Re}\left[\frac{4}{3}\nabla\left(\mu \nabla \bullet \bar{V}\right) + \nabla\left(\bar{V} \bullet \mu \nabla\right) - \bar{V}\nabla^2\mu\right] \\ + \frac{1}{Re}\left[\nabla\mu \times \left(\nabla \times \bar{V}\right) - \left(\nabla \bullet \bar{V}\right)\nabla\mu - \nabla \times \left(\nabla \times \mu\bar{V}\right)\right] \end{aligned} \tag{2.3}$$

Energy Equation

The energy equation, under the assumption of a variable property perfect gas and in the absence of heat sources and radiation heat transfer, can be written as

$$\rho \frac{DH_0}{Dt} - Ec\frac{\partial p}{\partial t} - \nabla \bullet \left(\frac{\kappa}{PrRe}\nabla T\right) - \nabla \bullet \left(\frac{Ec}{Re}\bar{V}\sigma_{ij}\right) = 0 \tag{2.4}$$

where σ_{ij} denotes the viscous stress tensor.

It has become common practice to include the continuity equation (2.2) and the energy equation (2.4) in the set of equations called the Navier-Stokes equations although, strictly speaking, this term refers only to the components of the viscous momentum equation (2.3). To close the system of equations, additional relations are required, namely, the equation of state

$$p = \rho RT \tag{2.5}$$

and empirical equations expressing viscosity μ and thermal conductivity k as functions of temperature [48].

2.3 Galerkin Finite Element Method

2.3.1 Overview of the Finite Element Approximation

In the finite element method, a geometrically complex domain of a given flow problem is discretized as a collection of simple nonoverlapping subdomains called elements [49-51]. Within each element a certain number of points or nodes are defined, which can be located on the edges, faces or inside the element. The numerical value of the solution unknowns is to be determined at these nodes. These solution variables are approximated by polynomials. If ϕ_h is an approximate solution of $\phi(\bar{x})$, a series expansion of the form

$$\phi_h(\bar{x}) = \sum_J \hat{\phi}_J N_J(\bar{x}) \tag{2.6}$$

may be written where the summation extends over all nodes J and N_J are the shape or interpolation functions. The functions N_J are chosen to be locally

defined polynomial interpolations within each element, taking on a zero value outside the particular element. The coefficients $\hat{\phi}_J$ in equation (2.6) are the unknown nodal values of the solution variable. These local interpolation functions possess the following properties on each element e, where node J belongs to e:

(i) at $\phi_h(x_J, y_J, z_J) = \hat{\phi}_J$, the function $N_J^{(e)}$ satisfies

$$N_I(x_J, y_J, z_J) = \begin{cases} 0 & \text{if} \quad I \neq J \\ 1 & \text{if} \quad I = J \end{cases} \tag{2.7}$$

(ii) at any point (x, y, z) within an element,

$$\sum_J N_J^{(e)}(x, y, z) = 1.0 \tag{2.8}$$

The global function N_J is obtained by assembling the contributions $N_J^{(e)}$ of all the elements to which node J belongs.

The method of weighted residuals offers a means by which to formulate the finite element equations. In this work the discretized form of the governing equations is obtained by minimizing, in a weighted average sense, the residuals of the system of equations (Navier-Stokes equations (2.2)-(2.4)) over the solution domain. This is carried out by multiplying each equation by a weight function, which in the Galerkin finite element method is identical to the shape function, and integrating over the domain. The weak form is then obtained by integrating by parts the weighted residual form of the system of equations. Details of the

weak Galerkin formulation for the full Navier-Stokes system of equations are provided in Appendices A and B.

2.3.2 Finite Element Discretization

NS3D accommodates isoparametric linear tetrahedral, trilinear hexahedral, and linear prismatic elements. Isoparametric elements use the same shape functions to define both geometry and solution variables. To simplify analytical expressions for elements of complex shapes, a reference element is defined in a local non-dimensional space with a simple geometrical shape, as shown for the trilinear hexahedral element in fig. 2.1. The transformation from $\bar{\xi}^e$-space to $\bar{x}^e$-space makes use of the shape functions in local coordinates through the geometrical discretization:

$$x = \sum_{J}^{ndperl} N_J(\xi,\eta,\zeta)\hat{x}_J \quad y = \sum_{J}^{ndperl} N_J(\xi,\eta,\zeta)\hat{y}_J \quad z = \sum_{J}^{ndperl} N_J(\xi,\eta,\zeta)\hat{z}_J \tag{2.9}$$

where the variable, ndperl, refers to the number of nodes per element. Similarly, the solution vector $\mathbf{U} = (\rho u_r, \rho u_\theta, \rho u_z, p)$ is approximated as

$$\mathbf{U} = \sum_{J}^{ndperl} N_J(\xi,\eta,\zeta)\hat{\mathbf{U}}_J \tag{2.10}$$

In *NS3D* all the solution variables are interpolated with shape functions of equal order and trilinear hexahedral shape functions are used,

$$
\begin{aligned}
N_1 &= \frac{1}{8}(1-\xi)(1-\eta)(1-\zeta) \qquad N_5 = \frac{1}{8}(1-\xi)(1-\eta)(1+\zeta) \\
N_2 &= \frac{1}{8}(1+\xi)(1-\eta)(1-\zeta) \qquad N_6 = \frac{1}{8}(1+\xi)(1-\eta)(1+\zeta) \\
N_3 &= \frac{1}{8}(1+\xi)(1+\eta)(1-\zeta) \qquad N_7 = \frac{1}{8}(1+\xi)(1+\eta)(1+\zeta) \\
N_4 &= \frac{1}{8}(1-\xi)(1+\eta)(1-\zeta) \qquad N_8 = \frac{1}{8}(1-\xi)(1+\eta)(1+\zeta)
\end{aligned}
\tag{2.11}
$$

Such a transformation to local coordinates facilitates the numerical integration of the stiffness matrix and residual vector equations.

In the Galerkin weighted residual method, the weight functions are chosen to be identical to their corresponding shape functions, that is,

$$W_I(\xi,\eta,\zeta) = N_I(\xi,\eta,\zeta) \tag{2.12}$$

2.4 Artificial Dissipation

2.4.1 Continuity Equation

In *NS3D* the discretized form of the continuity equation is obtained by applying the Galerkin finite element method which is equivalent to approximating the derivative terms by a central finite difference scheme. In such a centered scheme, the first order derivatives are decoupled leading to an odd-even point decoupling or checkerboarding effect. The Ladyzenskhaya-Babuska-Brezzi (LBB) stability condition established that checkerboarding would occur unless the interpolation functions for velocities are one order higher than those for pressure [51]. Since *NS3D* employs equal order interpolation for both velocities and pressure variables, artificial dissipation terms are added to the governing equations to suppress this decoupling. These additional terms help eliminate

unphysical numerical oscillations which should be minimized so as not to degrade the approximate solution.

A pressure dissipation term, $\lambda\nabla^2 p$, is added to the right-hand side of the continuity equation, yielding

$$\frac{\partial \rho}{\partial t} + \nabla \bullet \left(\rho \bar{V}\right) = \lambda \nabla^2 p \tag{2.13}$$

This dissipation term produces an error in mass conservation proportional to its magnitude. To refine it to second order accuracy, the dissipation term is reformulated as follows,

$$\frac{\partial \rho}{\partial t} + \nabla \bullet \left(\rho \bar{V}\right) = \lambda \nabla \bullet \left(\nabla p - \overline{\nabla p}\right) \tag{2.14}$$

where the balancing term, $\overline{\nabla p}$, represents the nodal values of the averaged gradients of pressure [47,52]. The user-specified coefficient λ must be sufficiently small to minimize the error in mass conservation but also large enough to prevent spurious pressure oscillations.

2.4.2 Momentum Equations

Most fluid flows in turbomachinery blade rows have high Reynolds numbers where the convective terms of the Navier-Stokes equation are dominant. If left unmodified, the convective terms may lead to numerical instabilities. Thus, all Navier-Stokes schemes must incorporate some form of numerical dissipation to stabilize the numerical scheme. This may involve the addition of explicit upwind

biased dissipation terms to the momentum equations or the use of an upwind biased discretization for the convective terms.

2.4.2.1 Streamline Upwind Petrov-Galerkin Formulation (SUPG)

NS3D uses the Streamline Upwind Petrov-Galerkin (SUPG) numerical dissipation scheme [53-55] whereby the finite element weight functions are modified to give them an upwind bias. The weight functions are applied to all terms in the momentum equations. This is an important difference since most numerical dissipation methods are developed by focusing only on the convective terms.

In the standard finite element formulation the governing equations are multiplied by a weight function W_I and integrated over the domain. The SUPG formulation adds to this weight function a perturbation weight function, W_I^{SUPG}, that gives the system good stability properties, while maintaining second order accuracy [53]. This perturbation weight function is calculated as follows:

$$W_I^{SUPG} = \tau_{SUPG}\left(u_r \frac{\partial W_i}{\partial r} + u_\theta \frac{\partial W_i}{r\partial\theta} + u_z \frac{\partial W_i}{\partial z} \right), \tag{2.15}$$

where (u_r, u_θ, u_z) represent the velocity components and (r,θ,z) denote the Cylindrical coordinates. The variable, τ_{SUPG}, is similar to a time term and is defined as

$$\tau_{SUPG} = c_1 * \text{fact1} * \frac{h^e}{|V|} \tag{2.16}$$

where

h^e is the length of the streamline cutting through a given element,

$|V|$ is the velocity magnitude,

c_1 is a numerical constant (In [53], a value of 0.5 is recommended but the current work has shown that it may be lowered to 0.25 with no adverse effects), and

fact1 is a factor based on the grid Peclet number given by

$$\text{fact1} = \text{MIN}(\text{Pec}/3, 1.0) \tag{2.17}$$

which, in the case of grid Peclet numbers less than three, results in a decrease in the value of τ_{SUPG}.

The perturbation weight function W_I^{SUPG} contains derivatives and thus cannot be integrated by parts since it would vanish for trilinear elements. However, *NS3D* uses the conservative form of the momentum equations which must be integrated by parts. To circumvent this problem, a non-conservative form of the momentum equations, excluding the viscous terms, is used which does not need to be integrated by parts. The implementation of SUPG in *NS3D* requires that a mixture of conservative and nonconservative forms be used. Specifically, the standard Galerkin weight function is applied to the conservative form of the equations and the perturbation SUPG weight function is applied to the non-conservative form. It should be noted that, for both conservative and non-conservative equations, the SUPG term vanishes for the viscous terms. The resulting formulation can be illustrated by examining the inviscid z-momentum equation:

$$\int_V \left(W_I \frac{\partial(\rho u_z)}{\partial t} - \frac{\partial W_I}{\partial z}\left(p + \rho u_z^2\right) - \frac{\partial W_I}{r\partial\theta}(\rho u_z u_\theta) - \frac{\partial W_I}{\partial r}(\rho u_z u_r) \right.$$
$$\left. + W_I^{SUPG}\left(\frac{\partial(\rho u_z)}{\partial t} + \rho u_z \frac{\partial u_z}{\partial z} + \rho u_\theta \frac{\partial u_\theta}{r\partial\theta} + \rho u_z \frac{\partial u_z}{\partial z} + \frac{\partial p}{\partial z} \right) \right) dV = 0 \tag{2.18}$$

2.4.2.2 Shock Function

While SUPG works very well when the flow varies smoothly, it is known to have stability problems in the presence of sharp discontinuities such as shocks [56]. For this reason, another weight function, W_I^{SHK}, is defined to capture shocks. It is identical to W_I^{SUPG} with the exception that τ_{SUPG} is replaced with τ_{SHK} given below,

$$\tau_{SHK} = fact2 * \frac{h^e}{|V|} \tag{2.19}$$

The variable fact2 is calculated from a shock detection algorithm, which is activated only in the presence of shocks. This additional weight function is applied only to the non-conservative form of the convection terms. Using the z-momentum equation as an illustration, this yields a term taking the form below:

$$W_I^{SHK}\left(\frac{\partial(\rho u_z)}{\partial t} + \rho u_r \frac{\partial u_r}{\partial r} + \rho u_\theta \frac{\partial u}{r\partial\theta} + \rho u_z \frac{\partial u_z}{\partial z} \right) \tag{2.20}$$

2.5 Time Discretization

A finite difference time integration scheme based on Gear's method has been implemented in *NS3D* for the time-accurate solution of the unsteady compressible Navier-Stokes and Euler equations [57]. Gear's method is a class of implicit time integration schemes which are characterized by large stability limits. The method is of backward differentiation type and possesses a variable

order of accuracy in time which can be controlled by the number of time levels used.

In general, after space discretization one arrives at a set of ordinary differential equations in time,

$$\mathbf{M}\dot{\mathbf{U}} + \mathbf{K}\mathbf{U} = \mathbf{F} \qquad 0 \le t \le T \tag{2.21}$$

where $\mathbf{U}$ represents the global vector of nodal values of the solution variable $\mathbf{U}(r,\theta,z,t)$, $\mathbf{M}$ is the mass matrix, $\mathbf{K}$ is the influence matrix, $\mathbf{F}$ is the source vector and T denotes the time span over which $\mathbf{U}$ is computed. Applying the *k*th order Gear scheme to the time term in equation (2.21) yields:

$$\left(\frac{\partial \mathbf{U}}{\partial t}\right)^t = \frac{1}{\Delta t}\left(\alpha_0 \mathbf{U}^t + \sum_{i=1}^{k} \alpha_i \mathbf{U}^{t-i\Delta t}\right) \tag{2.22}$$

where α_i (for i=0,1,...,k) and k are the coefficients and required order of time accuracy of the Gear scheme, respectively. In *NS3D*'s time-marching approach to a steady-state solution, the first order Gear scheme (k=1, α_0=1 and α_1=-1), which is identical to the implicit Euler backward scheme, is applied to the time-dependent terms of the system of equations, giving

$$\mathbf{U}_t = \mathbf{U}_{t-1} + \Delta t \mathbf{M}^{-1}[\mathbf{F} - \mathbf{K}\mathbf{U}] \tag{2.23}$$

The Euler backward scheme is commonly used as a matrix preconditioner to augment the diagonal dominance and hence the stability of time-marching approaches to steady-state problems. The second order Gear scheme (k=2) is

used to accurately resolve unsteady flow phenomena. Details of the temporal discretization of the full Navier-Stokes system of equations are given in Appendices A, B and C.

2.6 Newton Linearization

For reasons of stability and robustness of the numerical scheme, the continuity and momentum equations (2.2-2.3) are solved simultaneously (for details, see Chapter 4). To keep the coefficient matrix to a manageable size, the energy equation (2.4) is solved in a segregated manner. The nonlinear governing equations are linearized by a Newton method whereby each variable of the solution vector, $\mathbf{U} = (\rho u_r, \rho u_\theta, \rho u_z, p)$, is expressed in delta form, $\Delta\mathbf{U} = \mathbf{U}^{n+1} - \mathbf{U}^n$. After neglecting second order terms and substituting equations (2.10) and (2.12) into the Newton linearized system of equations, the delta form of the continuity, momentum and energy equations is assembled, over the elements of the domain, in terms of the nodal unknowns, $\Delta(\rho u_r)$, $\Delta(\rho u_\theta)$, $\Delta(\rho u_z)$, Δp and ΔH_0. The discretized equations may be written compactly as equations (2.24-2.28) below:

$$\sum_{e=1}^{nelem}\left[\sum_{j=1}^{ndperl}\left\{\left[k^{\rho u_r}{}_{ij}\right]_p \Delta(\rho u_r)_j + \left[k^{\rho u_\theta}{}_{ij}\right]_p \Delta(\rho u_\theta)_j + \left[k^{\rho u_z}{}_{ij}\right]_p \Delta(\rho u_z)_j + \left[k^{p}{}_{ij}\right]_p \Delta(p)_j\right\}\right] = -\mathrm{Res}^n_p$$

$$\sum_{e=1}^{nelem}\left[\sum_{j=1}^{ndperl}\left\{\left[k^{\rho u_r}{}_{ij}\right]_{\rho u_r} \Delta(\rho u_r)_j + \left[k^{\rho u_\theta}{}_{ij}\right]_{\rho u_r} \Delta(\rho u_\theta)_j + \left[k^{\rho u_z}{}_{ij}\right]_{\rho u_r} \Delta(\rho u_z)_j + \left[k^{p}{}_{ij}\right]_{\rho u_r} \Delta(p)_j\right\}\right] = -\mathrm{Res}^n_{\rho u_r}$$

$$\sum_{e=1}^{nelem}\left[\sum_{j=1}^{ndperl}\left\{\left[k^{\rho u_r}{}_{ij}\right]_{\rho u_\theta} \Delta(\rho u_r)_j + \left[k^{\rho u_\theta}{}_{ij}\right]_{\rho u_\theta} \Delta(\rho u_\theta)_j + \left[k^{\rho u_z}{}_{ij}\right]_{\rho u_\theta} \Delta(\rho u_z)_j + \left[k^{p}{}_{ij}\right]_{\rho u_\theta} \Delta(p)_j\right\}\right] = -\mathrm{Res}^n_{\rho u_\theta}$$

$$\sum_{e=1}^{nelem}\left[\sum_{j=1}^{ndperl}\left\{\left[k^{\rho u_r}{}_{ij}\right]_{\rho u_z} \Delta(\rho u_r)_j + \left[k^{\rho u_\theta}{}_{ij}\right]_{\rho u_z} \Delta(\rho u_\theta)_j + \left[k^{\rho u_z}{}_{ij}\right]_{\rho u_z} \Delta(\rho u_z)_j + \left[k^{p}{}_{ij}\right]_{\rho u_z} \Delta(p)_j\right\}\right] = -\mathrm{Res}^n_{\rho u_z}$$

$$\sum_{e=1}^{nelem}\left[\sum_{j=1}^{ndperl}\left[k^{H_0}{}_{ij}\right]_{H_0} \Delta(H_0)_j\right] = -\mathrm{Res}^n_{H_0}$$

where nelem denotes the total number of elements, Res^n represents the residual of the given governing equation at Newton step n, and (i, j) are the row and column indices. Details of equations (2.24)-(2.28) may be found in Appendices A, B and C.

2.7 Boundary Conditions for the Navier-Stokes Equations

Inlet Boundary Condition: $(\rho u_r, \rho u_\theta, \rho u_z)$ are specified.

The surface integrals of the continuity equation (A.6) are computed using the specified inlet mass flux, $\rho\bar{V}$. However, the contribution of the pressure dissipation term to the continuity contour integral is neglected due to the small value of λ. The momentum equations are not evaluated at the inlet and are replaced by the imposition of the specified inlet mass flux, $\rho\bar{V}$.

Wall Boundary Condition: $u_r = u_\theta = u_z = 0$ is imposed as the no-slip condition.

The surface integral of the continuity equation is not evaluated since $\bar{V} = 0$ and the contribution of the pressure dissipation term to this integral is neglected due to the small value of λ. The momentum equations are replaced at the wall nodes by the imposition of $\bar{V} = 0$.

Exit Boundary Condition: p is specified.

The static pressure is specified at all exit points and replaces the continuity equation. The normal derivatives of $\bar{V}$ are neglected in the momentum contour integrals. All artificial dissipation terms in the momentum surface integrals are also neglected due to the small value of the artificial dissipation coefficients.

Symmetry Boundary Condition:

For the continuity equation zero normal mass flux is imposed by neglecting the surface integrals. In the computation of the momentum surface integrals the convective terms are assumed small and neglected. The shear stress is also set to zero as one of the boundary conditions. All artificial dissipation terms in the momentum surface integrals are neglected due to the small value of the artificial dissipation coefficients.

Periodic Boundary Condition:

For a passage of a blade row and under the assumption of steady flow or unsteady flow with equal rotor and stator pitches, the grid points on the upper free surface are identical to those on the lower one. This is done by warping the grid around at the free surfaces, and solving for the first node of the periodic pair while imposing Dirichlet boundary conditions on the second pair. The solution of the second pair inherits that of the first periodic pair, which is obtained from the flow solver.

Interface Boundary Condition:

This boundary condition is required for multistage test cases. For steady multistage the interface has a "mixed-out" boundary condition: exit and inlet. The upstream interface plane is treated as an exit, whereas the downstream interface plane is treated as an inlet. Boundary conditions are exchanged at these planes as they are updated, iteratively, via the flow solver. For unsteady multistage with equal rotor and stator pitches, the rotor and stator grids are just touching one another at the interface plane. One side of the interface, which is termed the dead side, is set to Dirichlet type boundary conditions, while the other side, referred to as the live side, is to be solved for. Faces on both sides of

the interface are assembled into the governing equations and the contribution of the dead side is properly distributed into the live side. The solution of the nodes of the dead is interpolated from those of the live side. Details on the implementation of the interface and the interpolation procedure are described in Chapter 3.

FIGURES

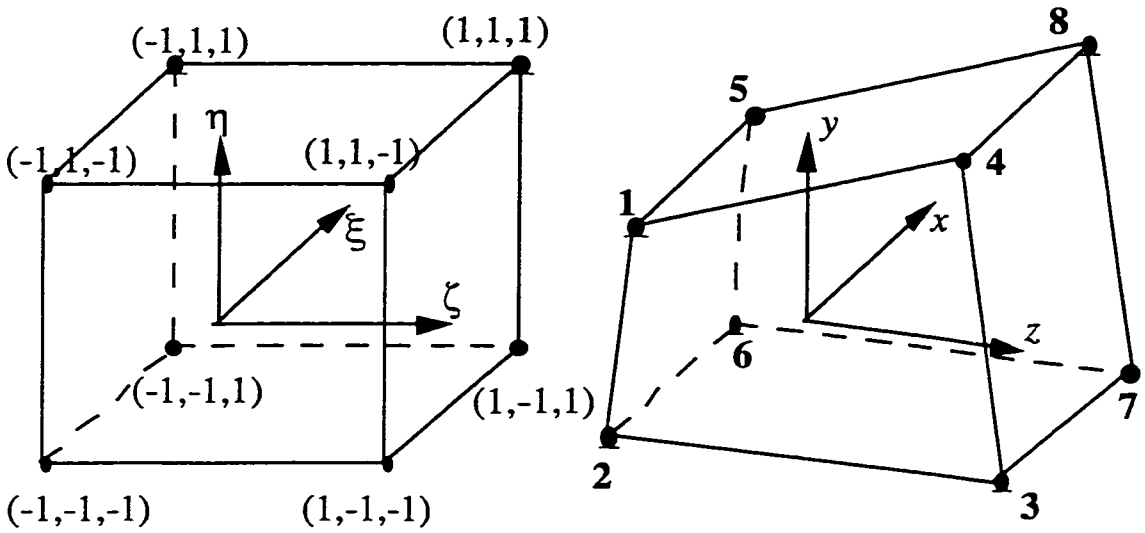

(a) Natural coordinates (b) Physical coordinates

Figure 2.1 Isoparametric trilinear element

3. Multistage Methods

3.1 Introduction

The flow in a turbomachine is very complex, being three-dimensional, viscous, turbulent and unsteady. Analyzing the flow field within the passage of a blade row without considering the effects of the upstream and the downstream blade rows is both misleading and inaccurate. Thus, it is not possible to optimize a design of a blade row without thoroughly studying the effects of neighboring ones. Benefits due to aerodynamic flow behavior are difficult, if not impossible, to achieve if multistage effects are to be ignored. Specifically, the effects of axial spacing, blade count, clocking, and levels of unsteadiness may be quite significant. Over the last decade, researchers and engineers have been investigating the flow physics within the passage of a blade row embedded in a multistage environment to gain a better understanding of flows through compressors and turbines. In doing so, gas turbine manufacturers rely heavily on experimental testing as well as numerical simulation. This chapter describes the computational multistage methods used in this Thesis. These methods are applicable to the analysis of the flow in axial and centrifugal stages of turbomachines.

3.2 Steady Rotor-Stator Interaction Models

Numerical simulation of the flow phenomena in axial turbines and compressors is demanding in terms of computing resources. It is for this reason that much research has been devoted to the development of fast and efficient numerical models. One popular method, which is applied in this thesis and has been used extensively by gas turbine companies, is the mixing plane method.

3.2.1 Mixing Plane Method

The mixing plane method is a powerful analytical tool for the analysis of fluid flow in axial turbomachinery stages under the assumption of steady flow. The novel features of the mixing plane method are two-fold: it is able to represent the multistage environment while solving for an individual blade row and, the inter-blade row boundary conditions are calculated rather than being imposed [5].

The boundary conditions at inlet and outlet of each blade row are assumed to be steady and uniform in the circumferential direction. These boundary conditions are not known *a priori* and, hence, they constitute part of the numerical solution. The mixing plane is defined as the common interface plane between adjacent blade rows (figure 3.1). The rotor-stator interaction begins with an initialization of the flow fields in the adjacent blade rows and, at each iteration, the interface boundary conditions are updated by passing the proper information between the upstream and the downstream blade rows. It is at the mixing plane that the solutions of adjacent blade rows are coupled and the quantities necessary for conservation laws are averaged. Once the averaging procedure has been performed, these quantities are then passed axisymmetrically to the adjacent blade row. As an example, one mixing plane would be required in the analysis of a single stage axial flow compressor, that is, a rotor followed by a stator, and this interface would be located somewhere between the trailing edge of the rotor and the leading edge of the stator, normal to the engine axis.

The mesh requirements for the mixing plane method can be stated as follows:

- Single passage mesh for each blade row with tip clearance
- Non-overlaping grids between blade rows

- Mixing plane shared between adjacent blade rows normal to engine axis
- Identical spanwise grid point distribution at the mixing plane.

A non-matching spanwise grid point distribution at the mixing plane is possible, while this has been found to slow the rate of convergence and introduce interpolation errors of averaged flow quantities at the mixing plane. Therefore, such a grid point distribution was abandoned.

The solution procedure for the mixing plane method consists of the following steps:

- Solve each blade row with fixed inlet and exit boundary conditions
- Iteratively update boundary conditions at the mixing plane via proper averaging methods
- Match radial profiles or averaged flow properties at the mixing plane

The derivation of thermodynamic variables is based on the "mixed-out" approach which assumes that the flow is instantaneously mixed at the interface plane [6]. The mathematical derivation is presented below.

Consider the following fluxes

$$F_1 = \overline{\rho u}_z = \frac{1}{\text{Pitch}} \int_0^{\text{Pitch}} \rho u_z d\theta \tag{3.1}$$

$$F_2 = \overline{\rho u}_z^2 + \overline{p} = \frac{1}{\text{Pitch}} \int_0^{\text{Pitch}} \left(\rho u_z^2 + p\right) d\theta \tag{3.2}$$

$$F_3 = \overline{\rho u}_z \overline{u}_\theta = \frac{1}{\text{Pitch}} \int_0^{\text{Pitch}} \rho u_z u_\theta d\theta \tag{3.3}$$

$$F_4 = \overline{\rho u}_z \overline{u}_r = \frac{1}{\text{Pitch}} \int_0^{\text{Pitch}} \rho u_z u_r d\theta \tag{3.4}$$

$$F_5 = \overline{\rho u}_z \overline{H}_o = \frac{1}{\text{Pitch}} \int_0^{\text{Pitch}} \rho u_z H_o d\theta \tag{3.5}$$

and the following total enthalpy equation:

$$\overline{H}_o = \frac{\gamma}{\gamma - 1} \frac{\overline{p}}{\overline{\rho}} + \frac{1}{2} \left(\overline{u}_r^2 + \overline{u}_\theta^2 + \overline{u}_z^2 \right) \tag{3.6}$$

Since the mixing plane is assumed to be normal to the engine axis, equations (3.1-3.5) can be obtained from the continuity, momentum, and energy. The viscous terms in the momentum and energy fluxes have been neglected since they involve the derivatives of the three components of velocity.

Equations (3.1-3.6) can be solved to obtain the "mixed-out" values of pressure, velocity, and total enthalpy as follows:

$$\overline{p} = \frac{\gamma}{\gamma + 1} \left(F_2^2 + \sqrt{F_2^2 + \left(\gamma^2 - 1\right)\left(F_2^2 + F_3^2 + F_4^2 - 2F_1F_5\right)} \right) \tag{3.7}$$

$$\overline{u}_z = \frac{F_2 - \overline{p}}{F_1} \tag{3.8}$$

$$\overline{u}_\theta = \frac{F_3}{F_1} \tag{3.9}$$

$$\overline{u}_r = \frac{F_4}{F_1} \tag{3.10}$$

$$\overline{H}_o = \frac{F_5}{F_1} \tag{3.11}$$

$$\overline{\rho} = \frac{F_1}{\overline{u}_z} \tag{3.12}$$

Values of all other flow variables, such as total pressure, static temperature, Mach number, and flow angles can be defined based on the "mixed-out"

quantities. It should be noted that the physical mixing process implied in this procedure will generate viscous losses and result in a flow with a higher entropy level and, thus, higher measured losses than the actual ones. All the circumferenfial profiles are assumed to be mixed out instantaneously at the interface. This instantaneous mixing at the interface plane changes the blockage which, in turn, causes the static pressure to increase across the plane, while the mixing loss brings about a drop in total pressure across the plane [6].

The objective of this method is to match the averaged flow quantities as boundary conditions at the mixing plane. The following quantities are converted into the appropriate frame of reference, that is, relative in the rotor and absolute in the stator;

$$\overline{\rho}_{\text{(rotor)}} = \overline{\rho}_{\text{(stator)}} \tag{3.13}$$

$$\overline{u}_{z\ \text{(rotor)}} = \overline{u}_{z\ \text{(stator)}} \tag{3.14}$$

$$\overline{u}_{\theta\ \text{(rotor)}} = \overline{u}_{\theta\ \text{(stator)}} - \Omega r \tag{3.15}$$

$$\overline{u}_{r\ \text{(rotor)}} = \overline{u}_{r\ \text{(stator)}} \tag{3.16}$$

$$\overline{p}_{\text{(rotor)}} = \overline{p}_{\text{(stator)}} \tag{3.17}$$

3.3 Unsteady Rotor-Stator Interaction

This section describes a finite element based method for the computation of the unsteady flow in a turbomachinery stage with equal and unequal pitches. The method for the case in which the blade rows have equal pitches is presented first, since it incorporates most of the essential elements for the algorithm for unequal pitches. The algorithm for the general case of unequal pitches, which uses the time-inclined computational planes mentioned in Chapter 1, will then be

described. From a purely mathematical viewpoint, the latter procedure is a straightforward extension of the equal pitch method.

3.3.1 Rotor-Stator Interaction with Equal Pitches

In the current work, the frame of reference is chosen to be the absolute stator frame. However, when the flow variables are to be updated, they must be converted back into their local frame of reference.

The computational grid is composed of two parts, one part fixed to the stator blade row and the other part fixed to, and moving with, the rotor blade row. As shown in figure 3.2, the grids are not conforming at the rotor-stator interface.

It has been found that the grid at the interface should be generated such that both the rotor and stator grids have approximately the same density, that is, the same element size. Figure 3.3 shows a typical mismatched grid at the interface plane. The grid with solid lines is termed "live" while the grid marked with the dashed lines is referred to as "dead". Nodes of a live grid (nodes 1 to 9) have a direct representation in the matrix solver and so, the finite element solution at these nodes is updated through the iterative solver. However, nodes of the dead grid (nodes I to L) have an indirect representation in the matrix solver since their contributions are distributed, based upon their physical location with respect to the elements of the live grid, into the nodes of the live grid. For example, nodes I, J, K and L lie in the middle of the four-noded elements: 2-5-4-1, 3-6-5-2, 6-9-8-5,and 5-8-7-4, respectively. Assembly of the live elements is carried out using the standard finite element method. A different approach is taken in the assembly of the dead elements: for example, the contributions of dead node I are distributed into the nodes 1, 2, 5 and 4, according to the value of the finite element shape

functions at node I (see table 3.1). The same procedure applies to nodes J, K and L.

Table 3.1 Contributions of dead nodes into live nodes

Local nodes	1	2	3	4
Global Nodes	2	5	4	1
Weight	0.25	0.25	0.25	0.25

A Dirichlet boundary condition is imposed at Node I and, therefore, it has no equation number. However, it is still assembled in the matrix and the residual. The contributions of equation I are distributed into equations 1, 2, 3, and 4. The finite element solution of node I can then be written as

$$\mathbf{U}_I = \sum_{J=1}^{4} N_J(\xi,\eta,\zeta)\hat{\mathbf{U}}_J \tag{3.18}$$

The solution at node I is then updated from the solution at nodes 1, 2, 3, and 4 using the above equation. In doing so, the residual and the solution at node I are computed in a consistent manner.

When the stator-to-rotor pitch ratio is unity, the periodic boundary condition may be implemented in a straightforward manner. The lower periodic line sees the same flow field as the upper periodic line at the same time. In situations where the stator pitch is different from the rotor pitch, this no longer holds true. If one considers the case in which the stator pitch is larger than the rotor pitch, then an incoming stator wake would cross the rotor upper periodic boundary at a small time ΔT after the neighboring wake crosses the lower periodic boundary. This is discussed in the next section.

3.3.2 Rotor-Stator Interaction with Unequal Pitches

Computationally, it is very easy to enforce the spatial periodicity for steady flows or unsteady flow with equal pitches, as mentioned earlier. However, in unsteady calculations in turbomachinery stages where there are different numbers of stator and rotor blades, a problem arises which is not present in steady-state calculations. The number of pitchwise periodic boundaries in a stator-rotor configuration is equal to the largest common divisor of the number of rotor blades to that of stator ones. In the worst case, the common divisor is unity. This means that all blade passages of the stator and rotor would have to be considered in the computation since integration of the system of governing flow equations cannot be carried out without a full set of boundary conditions. Even with today's supercomputers, it is difficult to get a reasonable unsteady Navier-Stokes simulation that includes all blade passages of a single turbomachinery stage. Therefore, one seeks a method that allows simple periodicity conditions to be applied on small computational domains, independently of the pitch ratio and without modifying or scaling the actual geometry of the problem.

To address this problem, Giles [6] developed the idea of a time-inclined computational domain. If a node at $\theta = 0$ is at time t, then the corresponding periodic node at $\theta = \theta_S$ is at time $t + \Delta T$. Mathematically, this corresponds to the use of a reversible transformation to transform the whole flow problem from (r, θ, z, t), the physical space, into (r', θ', z', t'), a computational space in which pitchwise boundaries are periodic boundaries even if they are not periodic in the physical space. This method [6] has been extended in this Thesis to three-dimensional viscous flows on non-conforming meshes at the interface plane common to adjacent rows.

The transformation is defined as follows:

$$\begin{aligned} r' &= r \\ \theta' &= \theta \\ z' &= z \\ t' &= t - \lambda\theta \end{aligned} \tag{3.19}$$

The inclination parameter λ represents the slope of the $t' =$ constant line and has a different value in the rotor and stator frames

$$\lambda = \begin{cases} \dfrac{\Delta T}{\theta_S} & \text{in the stator frame} \\ \dfrac{\Delta T}{\theta_R} & \text{in the rotor frame} \end{cases} \tag{3.20}$$

The time lag, ΔT, which is given by

$$\Delta T = T_R - T_S = \frac{\theta_S}{\Omega} - \frac{\theta_R}{\Omega} \tag{3.21}$$

represents the difference between T_R, the rotor blade-passing period and T_S, the stator blade-passing period. The stator and the rotor pitch angles are denoted as θ_S and θ_R, respectively. The time lag may be viewed as the amount of time in which the upper pitchwise boundary lags the lower pitchwise boundary to be periodic. In physical space, the periodicity condition is defined such that the time lag, ΔT, is equal to the difference in pitches divided by the rotor wheel speed.

When one transforms the unsteady governing equations, the resulting equations, in this new coordinate system, with $t' =$ constant, are

$$\frac{\partial Q}{\partial t'} + \frac{1}{r'}\frac{\partial}{\partial r'}(r'A) + \frac{1}{r'}\frac{\partial}{\partial \theta'}(B) + \frac{\partial}{\partial r'}(C) + \frac{D}{r'} = 0 \tag{3.22}$$

Thus, the conservation state variables have changed from U to $Q = U - \frac{\lambda}{r} B$, where

$$U = \begin{bmatrix} \rho \\ \rho u_r \\ \rho u_\theta \\ \rho u_z \end{bmatrix}, \quad B = \begin{bmatrix} \rho u_\theta \\ \rho u_r u_\theta - \sigma_{r\theta} \\ \rho u_\theta^2 + p - \sigma_{\theta\theta} \\ \rho u_z u_\theta - \sigma_{z\theta} \end{bmatrix} \tag{3.23}$$

The lagged periodic condition on the upper and lower periodic lines in the rotor and stator frames is given by

$$Q(r,\theta,z,t) = Q(r,\theta+\theta_{R,S},z,t+\Delta T) \tag{3.34}$$

Applying the transformation to the above equation yields the desired result

$$Q(r',\theta',z',t') = Q(r',\theta'+\theta_{R,S},z',t') \tag{3.35}$$

This method does not require any assumptions about the flow at the pitchwise boundaries or any geometry adjustments. Thus, it is able to reproduce all frequencies that are present in the flow field. A weak Galerkin formulation of the time-inclined Navier-Stokes equations is provided in Appendix D.

For inviscid flows, under the ideal gas assumption, the state variables U can be computed analytically from Q (examine equations (1.7) and (3.23)). For viscous flows, however, a differential algebraic system of equations results. The differentials in this case are simply ignored. The neglected viscous terms are

comparable in magnitude to those terms which are usually dropped in the thin-shear-layer Navier-Stokes equations under high Reynolds number conditions [6].

The calculation of U from Q leads to a quadratic equation for the static pressure. The investigation of its solutions, for a subsonic flow in the circumferential direction, yields the condition

$$-\frac{1}{c-u_\theta} \le \frac{\lambda}{r} \le \frac{1}{c+u_\theta}, \text{ or } 1-\frac{M_w}{1-M_\theta} \le \frac{\theta_S}{\theta_R} \le 1+\frac{M_w}{1+M_\theta} \tag{3.26}$$

This means that the inclination parameter λ is limited by the physical characteristics of the linearized Euler equations. This is a reasonable and fundamental limitation, as without this constraint, information, which is propagating forward in physical time, could be propagating backward in the computational time. This violates the principle of causality and is inconsistent with an integration algorithm that marches forward in time. Therefore, stator-rotor configurations with big differences in the pitches cannot be simulated using only one stator passage and one rotor passage. With the use of multiple blade passages, the inclination parameter can be reduced to a value that allows a stable simulation [6].

At the end of the computation, the solutions at different instants of the computational time are transformed back to obtain solutions at different instants of the physical time. This is done by storing the solutions at a number of time-steps (typically 50-100) during the last blade-passing period of the computation. After the simulation, the desired number of solutions at the desired instants of

the physical time are calculated from the stored solutions (see Section 3.6, Post-processing of Results for Unequal Pitches).

The calculation possesses the same number of time-steps per period on each half, so the time-steps on the two halves are related by

$$\theta_R \Delta t_R = \theta_S \Delta t_S \tag{3.27}$$

Figure 1.7 attempts to explain this by showing both the stator and rotor inclined computational grids in the stator frame of reference. This figure depicts a case in which the stator pitch is greater than the rotor pitch. The stator and rotor nodes coincide at the beginning of a computational period. Although at each time-level the stator and rotor grids lie on the same inclined computational plane, the rotor is displaced relative to the stator grid. The diagram shows that the stator pitch is greater than the rotor pitch at fixed time t, but that on the inclined computational plane the rotor pitch is identical to the stator pitch. The stator time step size is not equal to the rotor time step, even though both grids are consistently at the same computational time level [6].

3.4 Interpolation Procedure at the Rotor-Stator Interface

The goal of the interpolation procedure at the rotor-stator interface is to locate nodes of the target mesh (rotor or stator) in elements of the source mesh (stator or rotor) at the interface plane. The physical coordinates X, Y, and Z of any node T(X,Y,Z) of the target mesh can be represented by a finite element discretization in terms of the interpolation shape functions N_i. The coordinates of the nodes within an element, E, of the source mesh are expressed as follows:

$$X=\sum_{i=1}^{4}N_i x_i \quad Y=\sum_{i=1}^{4}N_i y_i \quad Z=\sum_{i=1}^{4}N_i z_i \tag{3.28}$$

where the 2-D quadrilateral finite element shape functions are given by

$$N_1=\frac{1}{4}(1-\xi)(1-\eta),\ N_2=\frac{1}{4}(1+\xi)(1-\eta) \tag{3.29}$$
$$N_3=\frac{1}{4}(1+\xi)(1+\eta),\ N_4=\frac{1}{4}(1-\xi)(1+\eta)$$

and ξ and η are the local coordinates of element E and x_i, y_i and z_i are its physical nodal coordinates.

The aim is to minimize the function D, which represents the distance between node T and element E,

$$D(x,y,z)=D(\xi,\eta)=H^2+G^2+P^2 \tag{3.30}$$

where

$$H=\sum_{i=1}^{4}N_i x_i-X,\ G=\sum_{i=1}^{4}N_i y_i-Y,\ P=\sum_{i=1}^{4}N_i z_i-Z \tag{3.31}$$

The minimization process requires that

$$\frac{dD}{d\xi}=2H\frac{\partial H}{\partial\xi}+2G\frac{\partial G}{\partial\xi}+2P\frac{\partial P}{\partial\xi}=0 \tag{3.32}$$
$$\frac{dD}{d\eta}=2H\frac{\partial H}{\partial\eta}+2G\frac{\partial G}{\partial\eta}+2P\frac{\partial P}{\partial\eta}=0 \tag{3.33}$$

X, Y, and Z can be easily found if ξ and η are given. However, this is not the case in the present problem and the task is to find the local coordinates (ξ,η) of node T given its physical coordinates (X,Y,Z). The equations representing X, Y, and Z are nonlinear and are solved via Newton method for the natural coordinates ξ and η.

The residuals of the equations are as follows:

$$R_1 = \frac{1}{2}\frac{dD}{d\xi} \text{ and } R_2 = \frac{1}{2}\frac{dD}{d\eta} \tag{3.34}$$

Expanding the residuals in a Taylor series and retaining the first order term, one obtains the following system of linear equations in $\Delta\xi$ and $\Delta\eta$

$$\begin{bmatrix} \left(\frac{\partial H}{\partial \xi}\frac{\partial H}{\partial \xi}+\frac{\partial G}{\partial \xi}\frac{\partial G}{\partial \xi}+\frac{\partial P}{\partial \xi}\frac{\partial P}{\partial \xi}\right) & \left(\frac{\partial H}{\partial \eta}\frac{\partial H}{\partial \xi}+\frac{\partial G}{\partial \eta}\frac{\partial G}{\partial \xi}+\frac{\partial P}{\partial \eta}\frac{\partial P}{\partial \xi}\right) \\ \left(\frac{\partial H}{\partial \eta}\frac{\partial H}{\partial \xi}+\frac{\partial G}{\partial \eta}\frac{\partial G}{\partial \xi}+\frac{\partial P}{\partial \eta}\frac{\partial P}{\partial \xi}\right) & \left(\frac{\partial H}{\partial \eta}\frac{\partial H}{\partial \eta}+\frac{\partial G}{\partial \eta}\frac{\partial G}{\partial \eta}+\frac{\partial P}{\partial \eta}\frac{\partial P}{\partial \eta}\right) \end{bmatrix} \begin{Bmatrix} \Delta\xi \\ \Delta\eta \end{Bmatrix} = \begin{Bmatrix} -R_1 \\ -R_2 \end{Bmatrix} \tag{3.35}$$

where, as an example,

$$\frac{\partial H}{\partial \xi} = \sum_{i=1}^{4}\frac{\partial N_i}{\partial \xi}x_i,\ \frac{\partial G}{\partial \xi} = \sum_{i=1}^{4}\frac{\partial N_i}{\partial \xi}y_i,\ \frac{\partial P}{\partial \xi} = \sum_{i=1}^{4}\frac{\partial N_i}{\partial \xi}z_i \tag{3.36}$$

It should be noted that X, Y, and Z are the coordinates of the node T of the target mesh, are constants, and hence are known quantities. As the above matrix is nonlinear, one solves for $\Delta\xi$ and $\Delta\eta$ to update the values of ξ and η as indicated

$$\xi^{n+1} = \xi^n + \Delta\xi,\ \eta^{n+1} = \eta^n + \Delta\eta \tag{3.37}$$

where ξ^n is the previous guess of ξ and ξ^{n+1} is its updated value. Once the correct values ξ and η are found, that is, their values lie between -1 and 1, and the distance D is below a user-defined tolerance, then the node is deemed to be inside the element E.

Details on the interpolation procedure at the rotor-stator interface are provided in Appendix E.

3.5 Grid Rotation

In the modeling of unsteady rotor-stator interaction, the rotor grid moves relative to the stator grid. This is a pure rotation which depends on the time step used, as well as the rotational speed of the rotor. At every time step, the rotor grid rotates as

$$\theta_r^{t+\Delta t} = \theta_r^t + \Omega\Delta t \tag{3.38}$$

Once the rotor grid has moved, the target mesh nodes should be found in the new location of source mesh elements at the interface plane.

3.6 Post-processing of Results for Unequal Pitches

The Fourier transform pairs used for the post-processing of the results in this Thesis are based upon the following equation, which expresses a mapping from the Fourier domain into the physical domain,

$$U(t)=\Re\left\{\sum_{k=0}^{K}\hat{U}_k e^{2\pi i\frac{kt}{T}}\right\}=\hat{U}_0+\frac{1}{2}\sum_{k=1}^{K}\left\{\hat{U}_k e^{2\pi i\frac{kt}{T}}+\hat{U}_k^* e^{-2\pi i\frac{kt}{T}}\right\} \tag{3.39}$$

where $\Re\{z\}$ denotes the real part of the complex variable z, and z* denotes the complex conjugate of z. The plotting procedure reconstructs the solution $U(t)$ at any instant in time based upon the Fourier coefficients $\hat{U}_k$. The aim is to calculate these coefficients from the data supplied by the rotor-stator finite element calculation, which consists of flow data on time-inclined computational planes at 40 ($NOS \geq 40$) equally spaced intervals during the last period of the calculation.

The correct time at a particular node on the computational plane is equal to

$$t = t' + \lambda\theta = \frac{n}{NOS}T + \lambda\theta \tag{3.40}$$

where T is the period, θ is the circumferential location of the node, and λ is the time-inclination parameter. Thus, one arrives at the following expression:

$$U_n = \hat{U}_0 + \frac{1}{2}\sum_{k=1}^{K}\left\{\hat{U}_k e^{2\pi i\left(\frac{kn}{NOS}+\frac{k\lambda\theta}{T}\right)}+\hat{U}_k^* e^{-2\pi i\left(\frac{kn}{NOS}+\frac{k\lambda\theta}{T}\right)}\right\} \tag{3.41}$$

The Fourier coefficients are determined as shown below:

$$\frac{1}{NOS}\sum_{n=1}^{NOS} e^{2\pi i(k-k')\frac{n}{NOS}} = \delta(k-k') = \begin{cases} 1, & k = k' \\ 0, & k \neq k' \end{cases} \tag{3.42}$$

$$\frac{1}{NOS}\sum_{n=1}^{NOS} U_n e^{-2\pi i \frac{kn}{NOS}} = \begin{cases} \hat{U}_0, & k=0 \\ \frac{1}{2}\hat{U}_k e^{2\pi i \frac{k\lambda\theta}{T}}, & k \geq 1 \end{cases} \tag{3.43}$$

Hence,

$$\hat{U}_0 = \frac{1}{NOS}\sum_{n=1}^{NOS} U_n \tag{3.44}$$

$$\hat{U}_k = \frac{2}{NOS} e^{-2\pi i \frac{k\lambda\theta}{T}} \sum_{k=1}^{NOS} U_n e^{-2\pi i \frac{kn}{NOS}}$$

The vector U, used in the above description, is not the usual state vector. Rather, it is the vector of primitive quantities. The main reason for this choice is that, in stator/rotor interaction cases, it ensures that the post-processing is independent of the choice of frame of reference, since the primitive variables are the same in both frames, except for a constant difference, Ωr, in u_θ.

For the maximum accuracy in reproducing the unsteady results, the recommended value for the variable K is 24. However, in practice, it is sufficient to choose K such that

$$\sum_{k=K+1}^{24} \left|\hat{U}_k\right|^2 \leq 10^{-8} \tag{3.45}$$

which guarantees that the resulting values of $U(t)$ will be correct to within 10^{-4}, which is perfectly acceptable for plotting. This compression of the Fourier data results in tremendous savings in terms of memory.

The flow at any instant in time is reconstructed through equation (3.39), which can be re-written as

$$U(t) = \bar{U}_0 + \sum_{k=1}^{K} \left\{ \Re(\bar{U}_k) \cos(k\phi) - I(\bar{U}_k) \sin(k\phi) \right\} \tag{3.46}$$

where I(z) is the imaginary part of z, and ϕ is defined by

$$\phi = 2\pi \frac{t}{T} \tag{3.47}$$

In calculating ϕ, care must be taken in stator/rotor cases to use the correct period on either side of the interface. A slight complication arises in plotting multiple blade passages from one set of Fourier data. This requires computing different values of ϕ for each blade passage, allowing for the time lag between passages. For the m^{th} passage, ϕ is given by

$$\phi_m = 2\pi \left(\frac{t + (m-1)\Delta T}{T} \right) \tag{3.48}$$

where ΔT is the time lag between periodic surfaces.

FIGURES

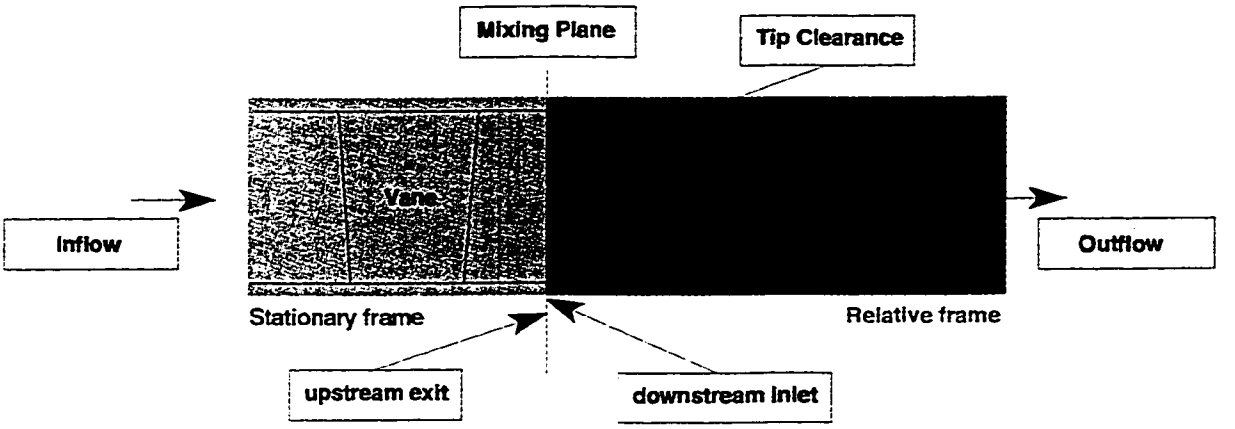

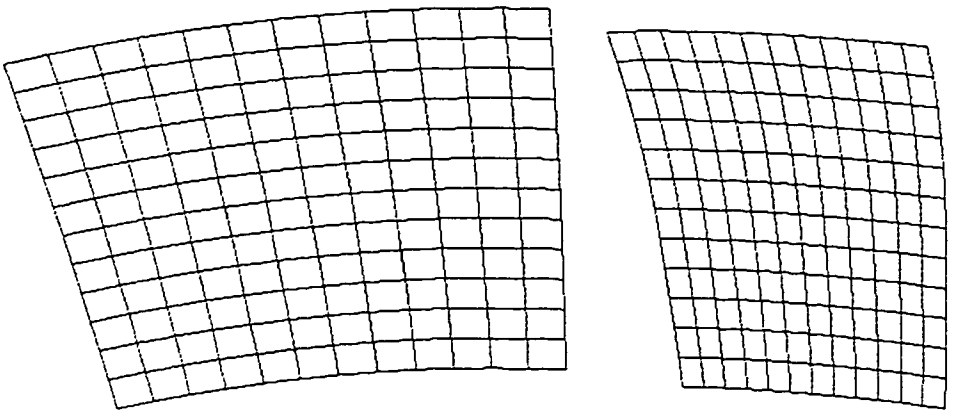

(a) Upstream exit (b) Downstream inlet

Figure 3.1 Mixing plane method illustrated with a turbine stage configuration (a) upstream exit; (b) downstream inlet

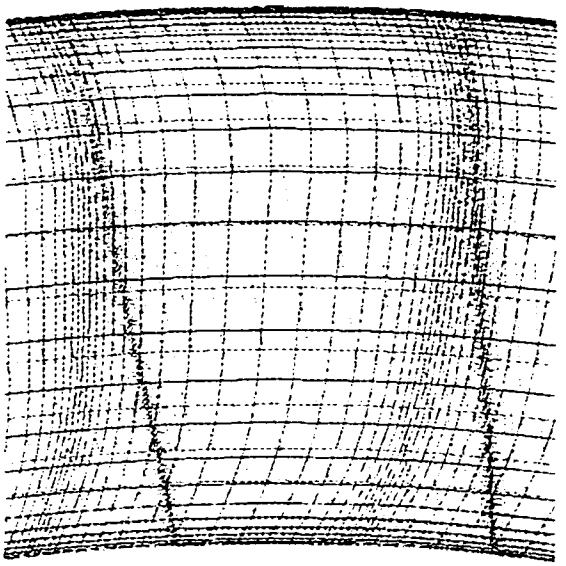

Figure 3.2 Mismatched grid at the rotor-stator interface

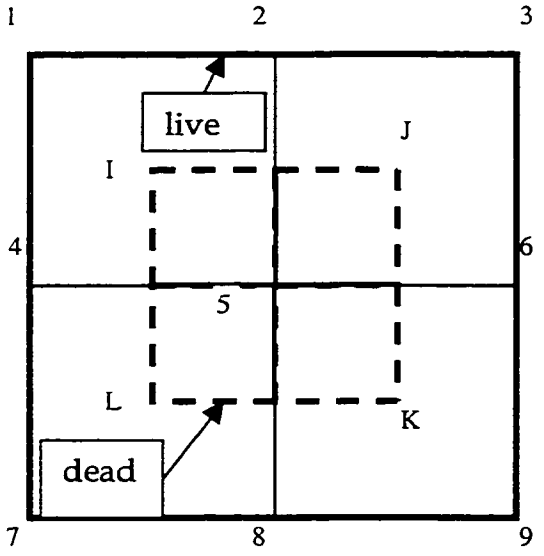

Figure 3.3 Mismatched grid at the interface

4. Solution Procedure

4.1 Introduction

This chapter describes the flow solver algorithm as well as the coupling of the solver with the multistage methodology. The numerical scheme used to iterate for time advance and for the spatial nonlinearity will be discussed. In addition, two separate approaches are described: one for the time-accurate solution of unsteady flows and another for the time marching solution of steady flows [57]. Stabilization details through an artificial dissipation scheme are then detailed. The robustness of the numerical scheme is ensured through the coupling of continuity and momentum equations. Finally, modeling aspects of the near-wall behavior of the turbulence equations, as implemented in the *NS3D* code, are briefly presented because of its novel idea of using a wall finite element to represent the logarithmic law of the wall [58,59].

As discussed in Chapter Two, the nonlinear governing equations are linearized by the Newton method and spatially discretized by the Galerkin finite element method. Furthermore, the time derivatives are discretized by the Gear scheme, a multi-level implicit, hence unconditionally stable method, with controllable accuracy. A second order Gear scheme, assuming two preceding time levels to be available, is used in this current work.

It has been previously demonstrated that the following systems of equations must be solved at each time iteration:

1. A coupled system of the continuity and momentum equations (hereby, Navier-Stokes Equation System)

2. the full energy equation, and
3. the two-equations describing (κ,ω) turbulence model.

4.2 The Navier-Stokes and Energy Equations

The Newton linearization procedure results in a set of linear equations for ρu_r, ρu_θ, ρu_z, and p. The delta form of the assembled equations can be represented symbolically as:

$$[K]\begin{Bmatrix}\Delta\rho\bar{V}\\ \Delta p\end{Bmatrix}=-\begin{Bmatrix}R_{\rho\bar{v}}\\ R_p\end{Bmatrix} \tag{4.1}$$

The continuity and momentum equations (2.2-2.3) are solved in a coupled manner for the mass flux components, ρu_r, ρu_θ, ρu_z, and pressure p. To reduce the overall memory requirements, the energy equation (2.4) is solved for the total enthalpy in a segregated manner.

$$\sum_{e=1}^{nelem}\left[\sum_{j=1}^{ndperl}\left[k_{ij}^{H_0}\right]_{H_0}\Delta(H_0)_j\right]=-Res_{H_0} \tag{4.2}$$

Equation (4.2) is linear and hence simple to solve. This fact can be illustrated by examining the terms in equation (C.6-C.7). In order to construct the coefficient matrix of the energy equation, the density, velocity, and effective conductivity must be known throughout the flow field from the previous iteration, but the total enthalpy does not enter in the construction of the matrix $\left[k_{ij}^{H_0}\right]_{H_0}$. Hence, one Newton iteration is sufficient for the solution of the energy equation.

The total enthalpy field obtained via equation (4.2), along with the velocity field from the Navier-Stokes iteration, are used to update the static enthalpy field.

4.3 The k-ω Turbulence Equations

The discretized form of the (κ,ω) two-equation model, is given by:

$$\sum_{e=1}^{nelem}\left[\sum_{j=1}^{ndperl}\left[k_{ij}^{\kappa}\right]_{\kappa}\Delta(\kappa)_j\right]=-Res_{\kappa} \tag{4.3}$$

$$\sum_{e=1}^{nelem}\left[\sum_{j=1}^{ndperl}\left[k_{ij}^{\omega}\right]_{\omega}\Delta(\omega)_j\right]=-Res_{\omega} \tag{4.4}$$

To reduce the computing cost of solving equations (4.3-4.4), the Jacobian matrices $\left[k_{ij}^{\kappa}\right]_{\kappa}$ and $\left[k_{ij}^{\omega}\right]_{\omega}$ are made identical by considering only the essential, and similar, terms of the $\kappa-$ and $\omega-$equations. Equations (4.3-4.4) yield therefore identical influence matrices but are solved in a sequential manner with (4.3) solved first to update κ, followed by equation (4.4) to update ω, using the updated values of κ and the turbulent viscosity, μ_{turb}.

The solution strategy for these equations consists of an update of the turbulent parameters and the solution of the Navier-Stokes equations for a few Newton iterations, typically five. This sequence is then repeated. At each turbulence update, the (κ,ω) equations are not solved to complete convergence but their residuals reduced by only an order of magnitude. At, or near, the convergence of the coupled system of continuity and momentum equations, the (κ,ω) equations are, however, completely converged.

While a low-Reynolds number (κ,ω) model could be used near walls, it would require an additional resolution of 10 to 20 grid points in the direction normal to the wall at any location within the boundary layer. This would be quite

demanding in terms of solution time and memory, making a Navier-Stokes code a less practical design tool. An alternative is using the wall function approach to describe the high-gradient region near walls through a slip velocity derived from the shear stress at the wall and respecting a certain behavior between that point and the wall. In the present work this slip velocity is given by:

$$\begin{aligned} u^+ &= y^+ && 6 > y^+ > 0 \\ u^+ &= \frac{y^+(20 - y^+) + \left(\frac{1}{s}\ln(y^+) + C\right)(y^+ - 20)}{14} && 20 > y^+ > 6 \\ u^+ &= \frac{1}{s}\ln(y^+) + C && y^+ > 20 \end{aligned} \tag{4.5a}$$

where:

$$s = 0.4184; \quad C = 5.1$$

$$u^+ = \frac{u}{u_\tau}; \quad y^+ = \frac{\rho y u_\tau}{\mu}; \quad u_\tau = \sqrt{\frac{\tau_{wall}}{\rho\,\mathrm{Re}}} \tag{4.5b}$$

For the boundary conditions imposed on (κ, ω) the production and dissipation of turbulent energy at the wall are assumed to be equal. The turbulent shear stress at the wall, τ_{wall}, is obtained from the wall function assumption, equation (4.5), and is used to compute new values for (κ, ω).

While the wall-function approach reduces the number of grid points in the near-wall region, by avoiding the solution of the governing equations in this high gradient region, it proves to be a source of inaccuracy for three-dimensional and separated flows. In *NS3D*, an alternative approach is taken in which a special wall finite element is implemented. This method is similar to [58,59] but is considerably more accurate than wall functions and much less costly than

applying a low-Reynolds number turbulence model. A special wall element, illustrated in figure (4.1), incorporates into its shape function the partially logarithmic behavior of the velocity vector in the direction normal to the wall, equation (4.5), while remaining linear in the other two directions. For elements adjacent to a wall, the velocity shape function in the normal direction to the face of the element lying on the wall is therefore modified to reflect the presumed flow behavior in this region, characterized by a viscous sublayer, a transition layer and a logarithmic outer layer, equation (4.5). For example, for the element shown in figure (4.1), assuming the bottom face to lie on a wall, $F_2(\eta)$ of nodes related to the opposite face, are re-expressed as $F_2\left(\frac{y^+}{y^+_{edge}}\right)$ to reflect a triple deck behavior [58,59].

As for the turbulent viscosity in the near-wall region, it is interpolated as follows: a linear behavior starting at the edge of the near-wall region, where y^+ is assumed to be less than 300, to $y^+ = 30$, and a quadratic variation between $y^+ = 30$ and the wall i.e. $y^+ = 0$.

It must be appreciated that the velocity shape functions in this special near-wall element cannot be integrated accurately using a two-point Gauss quadrature as in the rest of the flow field. Through numerical experimentation, it was determined that nine Gauss points, in the direction normal to the wall, are sufficient to adequately integrate the logarithmic behavior.

4.4 Global Iterative Scheme: Outer Newton Iteration

It is seen that upon advancing to a given time, the Newton linearization leads to the solution of a series of systems of linear equations for $(\rho u_r, \rho u_\theta, \rho u_z, p)$, H_o,

κ and ω. This is referred to as the outer iteration. To solve the linear systems at each Newton iteration, a direct or iterative solver can be used. Since an iterative solver is used here, this solution step is denoted as the inner iteration, to distinguish it from the outer iteration for nonlinearity.

It is worthwhile to note that efficient direct and iterative methods have been developed at the Concordia CFD Lab and P&WC and have been continuously incorporated in the company's code *NS3D*. *NS3D* uses iterative solvers based on the Preconditioned Conjugate Gradient Squared method (PCGS) or the Generalized Minimum Residual Method (GMRES). The necessary preconditioning for these two iterative approaches is obtained through an incomplete factorization process [60-63].

To stabilize the convergence of the Navier-Stokes system of equations at high Reynolds numbers, a strategy with a centered scheme for the continuity equation and artificial viscosity in the cross stream direction is always needed. Here, this extra artificial dissipation is introduced explicitly to the equations and symbolically represented as μ_{art}^{RHS} in equation (4.1).

For an iterative solver is used at each Newton iteration to solve the ill-conditioned linear system coming from the Navier-Stokes equations, it has also been found highly beneficial for the convergence of the iterative scheme to introduce a similar dissipation in the Jacobian matrix itself. This is symbolically represented as μ_{art}^{LHS} in equation (4.1). Equation (4.2), after the introduction of these two concepts, can be re-expressed in the form:

$$[K(\lambda,\mu_{art})]\begin{Bmatrix}\Delta\rho\bar{V}\\ \Delta p\end{Bmatrix}=-\begin{Bmatrix}R_{\rho\bar{V}}(\mu_{art})\\ R_p(\lambda)\end{Bmatrix} \tag{4.6}$$

The solution procedure involves a series of steps in which the amount of artificial dissipation in the numerical scheme is progressively decreased or unloaded. The unloading is usually performed in five steps, resulting in four intermediate solutions as well as the desired final solution which is obtained using the smallest amounts of artificial dissipation possible. Typically, the values specified for μ_{art}^{LHS} in the iterative scheme are greater than those of the residuals of the systems of equations, which represent the problem's physics. This is equivalent to setting up the iteration matrix to be at a lower Reynolds number than that at which the residuals are computed.

4.5 Steady Flow (Time-Marching) and Unsteady Flow (Time-Accurate) Algorithms

There are two solution procedures available in *NS3D*: one solves the steady-flow equations by a time-marching procedure (hereby called steady-flow algorithm, SFA, see flow chart presented in figure 4.2) and the second solves the unsteady flow equations by a time-accurate procedure (hereby called unsteady-flow algorithm, UFA, see flow chart presented in figure 4.3). In both algorithms, the discretized time terms improve the condition number of the system matrix, K, by increasing its diagonal dominance. In the steady-flow case, it provides a mechanism to ensure the convergence of the linear system by allowing the time step size to be dynamically changed, as necessitated by the problem.

4.5.1 Steady Flow Algorithm (SFA)

In the Steady Flow Algorithm, assuming that the initial values of $\rho\bar{V}$ and p are given, the overall residual of the coupled continuity and momentum equations in the L2-norm, $\left\|R_{\rho\bar{V}}, R_p\right\|_o$, can be computed. The SFA has also previously been described as a hybrid artificial viscosity scheme [46]. The outer and inner iterations are carried out as follows:

1. Compute λ^{LHS}, λ^{RHS}, μ_{art}^{LHS} and μ_{art}^{RHS}

2. Solve the turbulence equations every K_{int} Newton iterations and the energy equation every E_{int} Newton iterations, where K_{int} and E_{int} are typically 5 and 1, respectively.

Newton Iteration:

3. Solve $\Delta(\rho\bar{V})_i$ and $\Delta(p)_i$ at each Newton iteration,

$$\left[K\left(\lambda^{LHS}, \mu_{art}^{LHS}\right)\right]\begin{Bmatrix}\Delta\rho\bar{V}\\ \Delta p\end{Bmatrix} = -\begin{Bmatrix}R_{\rho\bar{V}}\left(\mu_{art}^{RHS}\right)\\ R_p\left(\lambda^{RHS}\right)\end{Bmatrix} \tag{4.7}$$

4. Update $\rho\bar{V}$ and p:

$$\begin{Bmatrix}(\rho\bar{V})_{i+1}\\ (p)_{i+1}\end{Bmatrix} = \begin{Bmatrix}(\rho\bar{V})_i\\ (p)_i\end{Bmatrix} + \begin{Bmatrix}\Delta(\rho\bar{V})_i\\ \Delta(p)_i\end{Bmatrix} \tag{4.8}$$

until $\dfrac{\left\|R_{\rho\bar{V}}, R_p\right\|_{i+1}}{\left\|R_{\rho\bar{V}}, R_p\right\|_o} < TOL$, a specified convergence criterion

repeat from step 1.

The hybrid artificial viscosity scheme is a key feature in allowing large time steps, making the use of iterative methods viable for steady-state problems.

4.5.2 Unsteady Flow Algorithm (UFA)

In the Unsteady Flow Algorithm, the values of $\rho\bar{V}$ and p are assumed to be given at an initial time t and, hence, $\left\|R_{\rho\bar{V}}, R_p\right\|_o$ can be computed. It should be noted that UFA may also be used for steady-state problems. At each time step, the solution procedure is as follows:

1. Solve the turbulence equations every K_{int} Newton iterations and the energy equation every E_{int} Newton iterations, where K_{int} and E_{int} are typically 5 and 1 ,respectively.

Newton Iteration:

2. Solve $\Delta(\rho\bar{V})_i$ and $\Delta(p)_i$ at each Newton iteration:

$$\left[K\left(\lambda^{LHS}, \mu_{art}^{LHS}\right)\right]\begin{Bmatrix}\Delta\rho\bar{V}\\ \Delta p\end{Bmatrix} = -\begin{Bmatrix}R_{\rho\bar{V}}\left(\mu_{art}^{RHS}\right)\\ R_p\left(\lambda^{RHS}\right)\end{Bmatrix}$$

5. Update $\rho\bar{V}$ and p:

$$\begin{Bmatrix}(\rho\bar{V})_{i+1}\\ (p)_{i+1}\end{Bmatrix} = \begin{Bmatrix}(\rho\bar{V})_i\\ (p)_i\end{Bmatrix} + \begin{Bmatrix}\Delta(\rho\bar{V})_i\\ \Delta(p)_i\end{Bmatrix}$$

$$\text{until } \frac{\left\|R_{\rho\bar{V}}, R_p\right\|_{i+1}}{\left\|R_{\rho\bar{V}}, R_p\right\|_o} < TOL,$$

4. Advance solution in time, repeat from step 1.

4.6 Coupling of Flow Solver with Multistage Methodology

In steady multistage analysis, the mixing plane algorithm is coupled to the steady flow algorithm. The averaging procedure is first applied to both the exit plane of the upstream blade row and the inlet plane of the downstream blade row to extract the so-called "mixed-out" flow properties from the current numerical solution. The proper interface boundary conditions are then specified. Circumferentially-averaged radial profiles of absolute total temperature, density, radial velocity, absolute tangential velocity and axial velocity, which are obtained from the solution of the upstream blade row, are specified as the inlet boundary conditions at the downstream blade row. The circumferentially "mixed-out" static pressure, obtained from the solution at the inlet of the downstream blade row, is then specified as a boundary condition at the exit plane of the upstream blade row. The above procedure is repeated at each Newton iteration until the residuals of the governing equations are reduced by three orders of magnitude, and the mass flow rates and the circumferentially-averaged radial profiles, obtained from the upstream and downstream blade rows, are matched within a user-specified tolerance.

In unsteady multistage analysis, the solution is advanced in time using the Gear scheme with second order accuracy in time. The solution of the live side of the interface is updated, at each Newton iteration, via the flow solver while the solution on the dead side is interpolated from that of the live side. The solution of the time-dependent system of equations is updated to the next time level when the residual is reduced by two orders of magnitude or when the maximum number of Newton iterations per time step is attained. This procedure is then repeated and the solution time history is stored over one full period at selected grid points in the computational domain. At every time step, the time history is

checked to detect if time periodicity has been achieved. The time stepping is terminated only if the solution has converged to a time periodic response or the maximum number of time step is reached.

FIGURES

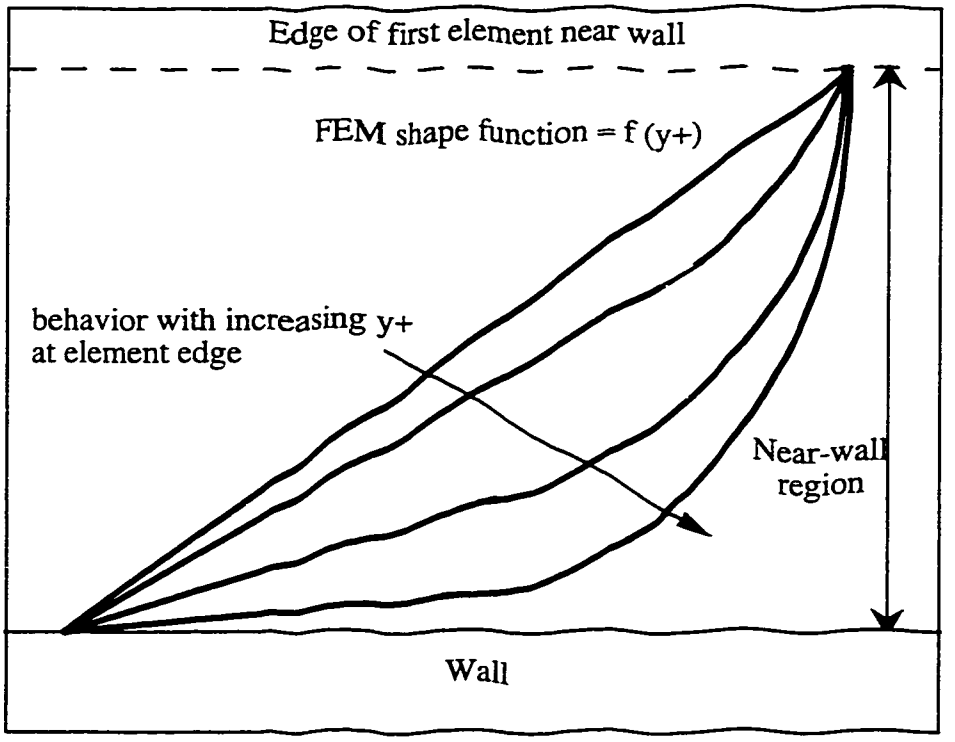

Figure 4.1 Wall element with logarithmic shape function

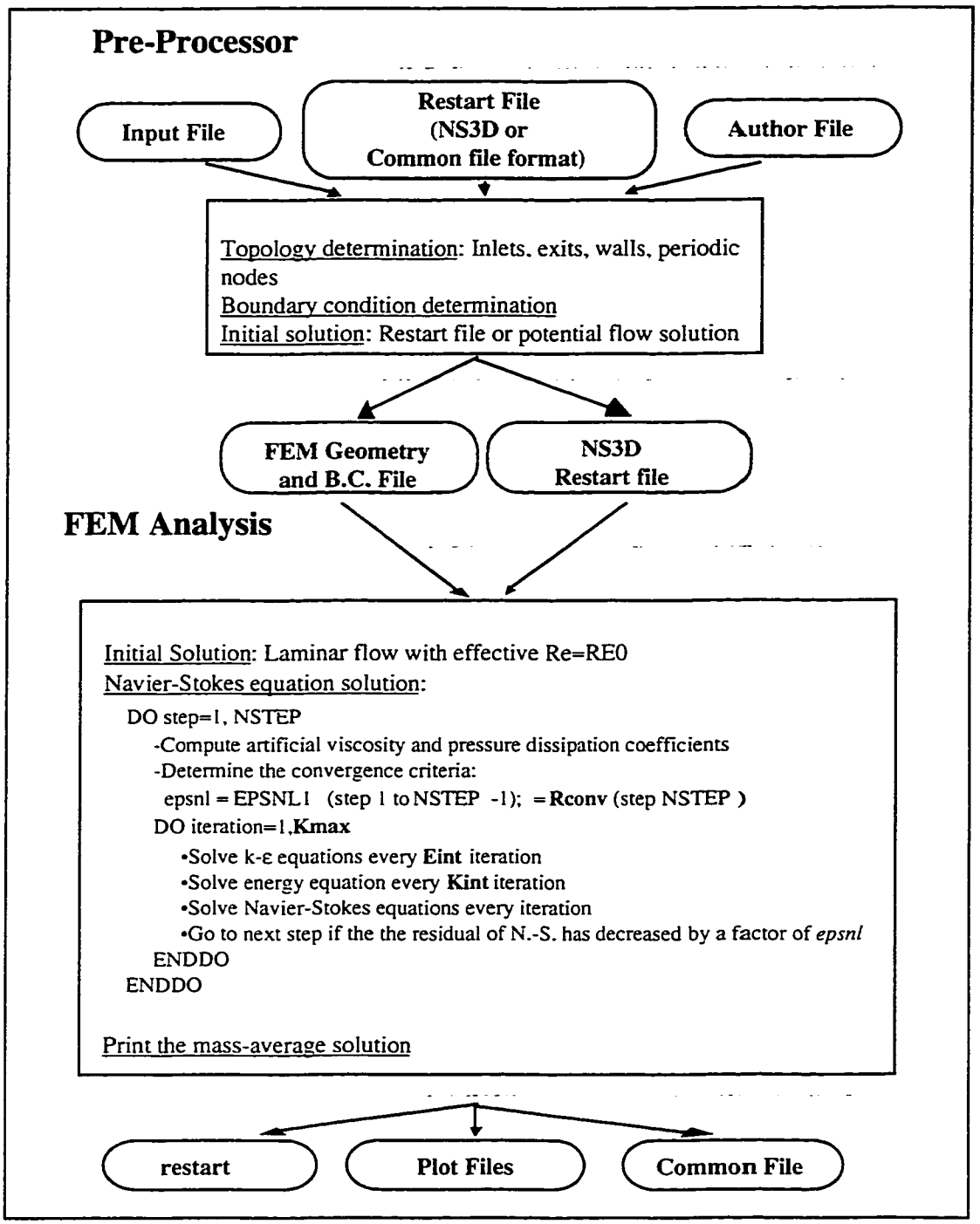

Figure 4.2 Algorithm flowchart for steady flow scheme

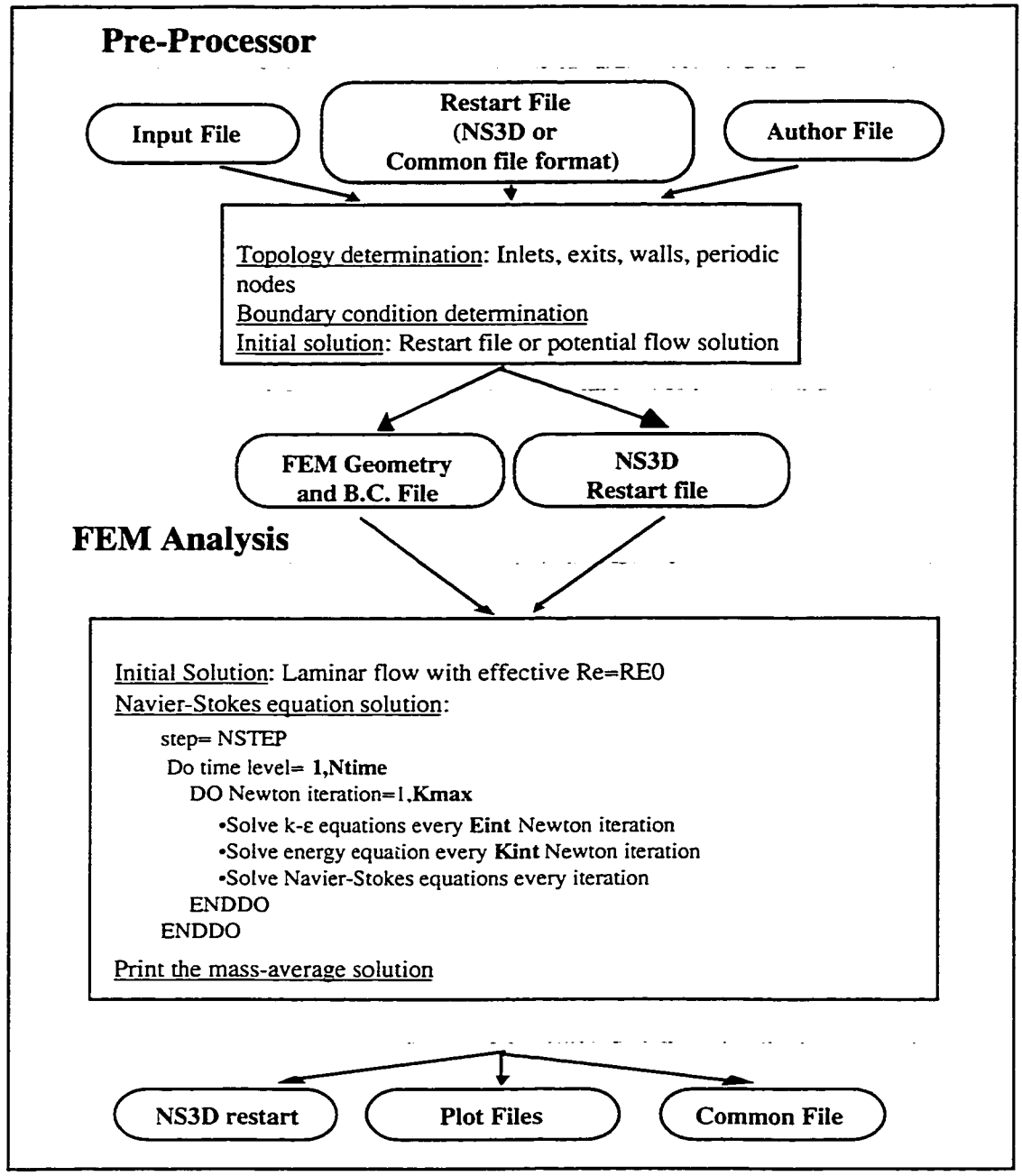

Figure 4.3 Algorithm flowchart for unsteady flow scheme

5. Numerical Results

5.1 Summary of Test Cases

Numerical results from five test cases are presented to validate the current work. All but one of these cases possess very complex geometries and are in fact actual engine stages. The predictions span the full range of the transonic flow regime, be it inviscid, viscous, laminar, turbulent, steady or unsteady. The test cases have been validated against engine data when available.

When performing a numerical simulation it is important to evaluate the sensitivity and dependency of the numerical solution of turbomachinery stages on grid parameters. These parameters comprise the grid density, and the its distribution in regions where flow features such as shocks, wakes, and separation zones are present. One, ultimately, aims to obtain a grid-independent solution and this may be achieved through grid adaptation [7]. In this work, however, the PWC in-house grid generation system for the analysis of turbomachinery flows, which is based on engineering and design experience of gas turbines, has been used to generate the grids for all test cases presented in this Thesis. It has been found that the numerical prediction on these "calibrated" meshes has consistently compared well with available engine data; hence it is believed that the effects of grid dependence on the numerical results have been minimized.

Section 5.2 describes numerical predictions of the mixing plane method on the second stage of the United Technologies Research Center (UTRC) Large-Scale Rotating Rig (LSRR) low-speed axial flow compressor. This low Mach number test case, which is selected due to the availability of extensive experimental data

[64], investigates the capability of the two-equation (κ,ω) turbulence model in predicting the corner stalls near the endwalls of the second stator, which has been observed experimentaly.

Section 5.3 provides an analysis of the numerical results obtained on a first stage HP compressor of a PWC turboprop engine. This is a high Mach number case with shocks emanating off the rotor leading edge region. The predicted results are compared to those of the mean line model at PWC, as well as to other numerical results. In Section 5.4, further analysis of the same test case is then conducted with the second stage compressor of the same turboprop engine so as to introduce an additional mixing plane. Thus, the two-stage analysis comprises four blade rows and, hence, three mixing planes: the first rotor followed by the first stator as the first stage, followed by a second rotor and second stator as the second stage. The aim of this test case is to predict the overall performance characteristics of the two-stage axial flow compressor such as choking line, stall, maximum efficiency, pressure ratio and temperature ratio versus corrected mass flow rate.

Section 5.5 presents the steady analysis of the complex geometry of a centrifugal stage compressor, specifically an impeller-vane diffuser configuration in which the flow enters the impeller axially and exits radially. The gap between the impeller and the diffuser is extremely small and the physics of the flow field in the gap region is not well understood. It has been established in the literature that the the mixing plane methodology provides a good prediction of the performance characteristics, such as pressure ratios and efficiencies, of axial turbomachines at their design points. The objective of this particular test case is

to test the applicability of this method to centrifugal stages and assess its performance in analyzing the complex flow features.

Section 5.6 examines laminar flow over a circular cylinder at Re=100. This important test case serves to validate the accuracy of the time discretization scheme in the *NS3D* code as well as the mismatched grid methodology, which has been applied in the unsteady multistage simulation of test cases with equal and unequal blade counts or pitches. The mesh of the flow over the circular cylinder consists of two sections. The first section includes the region upstream of the cylinder, the cylinder region, and a small region downstream of the cylinder surface. The second section comprises the remainder of the downstream region and, hence, the remainder of the computational domain. The meshes at the interface plane, common to both sections of the mesh, are non-conforming in the y- and z- directions. Thus, the desired outcome of completely mismatched grids at the interface plane would have been achieved. Such grids are required in the analysis of unsteady rotor-stator interaction whereby grids need to move relative to one another.

Section 5.7 provides unsteady flow predictions on the centrifugal stage configuration presented in section 5.5. This test case meets several objectives:

i. comparison of the results between steady and unsteady analysis;
ii. a better understanding of the flow physics in such turbomachinery components and a means to gauge the importance of unsteady effects on the performance of the impeller as well as the diffuser.
iii. It is also believed to be the first application of rotor-stator interaction to centrifugal machines

Section 5.8 presents the time-inclined unsteady results of wake-rotor interaction test cases in which the pitches of the rotor and wake differ. This cases serves to validate the post-processing method which maps the solution from the computational plane (r',θ',z',t') into the physical plane (r,θ,z,t).

5.2 Steady Analysis on the UTRC Axial-Flow Compressor

The multistage mixing plane method has been demonstrated for the second stage compressor of the UTRC large-scale rotating rig, at an rpm of 650 and a flow coefficient of 0.51. The results compare very well to the available experimental data and demonstrate the potential of this method for multistage application. It is considered a difficult test case, not only because of the incompressible nature of the flow field, but also due to the presence of corner stalls near the endwalls of the stator [64,65].

The rotor grid uses 25 points upstream of the blade, 55 points on the blade and 12 points downstream. There are 30 points in the hub-to-shroud direction and 29 points in the blade-to-blade direction. The stator grid uses 14 points upstream of the blade, 57 points on the blade and 15 points downstream. There were 25 points in the hub-to-shroud direction and 21 points in the blade-to-blade direction. The rotor tip clearance/chord is 1% and there is no stator hub clearance. To ensure the quality of the grids used in this test case, a grid adaptation procedure was applied to the stator grid in [7] and the results of static pressure recovery, flow angles and normalized axial velocity at inlet and exit planes of the stator indicate that the grids are near-optimal.

As shown in figure 5.1 the rotor inlet is located at station 3 and the stator exit at station 5. Station 4 represents the interface mixing plane between rotor and

stator. Station 3 is situated at 24% of the rotor axial chord upstream of the rotor leading edge, while station 4 is located at 30% of the rotor axial chord downstream of the rotor trailing edge and 19% of the stator axial chord upstream of the stator leading edge. Station 5 is located at 18% of the stator axial chord downstream of the stator trailing edge. The rotor and stator possess 44 blades each.

The analysis is performed with the inlet conditions at station 4 (that is, the exit of rotor and inlet of stator) determined iteratively. Each component is first converged separately in terms of mass. Interaction then begins between the adjacent rows. The proper mixed-out radial profiles are calculated at the planes corresponding to the interface, from each side. The new inlet variables to the downstream component consist of rothalpy, components of mass flux-scaled to correspond to the inlet mass flow rate in the far upstream component, and turbulent quantities, whereas the new exit variable to the upstream component is the radial static pressure profile. Both inlet and exit variables are obtained by suitably under-relaxing the changes at the nodal values from the previous iteration. This interaction then continues at each Newton nonlinear iteration until convergence for all blade rows is reached. In figures 5.2a-5.2g, comparisons between the measured and computed rotor pressure distributions are made at 3%, 14%, 26.9%, 45.1%, 73.4%, 86.1% and 95.5% span, respectively. The comparison is very good from leading to trailing edges, at all sections.

Figure 5.3 shows the radial profile for the total pressure loss coefficient of the rotor. The loss is well predicted, even near the end walls. Figures 5.4-5.5 depict the spanwise distributions of axial velocity, and relative flow angles at stations 3 and 4 of the rotor. Predictions for flow angles at station 3 compare extremely well

with the experimental data. At station 4, however, the numerical results are underpredicted in the hub region.

In figures 5.6a-5.6g comparisons between the experimental and numerical stator pressure distributions are made at 3%, 14%, 26.9%, 45.1%, 73.4%, 86.1% and 95.5% span, respectively. The comparison is good from hub to tip, with the numerical solution clearly indicating the region of separation on the suction side at the 3% span section.

Figure 5.7 reveals the spanwise total pressure loss coefficient of the stator. Comparisons between the numerical and experimental radial profiles of axial velocity, and absolute flow angles at stations 4 and 5 of the stator are depicted in figures 5.8-5.9. The numerical prediction of these quantities is accurate despite the small pressure ratio of this case, which gives little variation in the total pressure profiles, leading to some inaccuracy in being able to define the loss.

Figures 5.10-5.11 compare both the total and static pressure coefficients at stator inlet and exit (stations 4 and 5). The numerical results are in very good agreement with the experimental data [64].

5.3 Steady Analysis on a Turboprop's First HP Stage Axial Compressor

NS3D multistage analysis results for a PWC turboprop first HP stage axial compressor at 43,500 rpm are presented. This high Mach number test case is characterized by shocks near the rotor leading edge. Comparisons of the numerical predictions are made with those of the mean line model at PWC as well as to other numerical results obtained by a proprietary viscous compressible

flow solver, which is explicit, multi-grid, and finite-volume-based with k-ε as its turbulence model [66].

The multistage analysis procedure is detailed below:

1- Inlet boundary conditions, which include inlet radial distributions of total temperature To, total pressure Po, Mach number M, inlet gas angle α, and cone angle ϕ, and exit boundary conditions which include radial distribution of static pressure p for each blade row, are obtained from an axisymmetric inviscid through-flow analysis.
2- An inviscid (Euler) grid for each blade row is generated and the flow field is initialized based on the through-flow results obtained from step 1.
3- A viscous grid for each blade row is then generated and a viscous flow field is initialized, axisymmetically, based on the restart solution obtained in step 2.
4- Single-component viscous calculations are carried out using *NS3D* with the restart solution obtained in step 3 as an initial solution.
5- Multistage computations are then performed using *NS3D*. This step is usually combined with step 4 in the same analysis.

In this analysis, tip clearance effects are neglected and the finite element mesh used is shown in figure 5.12. The rotor grid contains 43,750 nodes with 25 nodes in the spanwise direction, 25 nodes in the pitchwise direction, 21 nodes upstream, 41 nodes on the blade, and 10 nodes downstream. The stator grid contains 46,250 nodes with 25 nodes in the spanwise direction, 25 nodes in the pitchwise direction, 10 nodes upstream, 41 nodes on the blade, and 25 nodes downstream.

Converged single-blade viscous solutions for the rotor and the stator are obtained before the interaction process between the rotor and the stator begins. It has been observed that the multistage calculations cannot be started unless the percentage change in static pressure at the mixing plane, common to the rotor and the stator, falls below 20%.

The convergence history of the Navier-Stokes equations for both the rotor and stator as a stage is shown in figure 5.13. The L2-residual for the rotor is two orders of magnitude greater than that of the stator. Approximately 450 Newton iterations are sufficient to reduce the residuals of the governing equations by three orders of magnitude for both blade rows. Convergence of the stage calculation is, however, not only based on the residuals, but also on the percentage change of physical quantities such as static pressure, total temperature, and mass flow across the mixing plane. Stage calculations are terminated when the percentage change in mass flow, area-averaged static pressure, and mass-averaged total temperature at the mixing plane are less than 0.2%, 0.5%, and 0.1%, respectively. Plots of the percentage change in mass flow versus iteration number for each rotor and stator are depicted in figure 5.14a and 5.14b, respectively.

Figure 5.15 shows the map predictions for the first rotor by *NS3D*, meanline model and the proprietary code. Due to the lack of test data for the first rotor, the results obtained by *NS3D* and the proprietary code are compared with those of the meanline. As displayed in figure 5.15, the *NS3D* results are in better agreeement with the meanline than those obtained by the proprietary code. The proprietary code over-predicts choking flow by 2.1%, peak efficiency by 1.39%,

and pressure ratio by 3.27% while *NS3D* over-predicted choking flow by 1.03%, under-predicted efficiency by 1.25% and over-predicted pressure ratio by 2.4%.

Figure 5.16 shows the map predictions for the first turboprop's compressor stage by *NS3D*, the meanline model, and the available test data. *NS3D* predictions are compared with test data at the choking flow condition and to meanline model predictions at non-choking conditions. The choking flow is over-predicted by 1.03% with respect to the test data. The stage isentropic efficiency is under-predicted by 0.97% and the pressure ratio is over-predicted by 1.98% with respect to the meanline model.

The discrepancies observed with the Thesis predictions can be explained as follows:

1- The coarse mesh used in the present analysis may not be fine enough to resolve the flow.
2- Tip clearance, which has not modeled in the present analysis, should reduce the predicted choking flow.

5.4 Steady Analysis on a Turboprop's Two-Stage HP Axial Compressor

A two-stage analysis, with tip clearance, of a PWC turboprop HP axial compressor at 43,500 rpm is carried out using *NS3D*. A compressor map is obtained and the numerical results are compared with experimental.

All the blade rows in this case were analyzed using medium size grids since fast workstations were not available. A midspan section of the two-stage

configuration is depicted in figure 5.17 with the first rotor, first stator, second rotor and second stator grids consisting of 81,780, 73,080, 73,080 and 73,950 nodes, respectively for a total of 301,890 nodes. Six grid points are used in the spanwise direction and three points inside the blade for tip clearance. The same number of grid points is used for all other blade rows.

Converged single-blade viscous solutions for each row are obtained before the interaction procedure among adjacent components is initiated. Five solutions are then obtained by changing the static pressure at the exit of the compressor, that is, the exit plane of the second stator. The first solution corresponds to the lowest static pressure at the exit of the compressor, also the choking condition. The second solution is obtained by solving with *NS3D* for about 250 iterations with the first solution as an initial guess. The remainder of the solutions are started from previous solutions with different static pressures at the compressor exit. Stage calculations are terminated when the difference in mass flow and mixed out quantities (static pressure, total temperature, and total pressure) at the mixing plane are less than 0.1%, and 0.4%, respectively.

Figure 5.18 shows the map predictions for the two-stage compressor by *NS3D*. It can also be observed from this figure that *NS3D* over-predicts choking flow by 0.44%, under-predicts efficiency by 2.16% and under-predicts pressure ratio by 0.2% with respect to the experimental data at the design corrected flow.

Figure 5.19 compares *NS3D* radial profiles of absolute flow angle and normalized total temperature at the exit of compressor to experimental values. It is apparent from figure 5.19 that both the normalized temperature and exit flow angle are

slightly over-predicted in the end-wall regions. However, the overall prediction compares very well with the experimental data.

One reason for the observed discrepancies in the Thesis predictions may be the coarseness of the grids.

5.5 Steady Stage Analysis on a Centrifugal Compressor Stage

Steady mixing plane analysis is conducted on a centrifugal stage, comprising an impeller and a vane diffuser, shown in figure 5.20. An important objective of this selected test case is to extend the applicability of this method to centrifugal stages and assess its performance in analyzing its complex flow features.

The flow at the inlet of the impeller is subsonic with a Mach number of 0.4 and a swirl relative to the axial direction ranging from zero to 30 degrees. The total pressure ratio across the impeller varies from 2.5 to 10. The flow at the exit of the impeller is primarily circumferential due to the high swirl of the flow (75 degrees with the radial direction since the flow enters the impeller axially and exits radially). The impeller increases the fluid's kinetic energy, resulting in a high speed flow with Mach numbers in the range of 0.85-1.2. The flow enters the vane diffuser where its kinetic energy in converted into pressure energy via a diffusion process characterized by a static pressure rise and an accompanying drop in velocity, to a Mach number of approximately 0.15. The total loss in the diffuser is about 10%.

Two simplifications were made to the impeller-diffuser geometry [70]. First, a vane diffuser is analyzed despite the fact that all PWC engines employ a pipe diffuser. This is done simply to reduce the grid size since a pipe diffuser would

require at least twice the grid size of a vaned diffuser. As a preliminary step, one is also interested in studying the qualitative behavior of the interaction which would be similar for both vane diffusers and pipe diffusers. Secondly, the blade/diffuser count is altered in this case to produce a one to one ratio (figure 5.21). The total grid contained 202,140 nodes with 137,340 in the impeller and 64,800 in the vaned diffuser. It should be noted that the impeller tip gap is modeled and the diffuser does not have a de-swirl cascade at the exit.

At the inlet, the total pressure, total temperature and flow angles are specified. At the exit of the diffuser, a constant static pressure is specified. Approximately, 500 Newton iterations are performed to resolve the non-linearity of the governing equations and match the axial profiles at the interface plane in the gap region between the impleller and the diffuser.

The flow in the interaction region is best viewed by aligning along the engine axis. Figure 5.22 reveals the Mach contours from such a vantage point. As shown, the flow separates right off the leading edge of the diffuser. The results make sense as the flow coming out of the impeller is far from uniform leading to an incidence on the diffuser of 10 degrees or more. Classical cascade theory, however, suggests that the incidence tolerance of the diffuser is no more than two degrees, thus the large separation obtained in the steady analysis is not surprising.

Figure 5.23 shows radial velocity contours obtained from a steady analysis as they develop through the back end of the impeller. The profile is typical of any steady analysis, showing strong flow near the hub and a relatively dead zone near the shroud.

The discrepancy between the mixing plane results and the engine performance data is attributed to the diffuser static pressure rise obtained with such a large separation zone. These results suggest that unsteady effects are significant and may have a first order effect on the solution, rendering the use of a mixing plane steady analysis inappropriate. An unsteady analysis would be more realistic in an engine environment as will be demonstrated in section 5.7.

5.6 Flow Past a Circular Cylinder at Re=100

This test case investigates laminar flow over a circular cylinder for the purposes of validating the time discretization scheme, as well as the mismatched grid methodology described in this work. The computational domain and the boundary conditions are presented in figure 5.24. The mesh has 37,920 nodes and 30,702 elements (figure 5.25). The grid over the cylinder is divided into two regions which share an interface plane (figures 5.25 and 5.26). The interface is normal to the x-direction and located several diameters behind the cylinder. The grid in the first region, to the left of the interface, has 38x58x8 nodes in the x-, y-, and z-directions, respectively, while the grid in the second region, to the right of the interface plane, has 25x64x10 nodes in the x-, y-, and z-directions, respectively. The mismatched grids at the interface plane from the left and right regions are illustrated in figure 5.26a while finer mesh details near the cylinder wall surface are shown in figure 5.27.

The analysis begins with a steady-state calculation, at Re=100, using the steady flow algorithm, SFA, with no artificial viscosity. The time-accurate calculation is then started from this steady-state solution. The second-order Gear method, with a time step $\Delta t=0.23$, was applied, which corresponds to approximately 25 time steps per shedding cycle. At each time step, 6 Newton iterations were found to

be sufficient to reduce the residuals of the Navier-Stokes equations by two orders of magnitude. The convergence history of the unsteady Navier-Stokes equations for flow past a circular cylinder at Re=100 is displayed in figure 5.28, with the peaks and troughs corresponding to the start and end of a time step, respectively.

In figure 5.29 the evolution of the transverse velocity v is plotted versus time at x/D = 0.65 downstream from the cylinder along the symmetry line y = 0. The Strouhal number, $Sr=fD/V_\infty$, is computed by measuring the vortex shedding period based on the transverse velocity v from figure 5.29 and is found to be within 5% of the experimental one given in [67]. It was also found that the horizontal velocity oscillates at twice the shedding frequency. The flow is periodic, with a period of T=5.75, and as shown in figure 5.30, the contours of transverse velocity are continuous across the interface plane where the grids are totally mismatched. Figure 5.30 shows the transverse velocity contours of vortex shedding behind the cylinder during a period of 6.0 (about 1.05 cycle). The global flow field is saved at five equally spaced time levels, covering one cycle of vortex shedding.

Table 5.1 Numerical and experimental data for the flow past a circular cylinder at Re=100

	T	Sr
Present work (conforming grids)	5.750	0.174
Present work (non-conforming grids)	5.750	0.174
Li et al. [68]	6.133	0.163
Gresho et al. [69]	5.600	0.180
Exp. [67]	6.024	0.166

Comparison of the principal parameters of the flow over the circular at Re=100 are presented in Table 5.1. The period of vortex shedding T, the Strouhal number Sr, at the points, x/D = 0.65 on the centerline behind the cylinder obtained from the present work are in good agreement with the numerical results of [68,69] and the experimental measurements of [67].

5.7 Unsteady Stage Analysis on a Centrifugal Compressor Stage

An unsteady stage analysis is conducted on the same centrifugal stage presented in section 5.5 to study the effect of unsteadiness on impeller performance.

As carried out in the steady analysis, the total pressure, total temperature and flow angles are specified at the inlet of the impeller, and a constant static pressure is specified at the exit of the diffuser. At each time step, 5 Newton iterations are performed to resolve the non-linearity of the governing equations. There are 70 time steps per blade-passing period.

The solution is restarted several times and it is not clear exactly how many time steps are carried out since only the last output file has been retained, which ran for 700 time steps. It is quite likely that more than 2000 time steps were performed, which represent 10,000 Newton iterations. Even with such a large number of time steps, a solution with a temporal periodicity of the blade-passing frequency is never achieved.

It is worth mentioning that both the steady and unsteady analyses, which are carried out on the same grid size, have the same memory requirements as well as the same computing cost per Newton iteration. This implies that the computing

time required for an unsteady analysis is approximately 20 times longer than that of the steady analysis.

Figure 5.31 reveals a comparison of Mach contours between the steady and unsteady analysis. As shown, there is a modest sized separation zone on one side of the diffuser, resulting in a large qualitative difference in the two results.

Another interesting effect seen in the analyses is the difference in the flow fields emerging from the impeller in the unsteady and steady analyses. Figure 5.32 shows radial velocity contours obtained from a steady and unsteady analysis. It is observed that the unsteady velocity profile has changed substantially from the steady results with the highest velocity flow now being in the shroud region when the flow leaves the impeller.

Figure 5.33a shows the instantaneous static pressure contours at an axial cut through the centrifugal stage. The pressure does not rise smoothly through the diffuser, but has a wave pattern. A videotape of the pressure field shows that these waves move up the diffuser. Figure 5.33b plots the instantaneous static pressure midway between the diffuser from the throat to the trailing edge. The wave pattern is clearly visible.

Large pressure fluctuations in a diffuser have been observed experimentally [71]. These pressure waves may be responsible for the difficulty in achieving a time periodic flow field. The pressure wave moves downstream and reflects off the walls and at the exit, sending waves upstream. The frequency of these waves can be completely different from the blade passing frequency, resulting in a very complicated flowfield where the temporal periodicity may be very different than

the blade passing frequency.

The unsteady calculations also reveal a difference in the pressure field. In a steady analysis the leading edge stagnation point pressure field radiates out from the leading edge in a direction that lines up with the incident flow. Figure 5.34 shows the pressure field at an instant in time from the unsteady analysis. The direction of the pressure gradient has a very strong radial bias even though the incident flow is predominately tangential. An explanation for this behavior can be found if one considers the effect that the impeller must have on the time averaged flow field. In an impeller flow that is steady in the relative frame there is an equivalence between the tangential direction and time, namely that $d\theta = \Omega dt$ where θ is the tangential direction, Ω is the impeller rotation speed and t is time. The time averaged flow field is thus constant in the θ-direction allowing a gradient only in the radial direction. The stagnation point pressure field from the diffuser is strongly influenced by this fact giving it the radial bias [72].

Fourteen solutions are saved equally spaced in time over one blade-passing period. These results are post-processed and time-averaged to give an overall impeller performance. The unsteady solution has an inlet corrected flow that is lower by 8.25% from the steady one. The unsteady results are scaled to determine the appropriate steady results. The downstream station is a plane halfway between the impeller trailing edge and the diffuser leading edge.

The steady and unsteady results are similar in terms of overall performance except for a difference in the total pressure. This indicates that the blockage is noticeably lower in the unsteady analysis. Figure 5.35 shows the magnitude of

the radial velocity at the impeller exit for the steady and unsteady analyses and the flow is, indeed, more uniform in the unsteady analysis.

Figure 5.36 shows the unsteady fluctuations in area averaged total pressure ratio, static pressure ratio and mass-averaged total temperature ratio at the interface. The results for two periods are plotted although only one was actually calculated and the results repeated. As noted earlier, the actual temporal periodicity of this problem is not the blade passing frequency. The largest fluctuation is in the total pressure. The static pressure fluctuation is considerably lower than that shown in figure 5.35, indicating that the diffuser amplifies the static pressure fluctuations. This is consistent with the experimental results in [71].

5.8 Wake-Rotor Interaction

The purposes of this test case are two-fold: (i) to demonstrate the capability of the time-inclined method to analyze wake-rotor interaction in which the pitches of the rotor and wake differ and (ii) to validate the post-processor which maps the solution from the computation plane (r',θ',z',t') discussed in Chapter 3 into the physical plane (r,θ,z,t). Two cases are analyzed with different number of wakes striking the rotor. The first case has 66 stator wakes and 72 rotors, while the second has 60 wakes and 72 rotors. This results in a pitch ratio of 1.091 and 1.2 for the first and second cases, respectively. Results for the case with a pitch ratio of 1.2 are presented in this Thesis.

First, a steady inviscid solution is obtained for the turbine stage using the mixing plane method. The steady boundary conditions $U(r,z)$ from the steady analysis are applied, after being modified, and are used to carry out an unsteady computation in the inclined plane. The rotor grid consists of 21,021 nodes with 13

nodes in the spanwise direction, 13 nodes in the pitchwise direction, and 49 nodes in the streamwise direction. Table 5.2 lists the relevant flow parameters for this case. The unsteady calculations use 600 time levels with 50 time steps per blade-passing period to resolve the temporal periodicity of the flow. At every time step, five Newton iterations are used to reduce the residual by two orders of magnitude. The flow attains a perfect time periodic solution after only three cycles which is equivalent to 150 time steps.

Table 5.2 Parameters for wake-rotor interaction test case

Inlet relative Mach number	0.73
Exit relative Mach number	0.80
Inlet absolute flow angle (deg)	-60.0
Stator-to-rotor pitch ratio	1.2
Wake velocity defect	0.1

The incoming wakes are specified at the rotor inlet boundary by applying the following sinusoidal function for the momentum vector $\rho\bar{V}$:

$$U(r,\theta,z,t)= U(r,z)[1-D\cos(2\pi\eta)]$$

where $\eta=\frac{\theta+\Omega t}{\theta_S}$ and D is the wake velocity defect and typically has a value of 0.05. Transforming η from the physical space into the computation space yields

$$\eta=\frac{\theta+\Omega(t'+\lambda_r\theta)}{\theta_S}=\frac{\Omega t'}{\theta_S}+\frac{\theta}{\theta_S}+\frac{\Omega\lambda_r\theta}{\theta_S}=\frac{\Omega t'}{\theta_S}+\frac{\theta}{\theta_S}+\frac{(\theta_S-\theta_R)\theta}{\theta_R\theta_S}=\frac{\Omega t'}{\theta_S}+\frac{\theta}{\theta_R}$$

It is clear that the flow in the inclined time plane has a time periodicity equal to

the rotor blade-passing period defined as $T_R = \frac{\theta_S}{\Omega}$, and more importantly, a spatial periodicity equal to the rotor pitch angle θ_R and, hence, one rotor passage is required to perform the computation, even with the differing values of wake and rotor pitches. The flow solution is saved at 50 equally spaced timesteps in the computation space covering a full period. The post-processor is run to produce 20 solutions per period in the physical space. A video is then produced using the commercial post-processing software, Fieldview. Plots for relative Mach number at different physical time steps are shown in figure 5.37. As shown, the same flow phenomena takes place in one passage as in the neighboring passage, after a time span ΔT equal to the time lag. The actual spatial periodicity is over (60 stators/12) five wakes which is equivalent to (72 rotor /12) six rotor passages. Therefore, five incoming wakes on a configuration consisting of six rotor passages is sufficient to fully describe the flow field in this case.

FIGURES

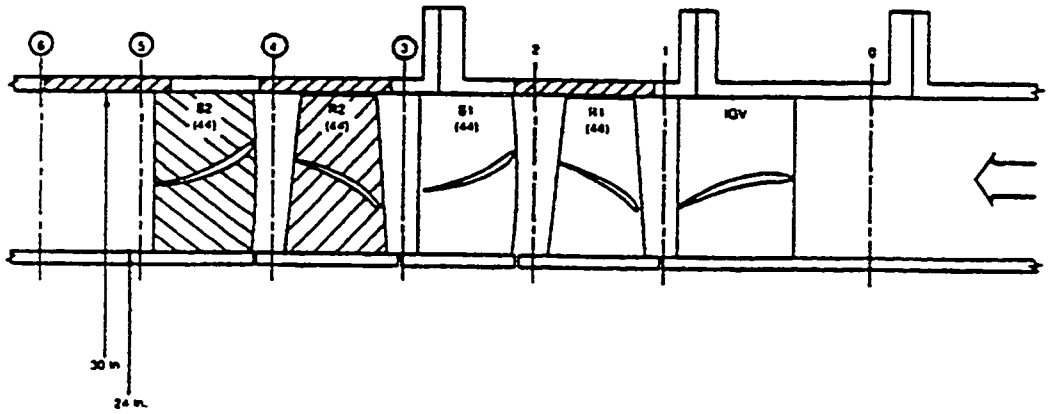

Figure 5.1 The UTRC 2.5 stage compressor model

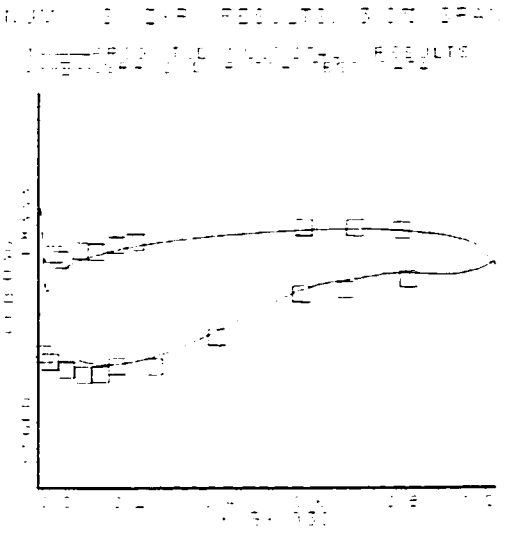

Figure 5.2a Rotor Cp at 3% span

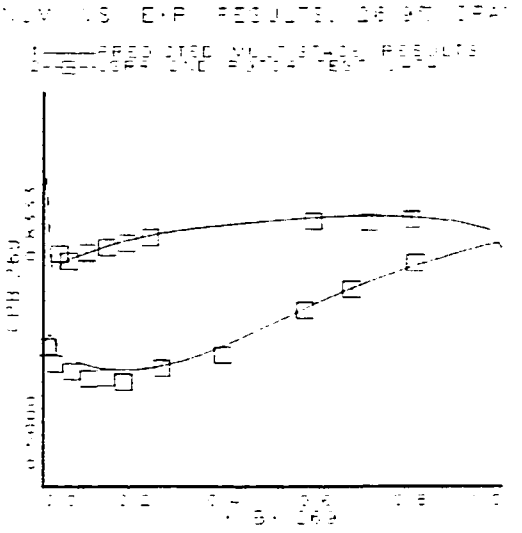

Figure 5.2c Rotor Cp at 26.9% span

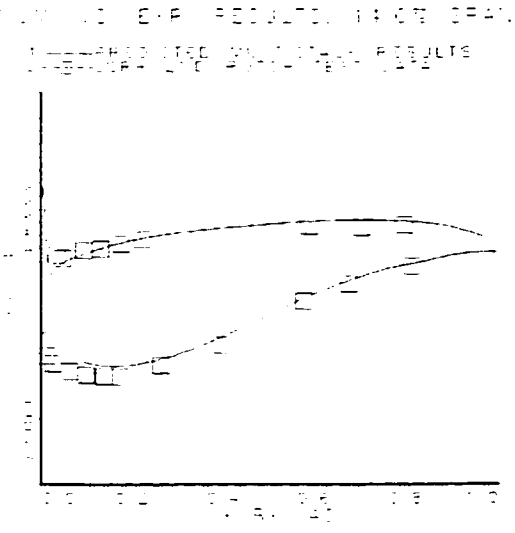

Figure 5.2b Rotor Cp at 14% span

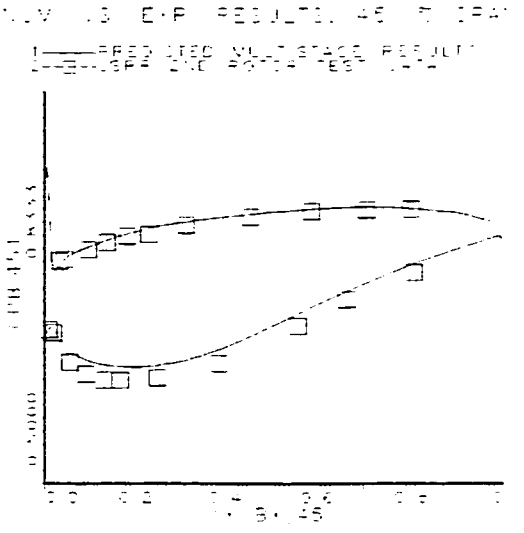

Figure 5.2d Rotor Cp at 45.1% span

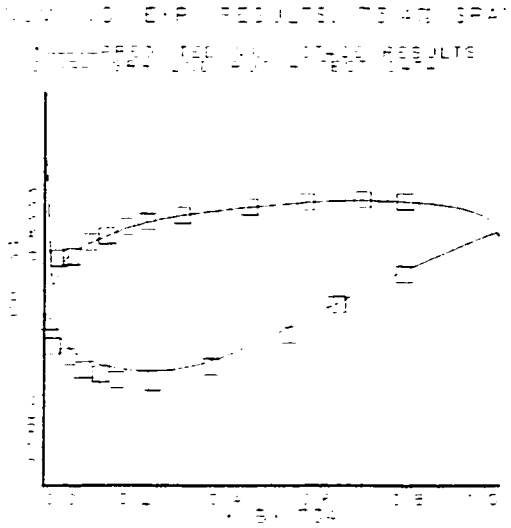

Figure 5.2e Rotor Cp at 73.4% span

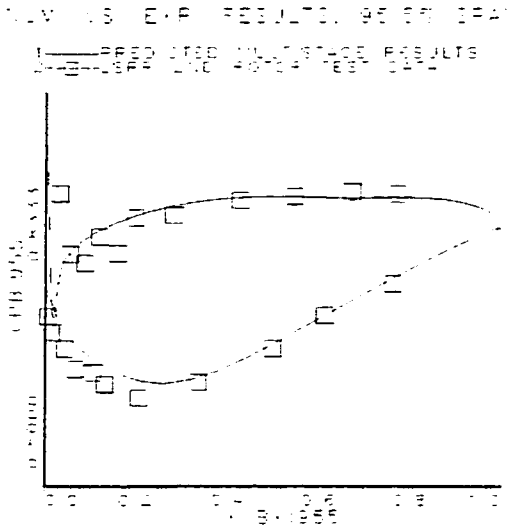

Figure 5.2g Rotor Cp at 95.5% span

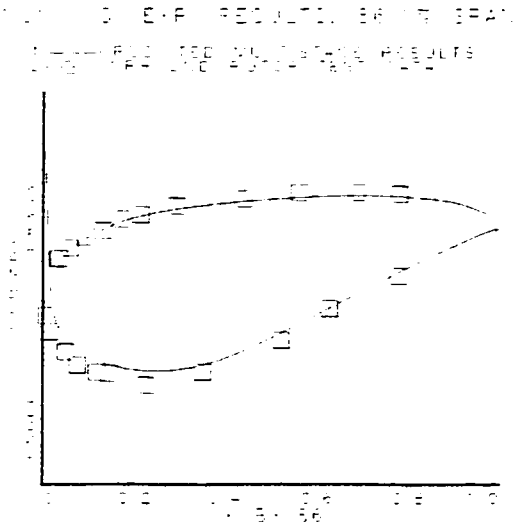

Figure 5.2f Rotor Cp at 86.1% span

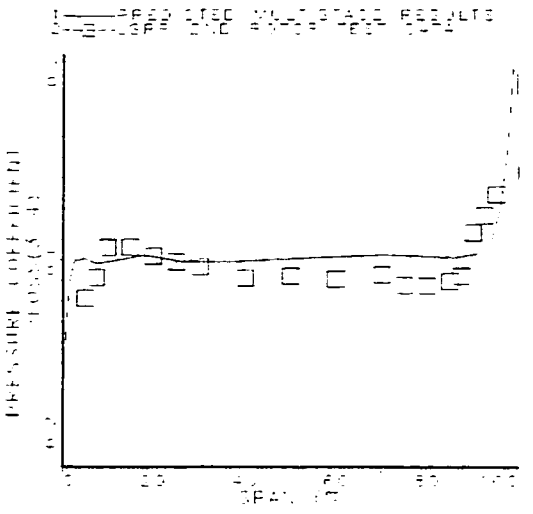

Figure 5.3 Rotor total pressure loss coefficient vs. % span

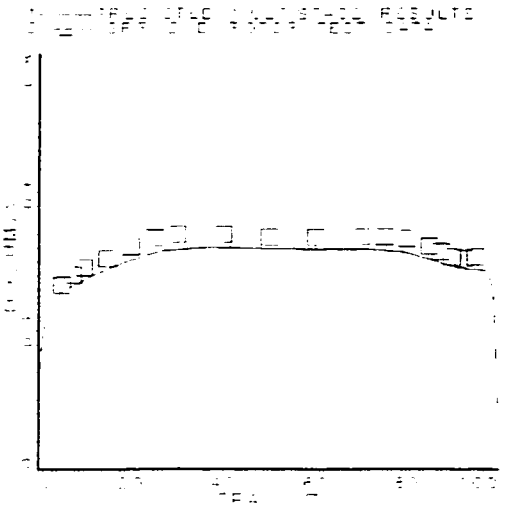

Figure 5.4a Normalized axial velocity vs. % span at rotor inlet

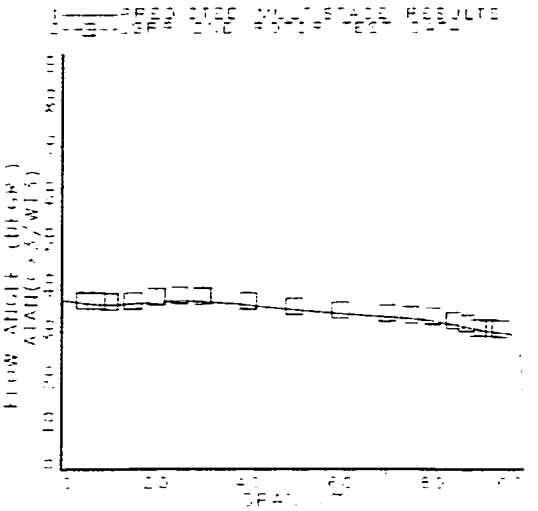

Figure 5.5a Relative flow angle vs. % span at rotor inlet

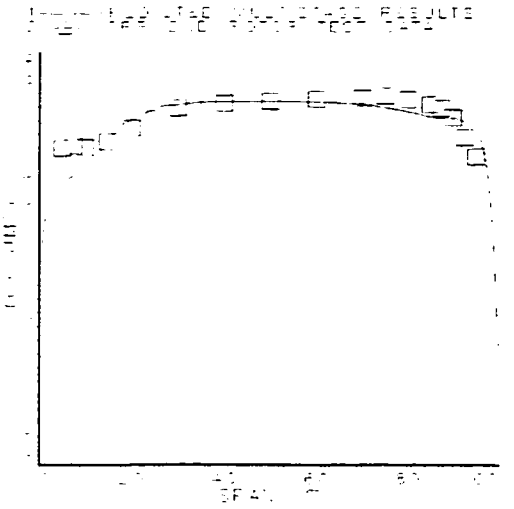

Figure 5.4b Normalized axial velocity vs. % span at rotor exit

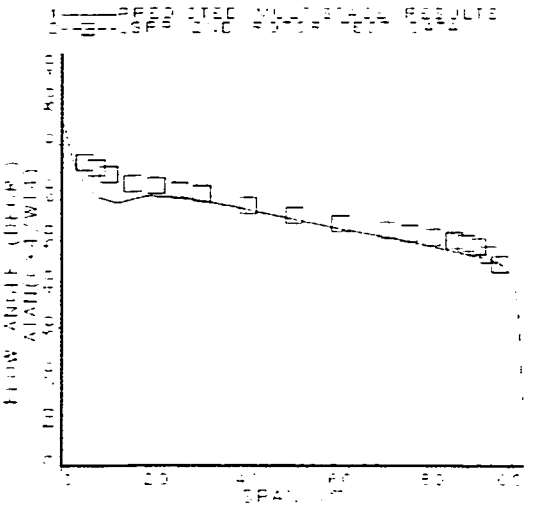

Figure 5.5b Relative flow angle vs. % span at rotor exit

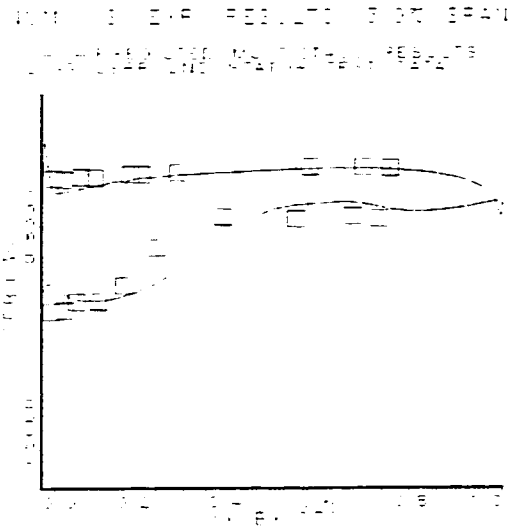

Figure 5.6a Stator Cp at 3% span

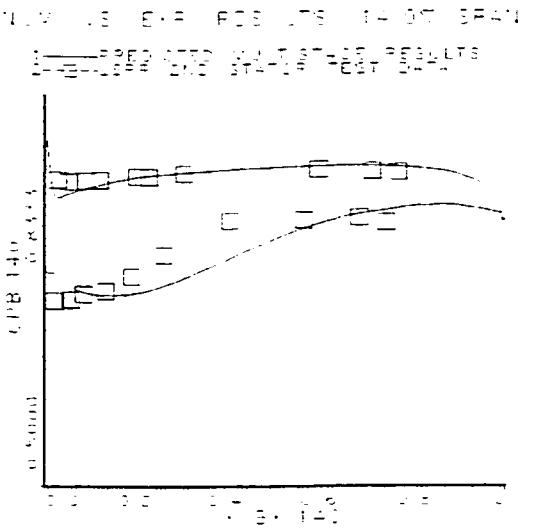

Figure 5.6c Stator Cp at 26.9% span

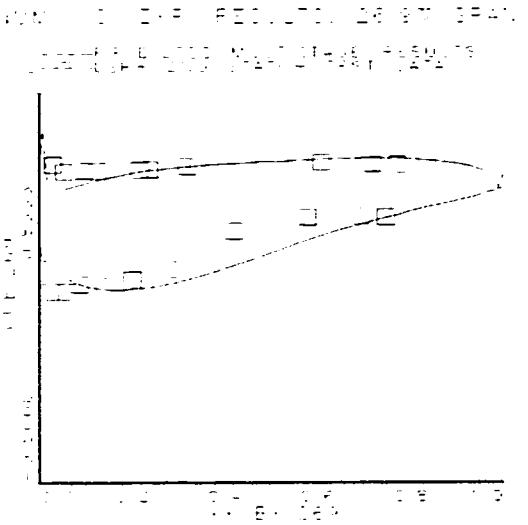

Figure 5.6b Stator Cp at 14% span

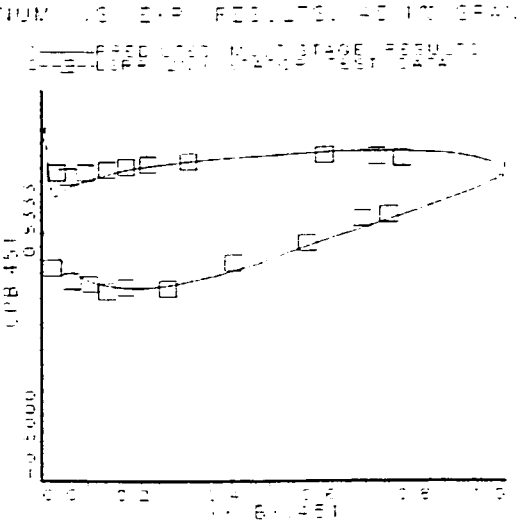

Figure 5.6d Stator Cp at 45.1% span

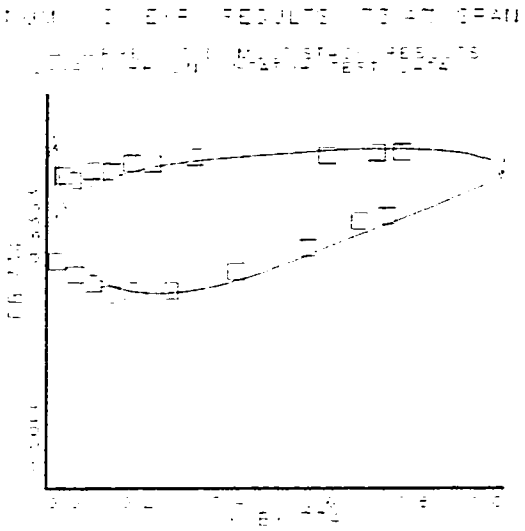

Figure 5.6e Stator Cp at 73.4% span

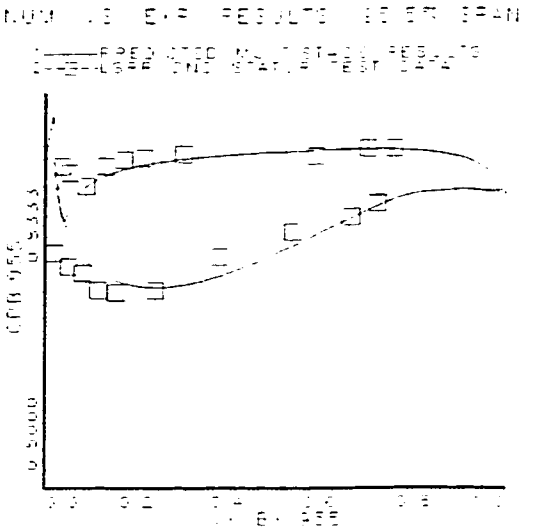

Figure 5.6g Stator Cp at 95.5% span

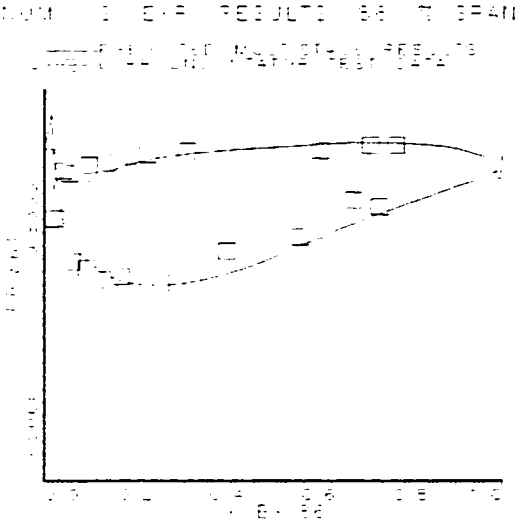

Figure 5.6f Stator Cp at 86.1% span

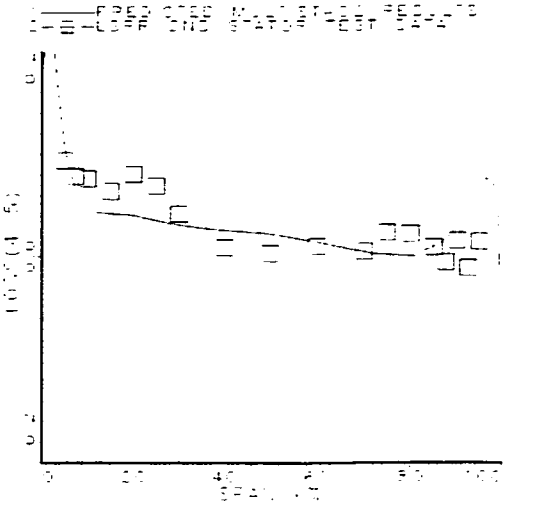

Figure 5.7 Stator total pressure loss coefficient vs. % span

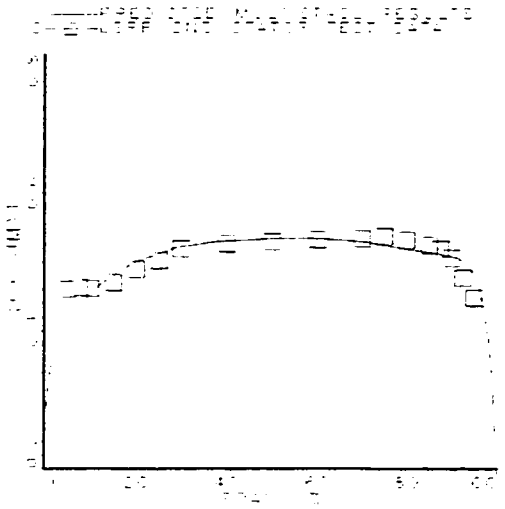

Figure 5.8a Normalized axial velocity vs. % span at stator inlet

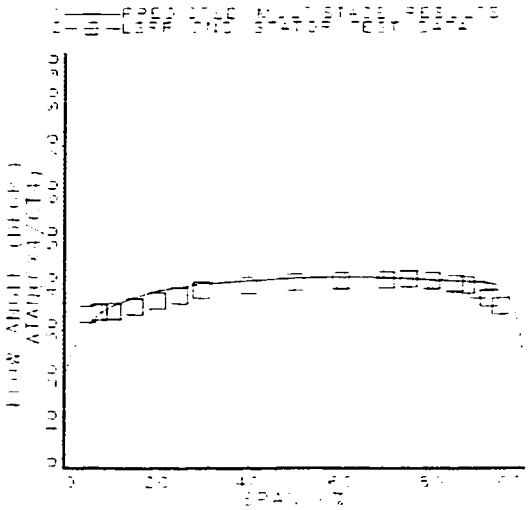

Figure 5.9a Absolute flow angle vs. % span at stator inlet

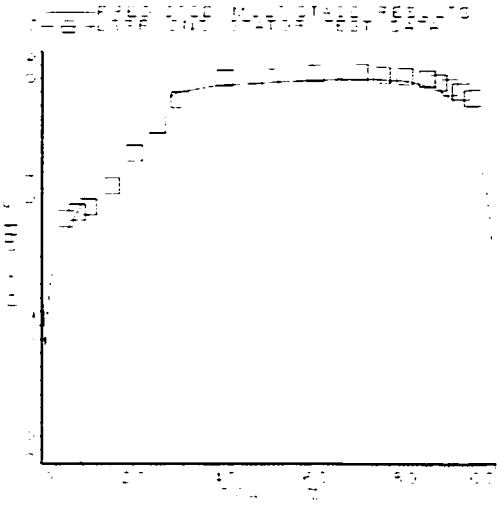

Figure 5.8b Normalized axial velocity vs. % span at stator exit

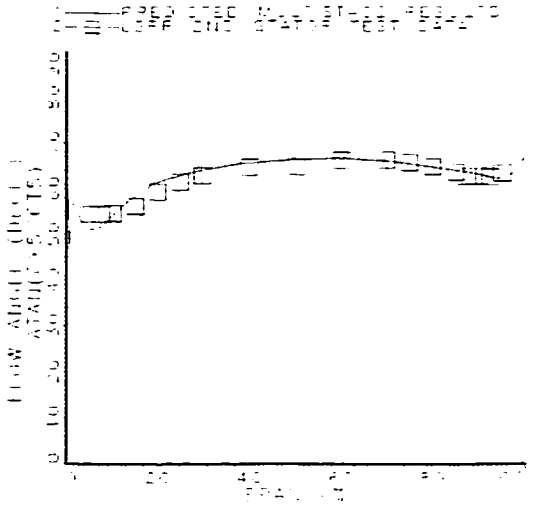

Figure 5.9b Absolute flow angle vs. % span at stator exit

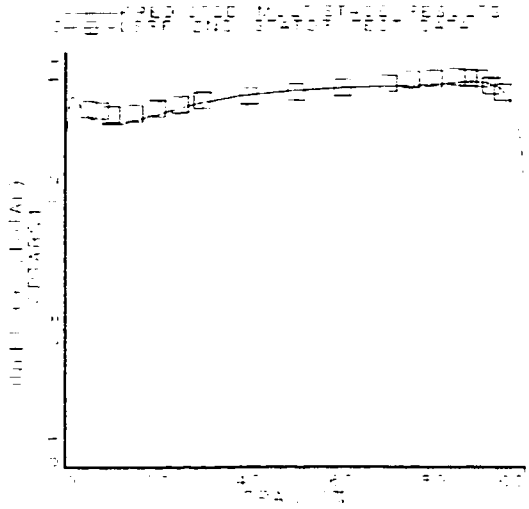

Figure 5.10a Total Cp vs. % span at stator inlet

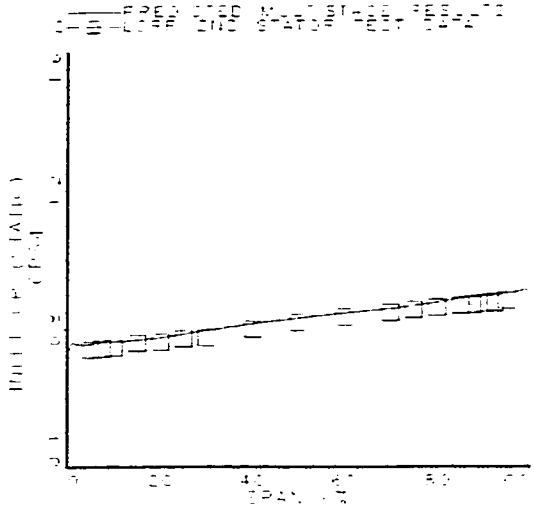

Figure 5.11a Cp vs. % span at stator inlet

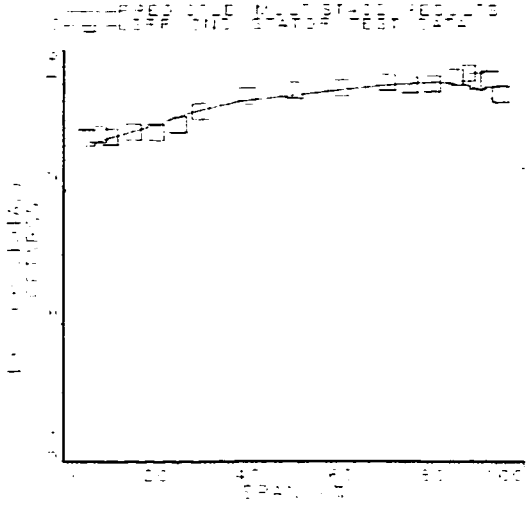

Figure 5.10b Total Cp vs. % span at stator exit

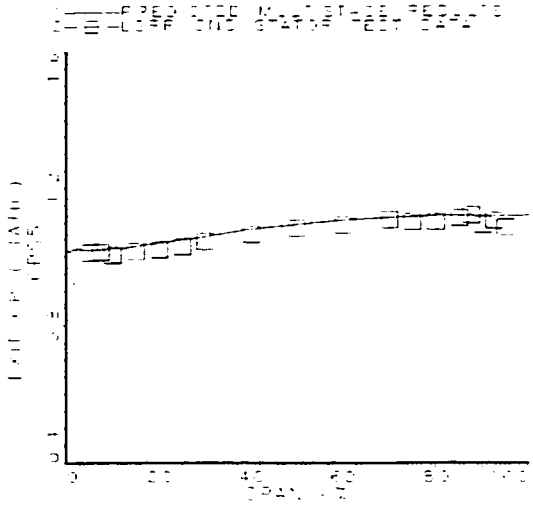

Figure 5.11b Cp vs. % span at stator exit

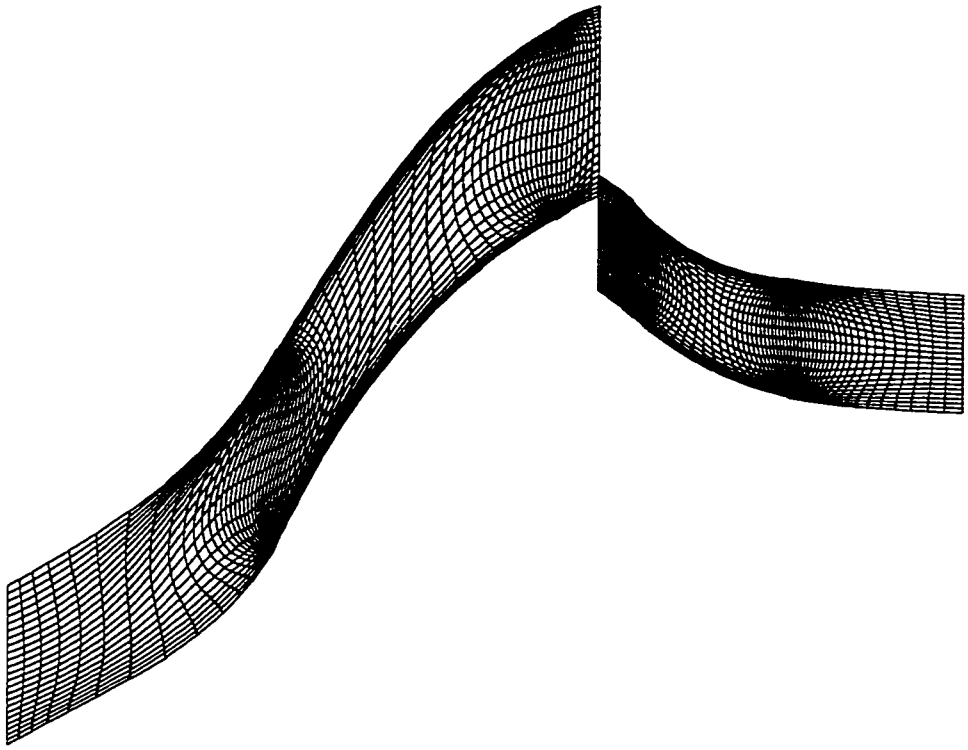

Figure 5.12 Finite element mesh at mid span of the first stage turboprop

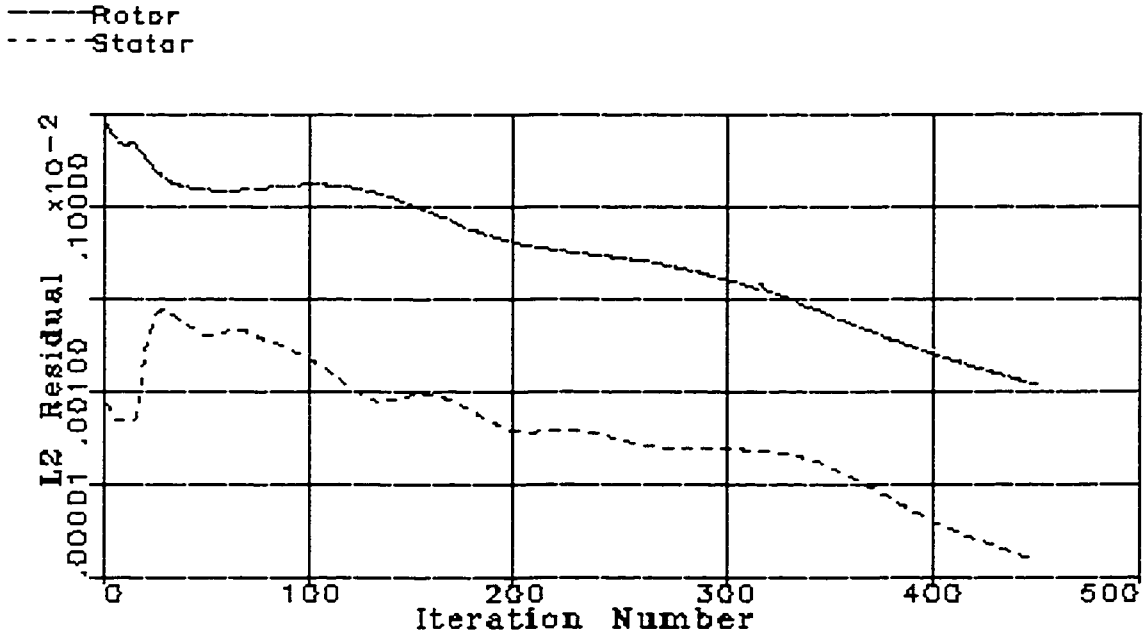

Figure 5.13 Convergence history of the Navier-Stokes equations for the first stage turboprop

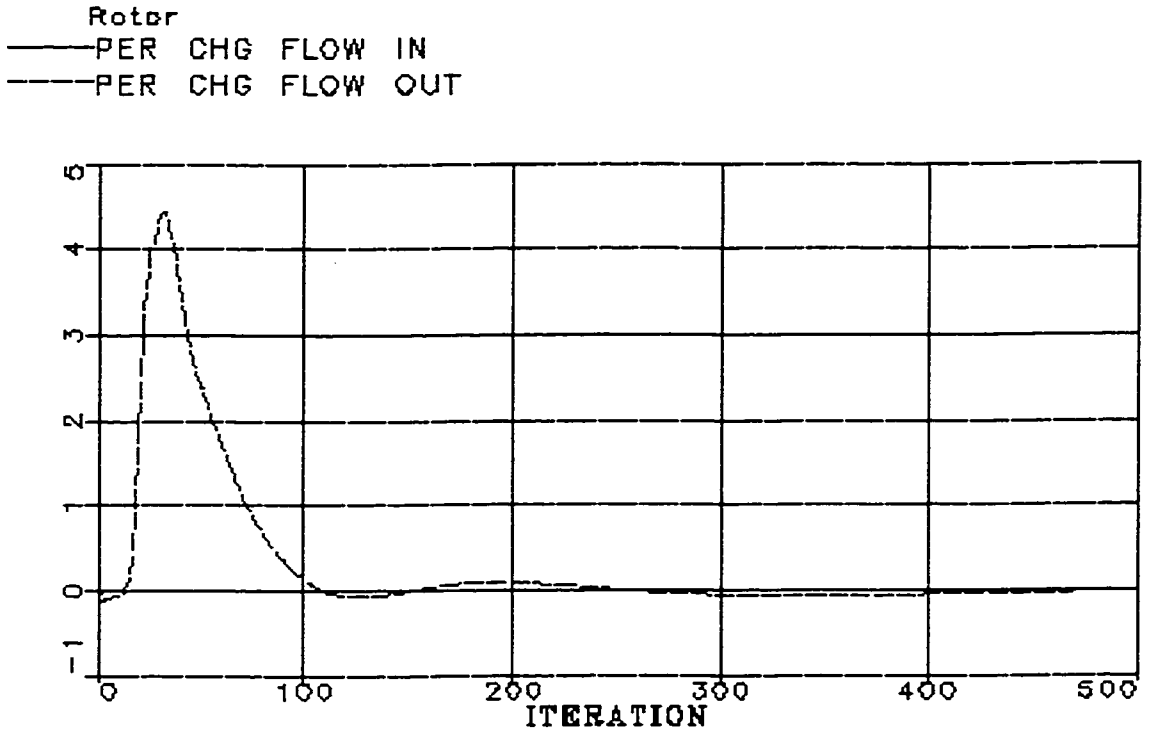

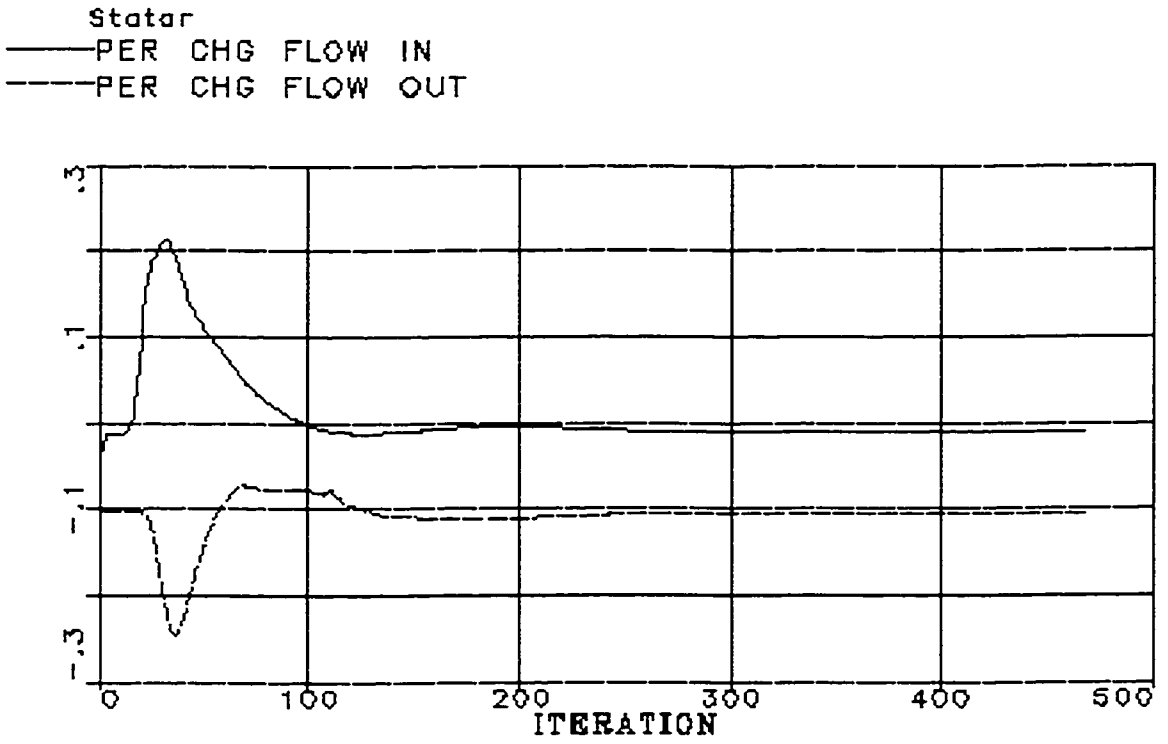

Figure 5.14 Percent change in component mass flow vs. iteration;

(a) rotor inlet and exit planes, (b) stator inlet and exit planes

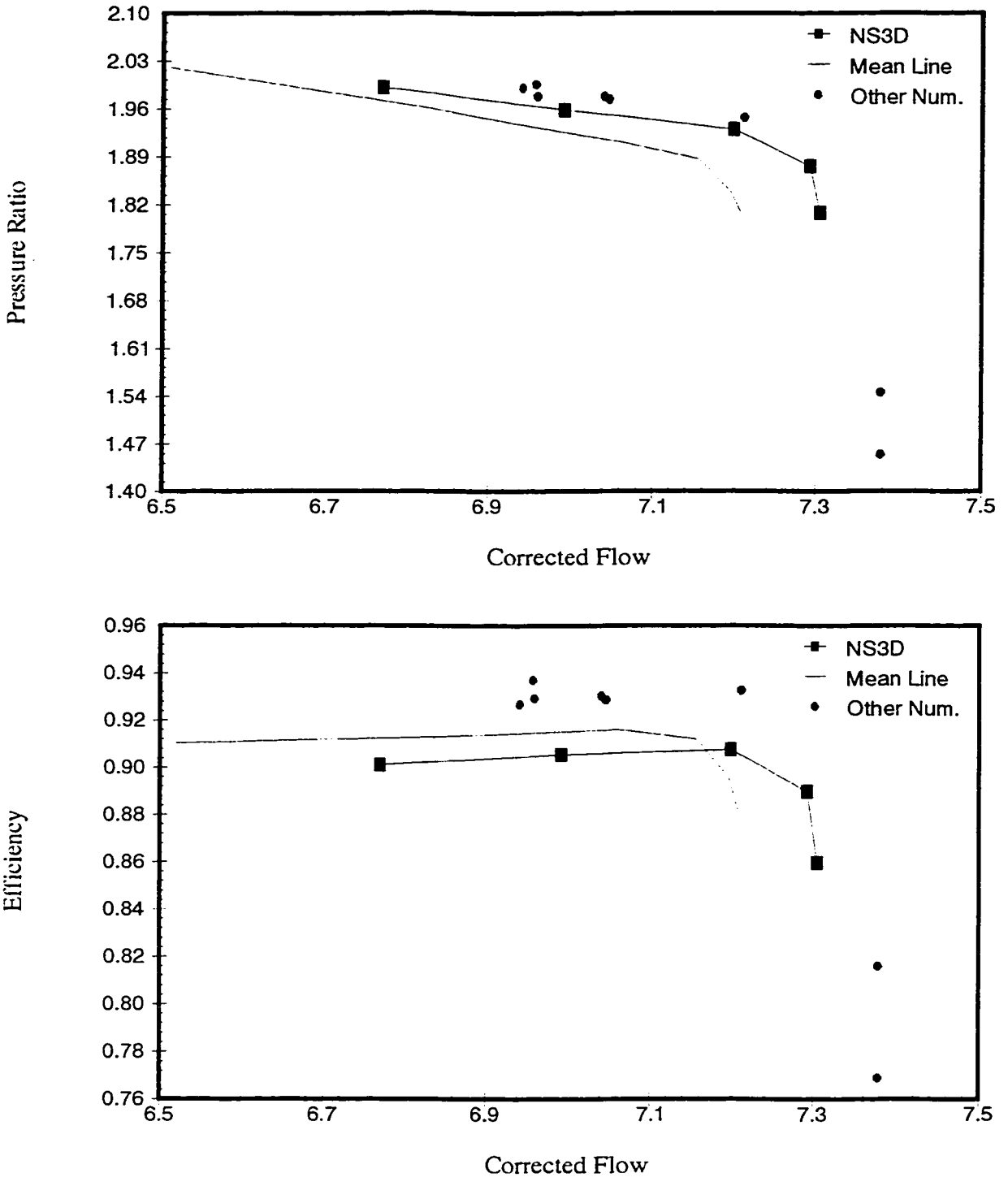

Figure 5.15 Comparison of 1st rotor speed line prediction by NS3D, mean line model, and other CFD code

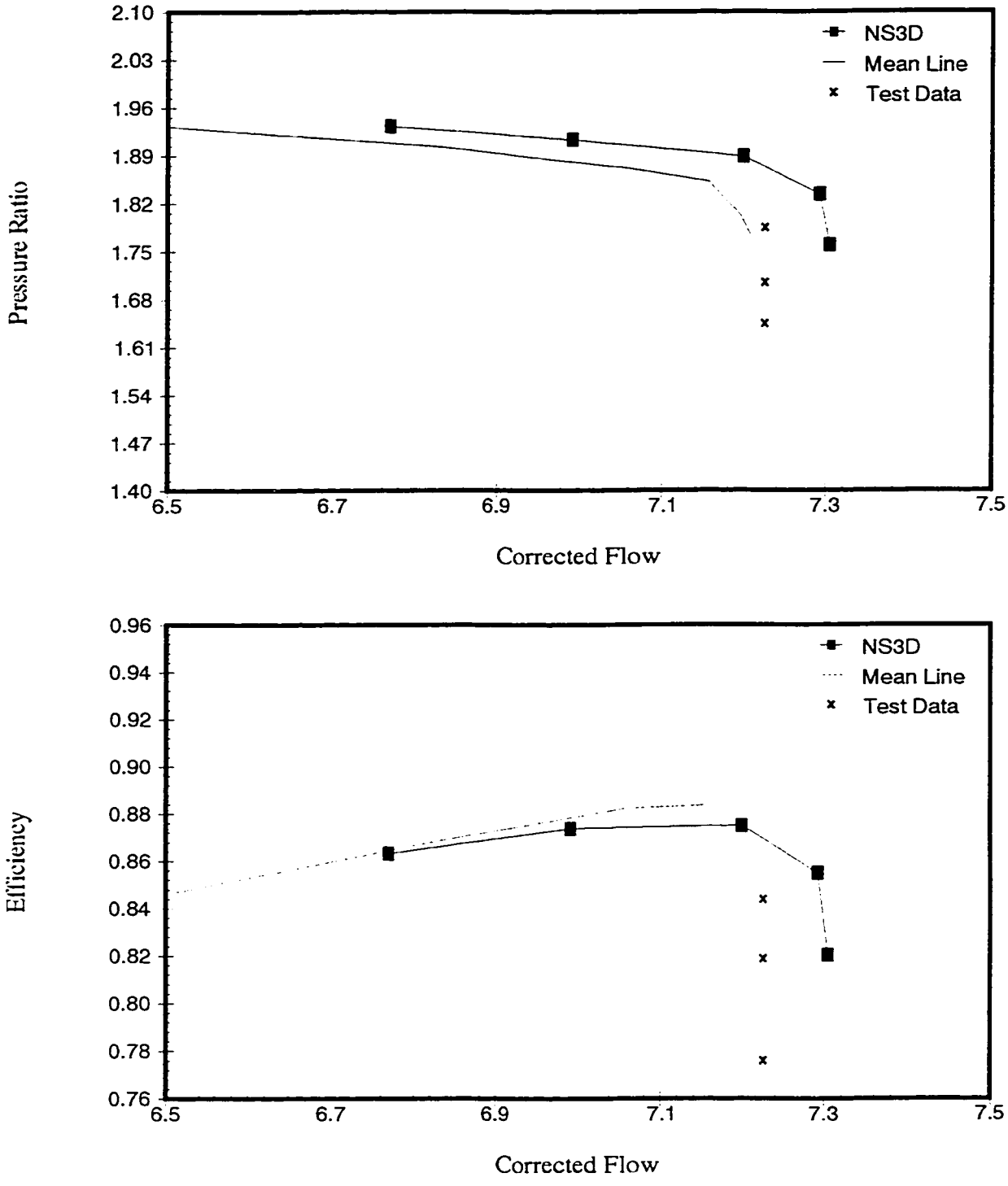

Figure 5.16 Comparison of stage turboprop speed line prediction by NS3D, mean line model, and test data

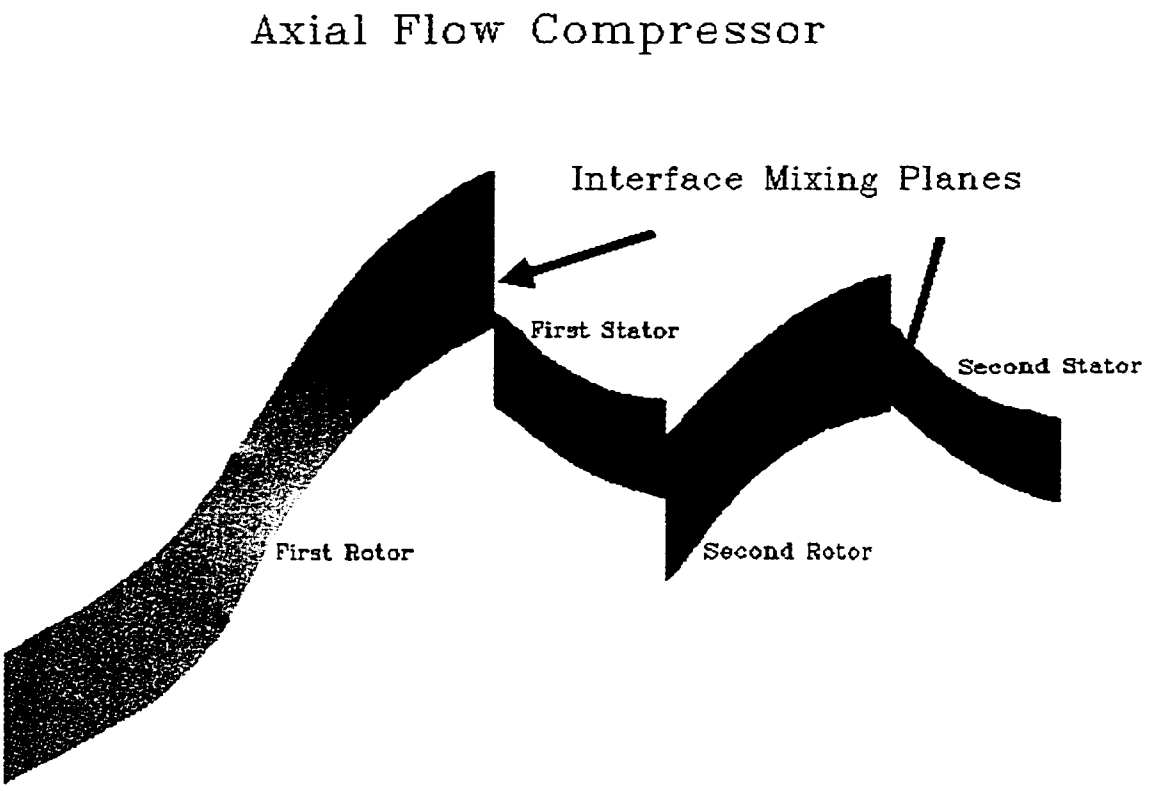

Figure 5.17 Turboprop engine: two-stage compressor at mid span plane

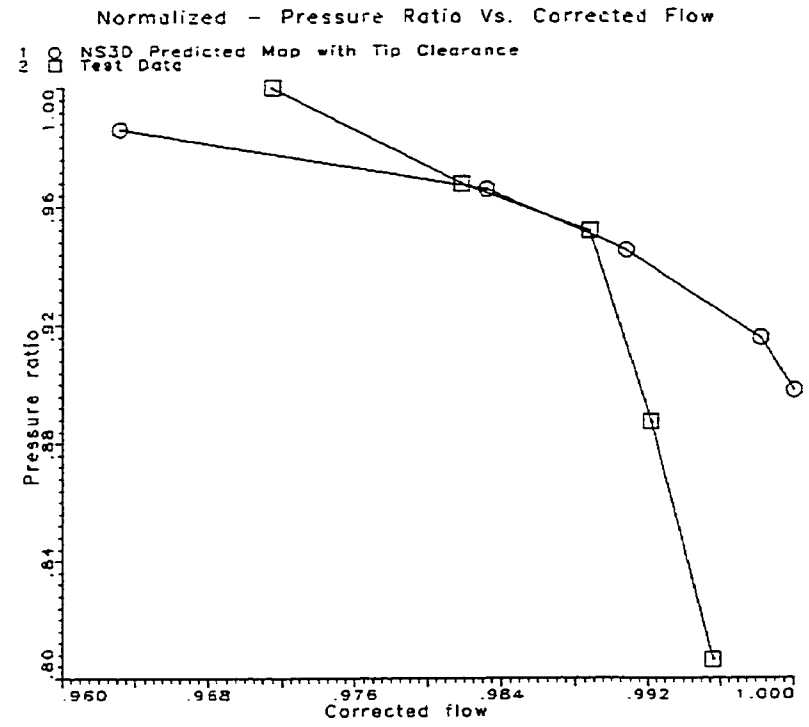

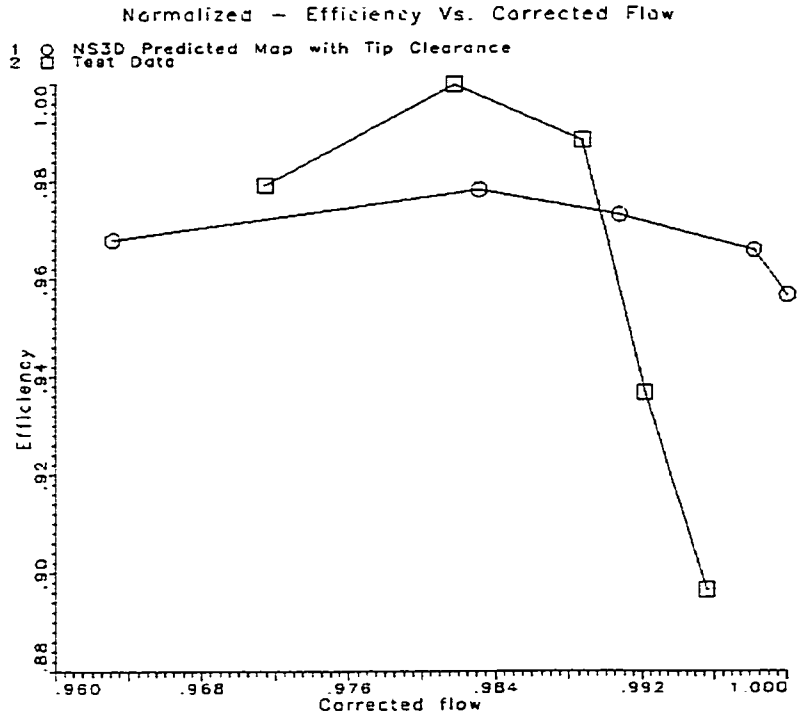

Figure 5.18 Comparison of two-stage speed line predictions by NS3D and test data; pressure ratio and efficiency vs. corrected flow

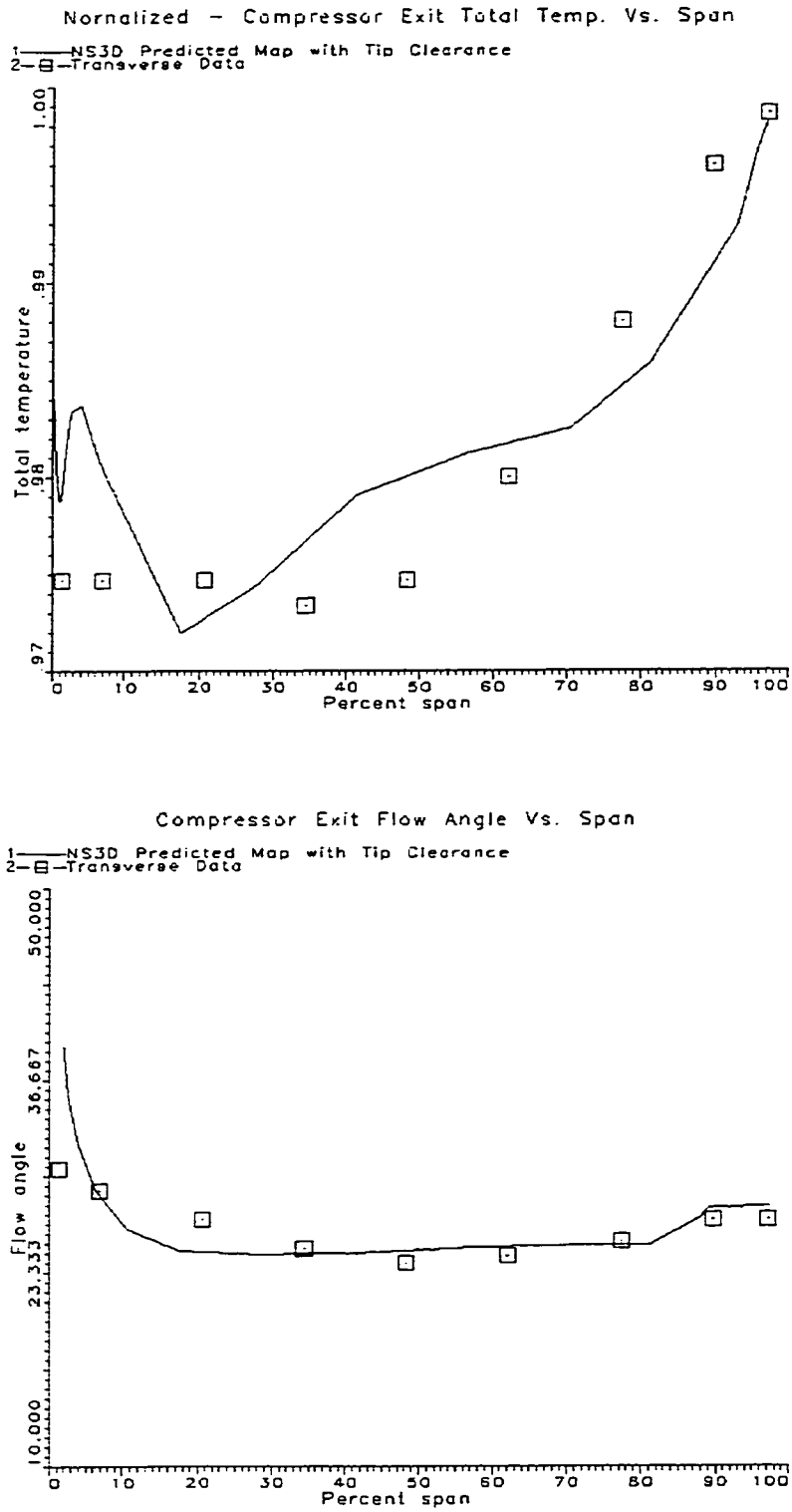

Figure 5.19 Comparison of radial distributions of absolute flow angle and absolute temperature at the compressor exit by NS3D and test data

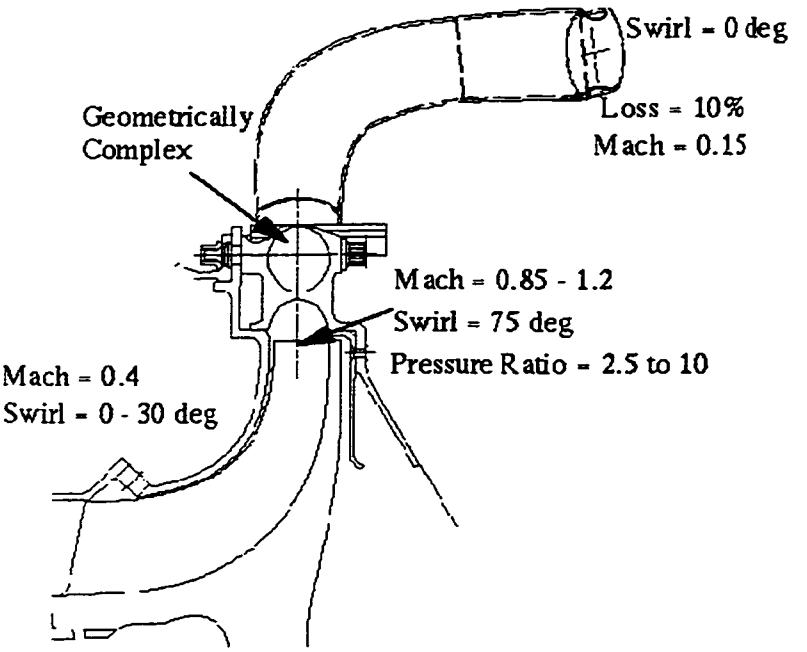

Figure 5.20 Centrifugal stage configuration; impeller-pipe diffuser

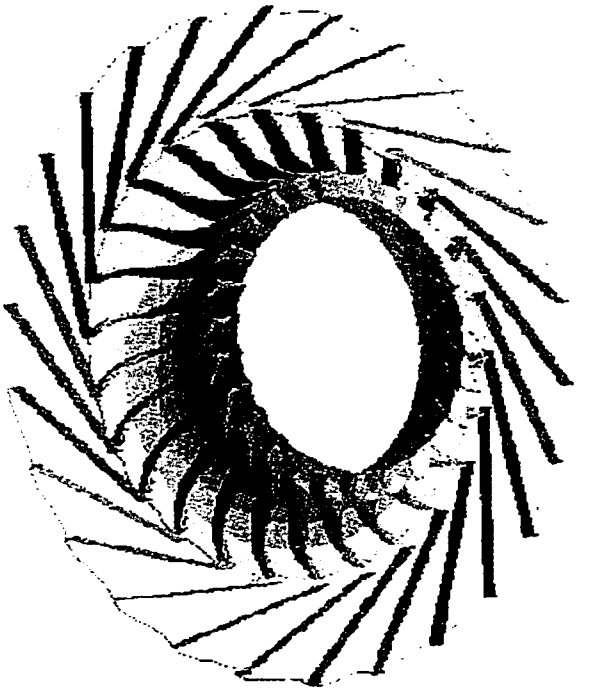

Figure 5.21 Centrifugal stage configuration; impeller-vane diffuser

Figure 5.22 Mixing plane Mach contours through a vane diffuser

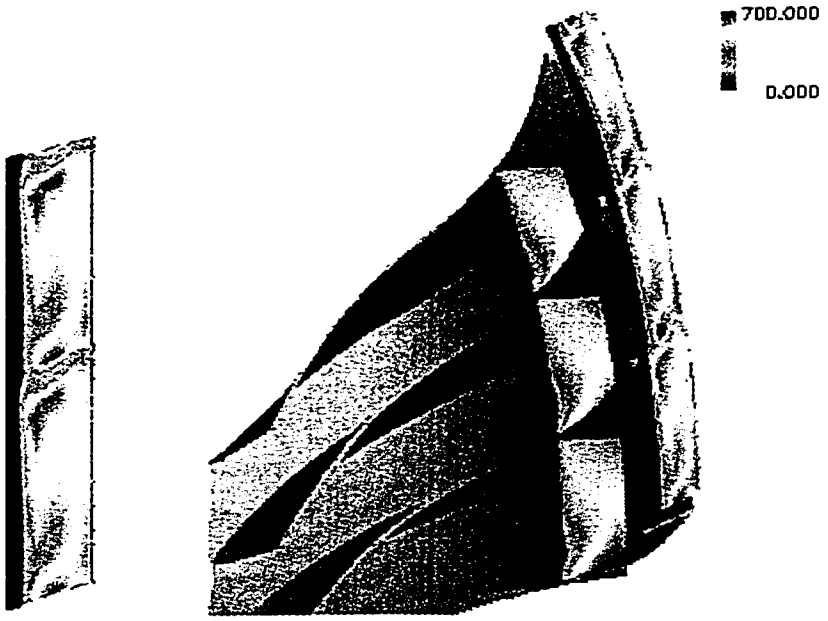

Figure 5.23 Mixing plane radial velocity contours at the impeller exit plane

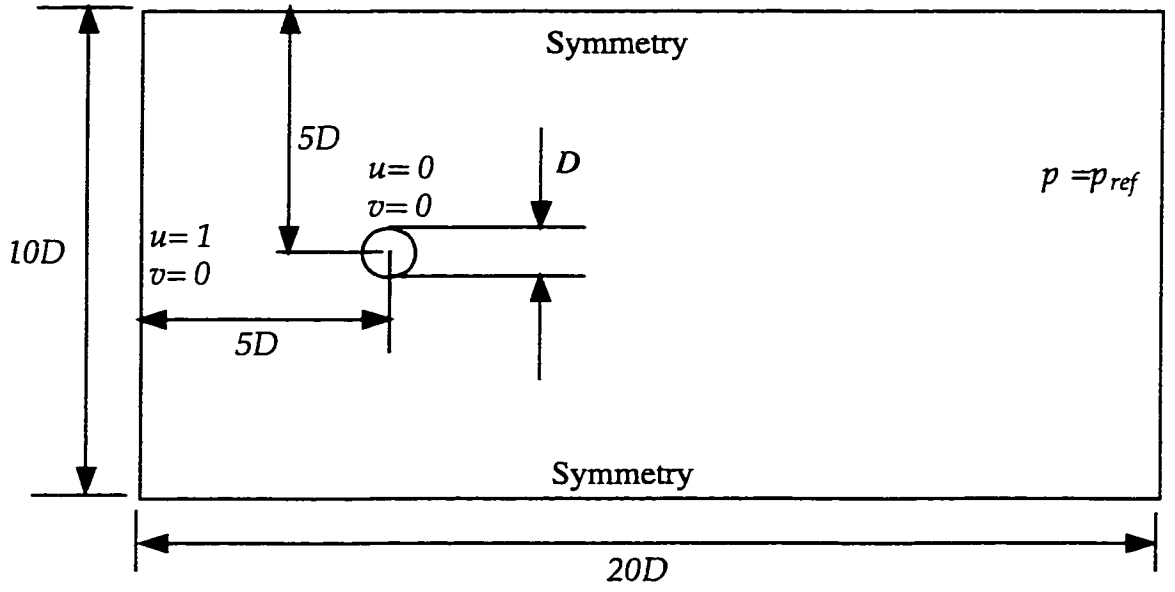

Figure 5.24 Computational domain and boundary conditions for the flow around a circular cylinder

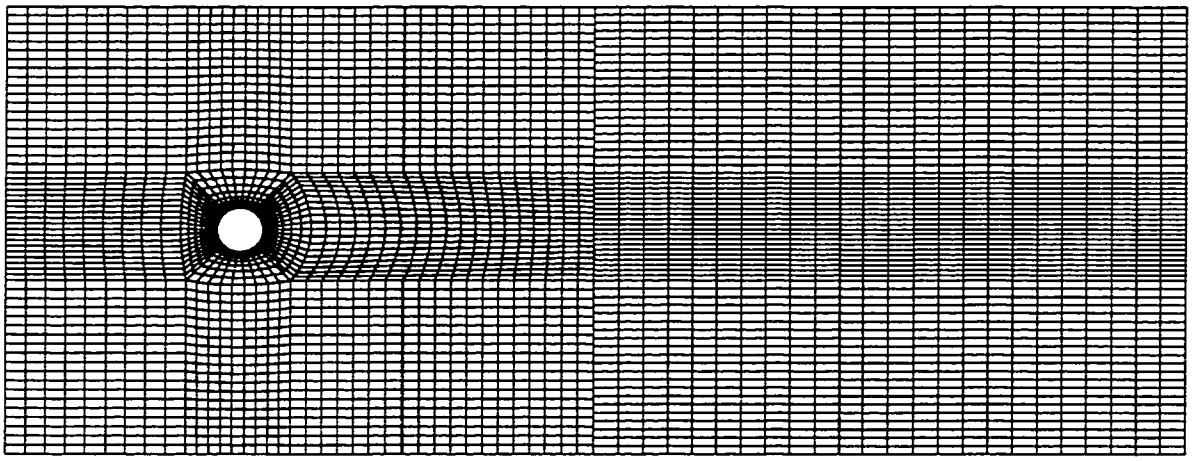

(a) Side view

(b) Top view

Figure 5.25 Finite element mesh for flow over a circular cylinder

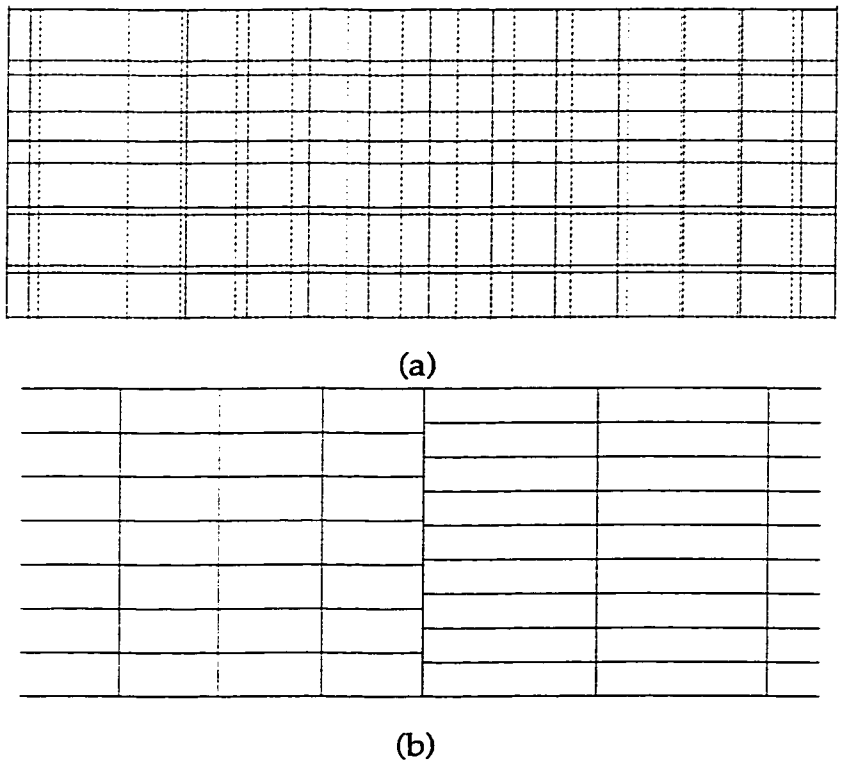

Figure 5.26 Details of mismatched grid; (a) front view; (b) side view

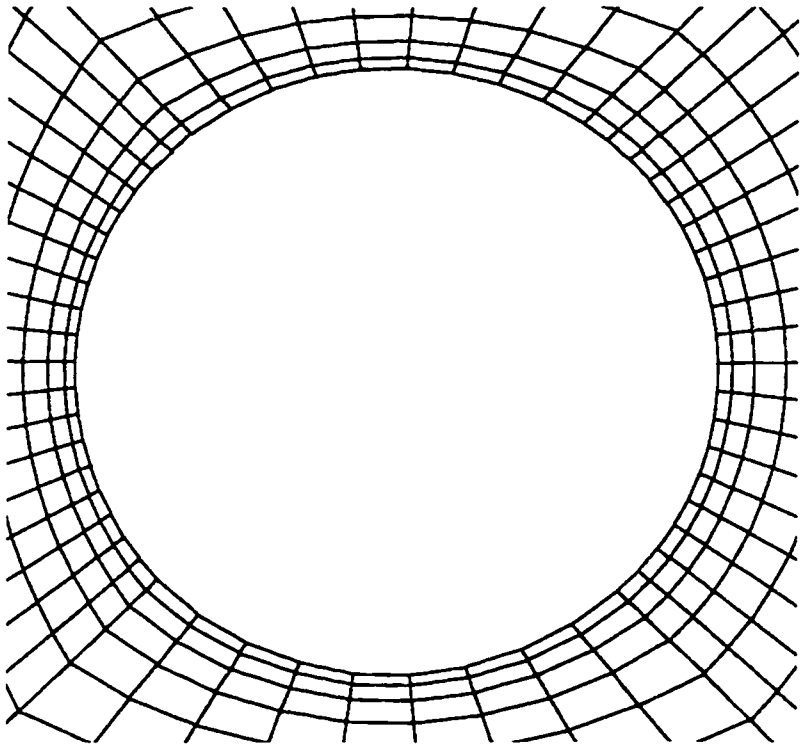

Figure 5.27 Mesh details near cylinder surface

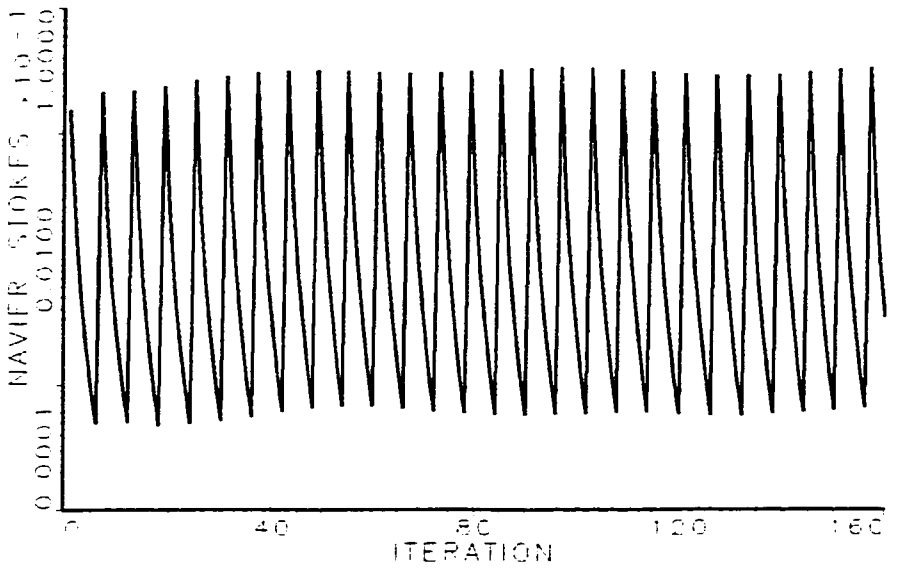

Figure 5.28 Convergence history of the unsteady Navier-Stokes equations for the laminar flow past a circular cylinder at Re=100

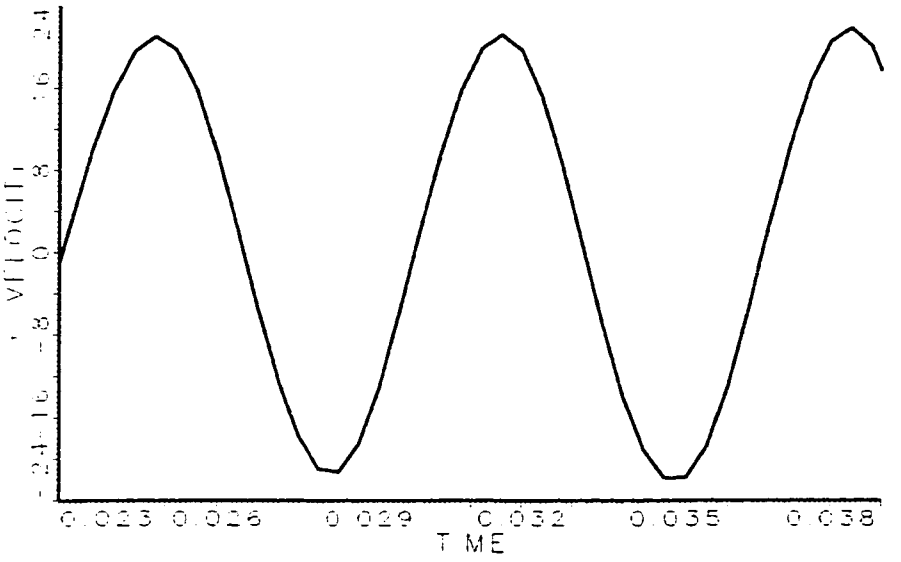

Figure 5.29 Predicted evolution of the y-component of velocity, v, with respect to time. Solution at a point (x/D=0.65, y=0) on the centerline behind the cylinder; Re=100, $\Delta t = 0.23$, T=5.75, Sr=0.174

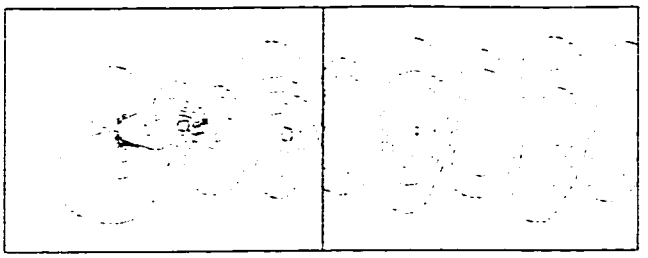

(a)

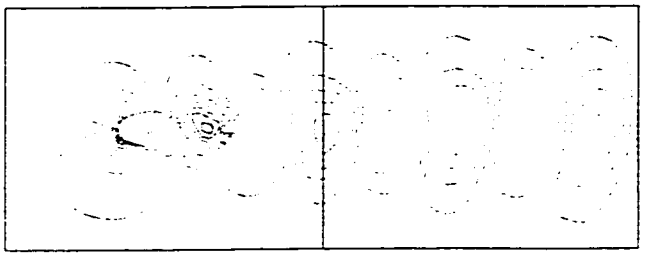

(b)

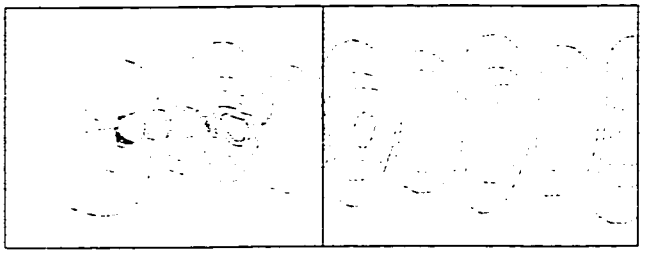

(c)

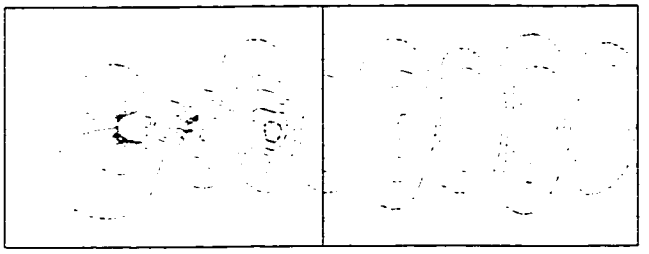

(d)

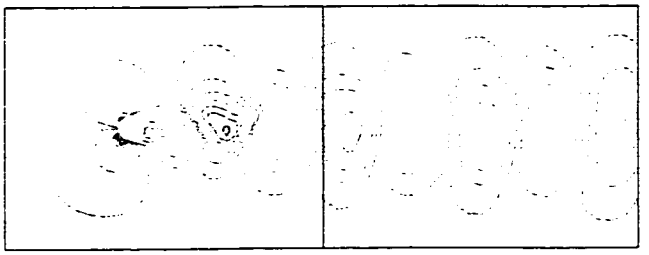

(e)

Figure 5.30 Predicted transverse velocity contours behind the cylinder over one cycle at times; (a) 0, (b) 0.23T, (c) 0.46T, (d) 0.69T, and (e) 0.92T. Laminar flow, Re=100, T=5.75, Sr=0.174

(a) Steady analysis (b) Unsteady analysis

Figure 5.31 Comparison of Mach contours through a centrigugal stage (a) steady analysis, (b) unsteady analysis

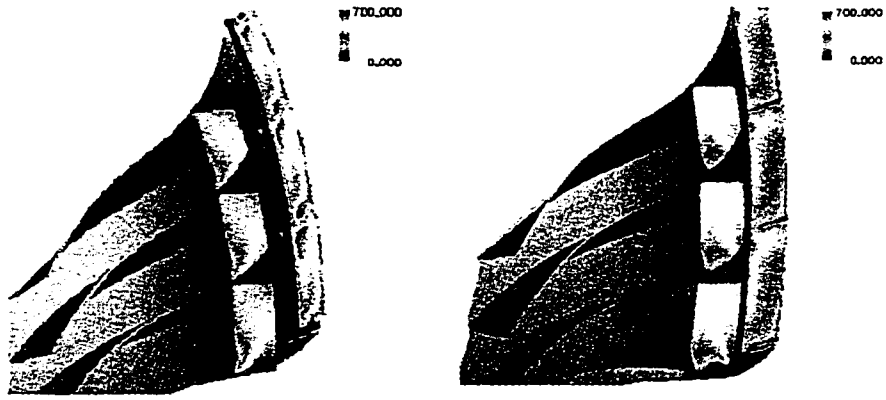

(a) Steady analysis (b) Unsteady analysis

Figure 5.32 Comparison of radial velocity contours through a centrigugal stage; (a) steady analysis, (b) unsteady analysis

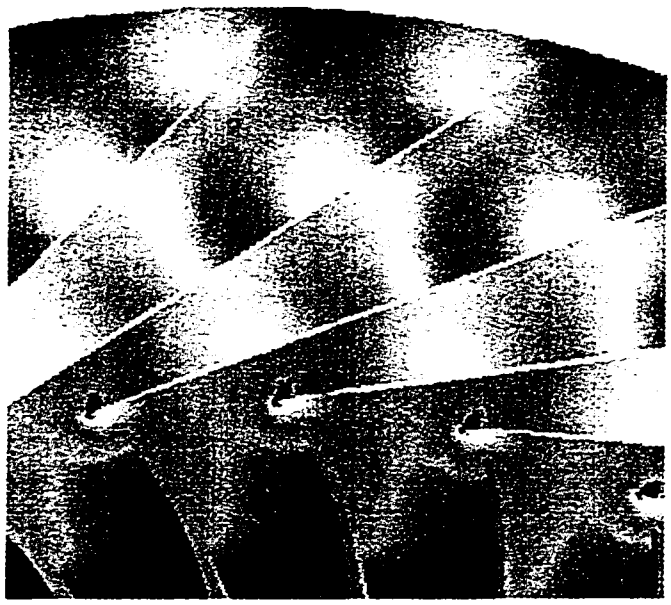

(a) static pressure contours

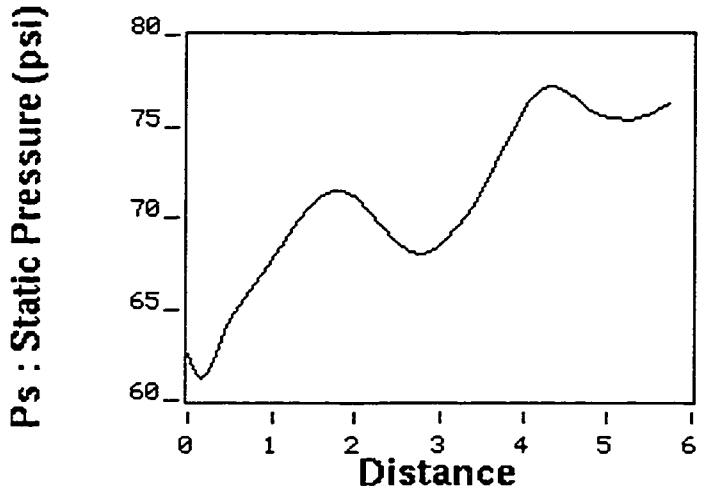

(b) static pressure midway through vane diffuser

Figure 5.33 Static pressure at an instant of time through a centrifugal compressor; (a) contour plot, (b) variation midway through vane diffuser

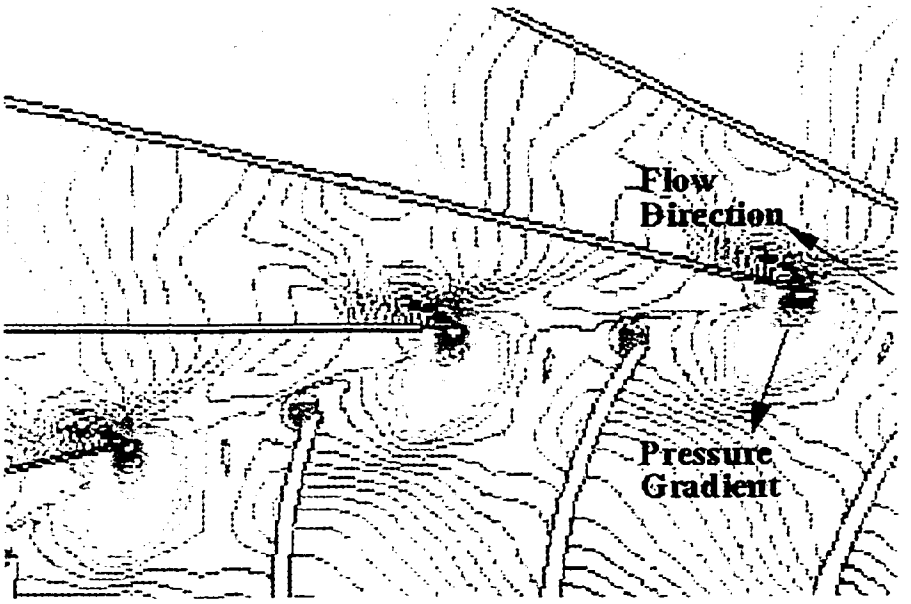

Figure 5.34 Instantanous static pressure gradient at the leading edge of the vane diffuser of the centrifugal stage

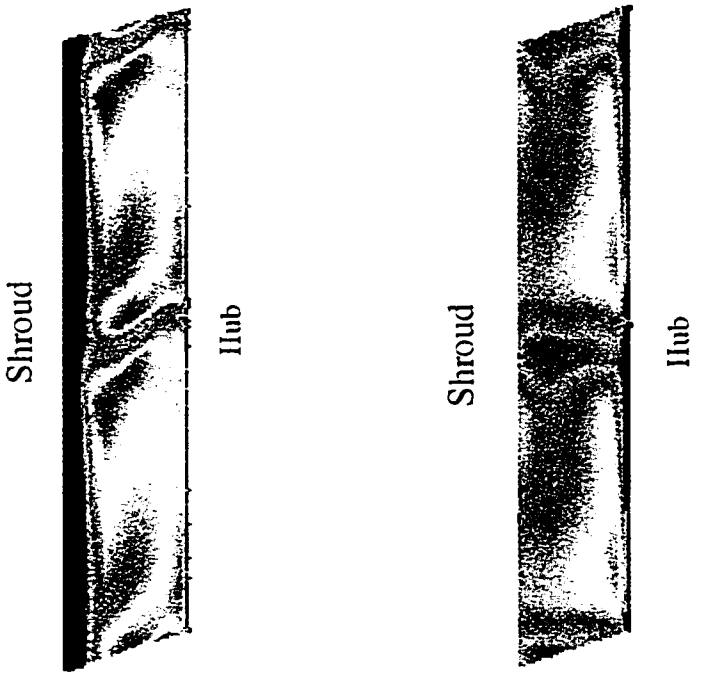

Figure 5.35 Radial velocity contours at the exit of plane of the impeller of the centrifugal stage

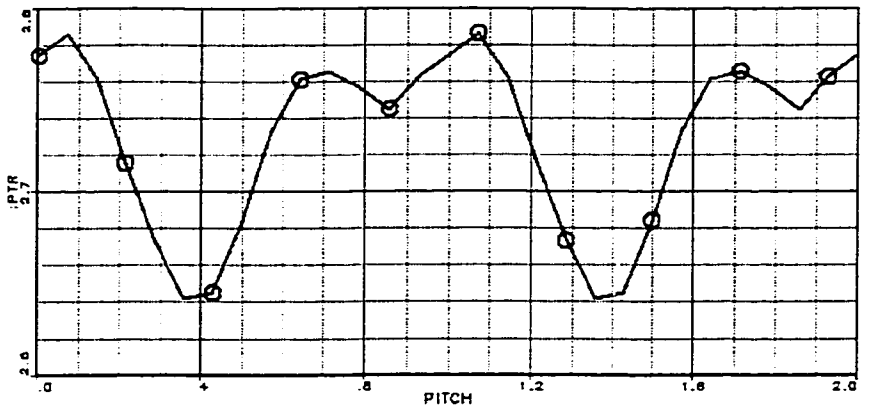

(a) Area Averaged Total Pressure

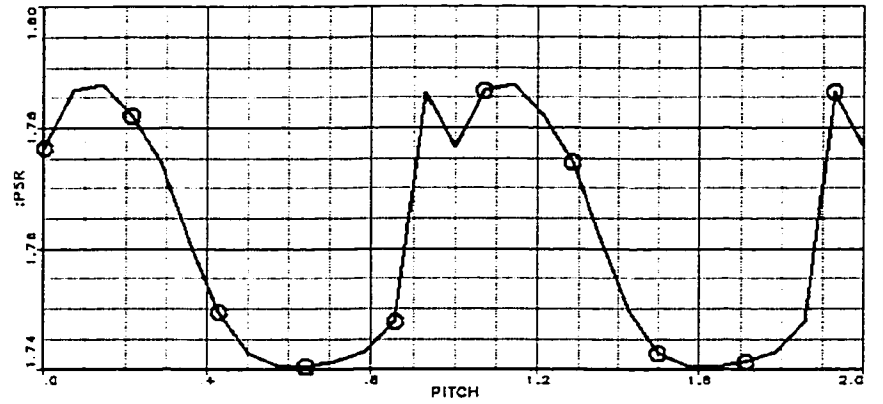

(b) Area Averaged Static Pressure

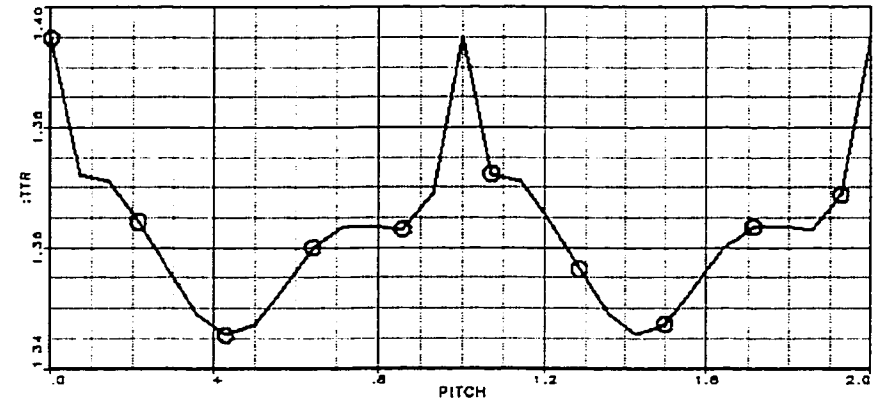

(c) Mass Averaged Total Temperature

Figure 5.36 Unsteady fluctuations of various flow quantities at the interface plane of the centrifugal stage

(a) t=0

(b) t=0.10T

(c) t=0.21T

(d) t=0.31T

(e) t=0.42T

Figure 5.37A Predicted velocity contours through a rotor blade of a PT stage over one blade-passing period T

(f) t=0.52T

(g) t=0.63T

(h) t=0.73T

(i) t=0.84T

(j) t=0.94T

Figure 5.37B Predicted velocity contours through a rotor blade of a PT stage over one blade-passing period T

6. Discussion

6.1 Conclusions

In this Thesis, a finite element formulation for the analysis of multistage turbomachinery is presented in terms of the Reynolds-averaged Navier-Stokes equations for three-dimensional unsteady, viscous, compressible, turbulent flow. Three methodologies are comprehensively described and their advantages and shortcomings are discussed.

A mixing plane finite element method applicable to multi-row turbomachinery has been implemented for the solution of three-dimensional viscous flows. A non-reflecting interface boundary condition is incorporated with the mixing plane methodology. It allows for a circumferential variation in static pressure at exit boundaries, while the radial profiles of static pressure, from the upstream exit and the downstream inlet at a mixing plane, are matched. This steady multistage methodology has been validated against three test cases, with hexahedral grids. The first test case involves the second stage of a low speed axial flow compressor with corner stall separation in the stator. The second test case considers a two-stage axial compressor of a turboprop engine, with transonic flow in the first rotor. Numerical results obtained for both cases compare well with the experimental data. The third test case deals with a compressor's centrifugal stage, comprising an impeller followed by a vane diffuser of equal pitch. It was found that the mixing plane predictions have flagrant inconsistency with engine performance data, indicating that the method is inappropriate for centrifugal machines. This finding is an important contribution of this Thesis.

The steady-state formulation of the system of Navier-Stokes equations in [46] has been extended to the time-accurate analysis of unsteady flows by implementing a second order Gear scheme. This formulation has been validated using the well-known two-dimensional test case of laminar flow past a circular cylinder. The vortex street shedding, observed experimentally, is captured and its computed shedding frequency is shown to be within 5% of the measured data.

The formulation is extended to handle the unsteady flow solution through a multistage turbomachine with equal pitches. Such flows are more complex since the rotor grid, at every time step, moves relative to the stator grid. A fully implicit finite element based methodology, using non-conforming grids at the interface, has been implemented to couple the rotor and stator solutions. One advantage of using non-conforming grids for the rotor and stator at the interface is that this method may be coupled to a grid adaptation capability. Such a capability would facilitate the grid generation process and open the doors for more complex geometries to be analyzed. The novelty of this implicit coupling procedure is that the assembly of element influence matrices of elements and the interpolation of solution are treated in a consistent manner at the interface plane. The implicit approach, characterized by its superior convergence rate, is a significant contribution of this Thesis. It permits the use of a high time-step and hence drastically reduces the computing time required to achieve a time periodic solution.

The unsteady approach for multistage turbomachines with equal pitches has been demonstrated on the same centrifugal stage compressor analyzed by the mixing plane method. In contrast with the steady mixing plane results, the unsteady numerical predictions agree well with experimental observations,

indication that the flow in centrifugal stages in fundamentally unsteady. This test case highlights the high stability limit of this method, as indicated by the high time step sizes allowed. As a comparison, typically 50 to 70 time-steps per blade-passing period are required with this method whereas 1000 to 3000 time-steps may be taken with explicit methods.

The equal pitch formulation is then enhanced, by transforming the governing flow equations from the physical time plane into a computational time plane, to handle the solution of a turbomachinery stage with different number of rotor and stator blade counts. The method is different from [6] in that it is implicit, formulated in terms of the solution vector U, not Q as in [6], and implemented in 3-D for viscous flows. The decision to solve for the solution vector U, as opposed to Q, is due to the resulting simplification of the interpolation procedure when transforming the solution from the stator frame to the rotor frame and vice-versa. The advantages of time-inclined approach are that only one channel per blade row is required and the implementation of the periodicity boundary condition at free boundaries is simplified.

The time inclination method is demonstrated on unsteady flow through a rotor blade passage of the power turbine of a turboprop engine. A stator wake is imposed at the inlet boundary of the rotor and unsteady computations are carried out in the time inclined plane of the rotor. The wake-to-rotor pitch ratio in this case is 1.2. The method is shown to be a powerful tool for single-stage analysis with unequal blade count.

An interpolation procedure has been developed and implemented to exchange the finite element solutions across interface planes common to rotors and stators.

The scheme has been proven to produce perfectly matching contour lines for all flow variables through the interface, even with the use of completely mismatched grids.

A post-processor based on Fourier transform theory has been developed to map the finite element solution from the time inclined computational plane into the physical time plane. The quality of the solution in the physical plane has been shown to be quite good, with no discontinuities in contour lines of all flow variables at free boundaries where the flow is periodic in the computational space.

The work of this Thesis has been embedded into a Concordia-Pratt & Whitney three-dimensional, turbulent, steady Navier-Stokes code, *NS3D*. It provides a powerful flow analysis tool which is essential in the design of modern turbomachinery blades.

6.2 Future Work

The applicability of the time-inclination formulation can be improved by considering cases with unequal airfoil counts for successive rotor or stator rows. As implemented in this Thesis, the time-inclination formulation is applicable to a multistage configuration with equal airfoil counts for successive rotor or stator rows, an example being a two-stage turbine with blade counts 75 and 76 for the first stage, and 75 and 76 for the second stage. However, it is not applicable for cases with unequal airfoil counts for successive rotor or stator rows, such as blade counts 66 and 72 for the second stage as in the previous example. This problem may be addressed by coupling the time-inclined solution of the first

stage to that of the second stage through a mixing plane placed downstream of the second blade row and upstream of the third blade row.

There is also a need to make this multistage methodology a useful analysis and design tool for low pressure (LP) turbines where the concepts of high-lift airfoils and clocking are of importance. Both design concepts and their relevance to unsteady flow phenomenon will be described briefly.

Cost and weight savings of LP turbines can be achieved by reducing the airfoil count and hence increasing the loading, thus the term high-lift airfoils. As the airfoil loading is increased, the diffusion level of the suction surface boundary layer also increases, making it more susceptible to separation. LP turbines operating at cruise conditions are particularly susceptible to boundary layer separation due to the low Reynolds numbers at which they operate. Under these conditions, a significant fraction of the suction surface boundary layer is laminar and transition to turbulence usually occurs via a laminar separation bubble. If this separated flow does not reattach before the trailing edge, the losses increase substantially [73,74].

One of the biggest shortcomings of today's CFD tools for the simulation of LP turbines is the lack of an accurate transition/turbulence modeling. The problem of predicting periodic transition in an unsteady flow environment is very challenging and a mathematical model for separated flow transition needs to be developed [75].

The study of high-lift airfoils and clocking can be thought of as a related subject since the clocking effect may possibly allow increased airfoil loads due to its

effect on the boundary layer transition process. Successive rotor or stator rows with equal airfoil counts can be circumferentially indexed relative to one another in order to minimize losses. This arises from the fact that the wakes from the upstream row of the clocked pair are "chopped", convected through the intermediate row and impinge on the downstream row in the same pitchwise position relative to each airfoil. A sinusoidal pattern in loss level then results based on whether the wake impinges on the leading edge, exactly between airfoils, or at some intermediate point. The loss mechanisms are not clearly understood; possibly they depend on unsteady boundary layer transition, as is the case for high-lift airfoils [76]. With the implementation of the unsteady multistage capability in NS3D, it is now possible to address these problems occurring in LP turbines.

Although potential performance benefits can result from airfoil clocking, the effects of clocking on blade vibratory stresses and noise generation are less understood. Any clocking investigation aimed at measuring performance should be accompanied with blade stress as well as acoustics analysis. Future work may include coupling the unsteady multistage code with the aero-acoustic code developed by the CFD Lab of Concordia University. In such a case, the predicted unsteady pressure is fed into the aero-acoustic code for noise prediction. Another future project may involve coupling the multistage code with the aero-elastic code developed by the Concordia CFD Lab to predict flutter phenomena and blade failure.

References

1. Greitzer E. M., "An Introduction to Unsteady Flow in Turbomachines", *Thermodynamics and Fluid Mechanics of Turbomachinery*, Vol. 2, pp. 967-1024, 1985.

2. Hetherington R. & Moritz R.R., "Influence of Unsteady Flow Phenomena on the Design and Operation of Aero Engines", AGARD-CP- 177, 1977.

3. Dawes, W.N., "Toward Improved Throughflow Capability: The Use of Three-dimensional Viscous Flow Solvers in a Multistage Environment", *ASME Journal of Turbomachinery*, Vol. 114, pp. 8-17, 1992.

4. W. N. Dawes, "The Use of 3D Viscous Flow Solvers in a Multistage Environment", *Trans ASME Journal of Engineering for Power*, 90-GT-18, 1990.

5. R. H. Ni, J. Bogoian, "Prediction of 3D Multi-Stage Turbine Flow Field Using a Multi-Grid Euler Solver", *AIAA Paper*, 8900091, 1989.

6. M. B. Giles, "UNSFLO: A Numerical Method for the Calculation of Unsteady Flow in Turbomachinery", *GTL Report No. 205*, MIT Gas Turbine Laboratory, 1991.

7. Sleiman, M., Tam, A., Robichaud, M. P., Peeters, M. F., Habashi, W. G., and Fortin, M., "Turbomachinery Multistage Simulation by a Finite Element Adaptive Approach", *Paper No. 96-GT-418, 41st ASME Gas Turbine and Aeroengine Congress*, Birmingham, U.K., June 1996.

8. Adamczyk, J., "Model Equation for Simulating Flows in Multistage Turbomachinery", *ASME Paper 85-GT-226*, March 1985.

9. Adamczyk, J.J., Celestina, M.L., Beach, T.A. and Barnett, M., "Simulation of Three-dimensional Viscous Flow Within a Multistage Turbomachine", *ASME Journal of Turbomachinery*, Vol. 112, No. 3, pp. 370-376, 1990.

10. M.B. Giles, "Stator-Rotor Interaction in a Transonic Turbine", *AIAA Paper*, October 1990.

11. Gundy-Burlet K.L., Rai M.M., Stauter R.C. & Dring R.P. , "Temporally and Spatially Resolved Flow in a Two-Stage Axial Compressor: Part 2 - Computational Assessment", *ASME Journal of Turbomachinery*, Vol. 113, pp. 227-232, 1991.

12. Sturmayr A., "Part 1: Multiblock with Non-Matching Boundaries", *Vrije Universiteit Brussel - Stromingsmechanica and FFA Internal Report R/WP3/SN2*, January 1995.

13. Stumayr A., "Part 2: Non-Matching Multiblock with Patched Grids in Three Dimensions", *Vrije Universiteit Brussel - Stromingsmechanica internal report*, 1995.

14. Rai M.M., "Navier-Stokes Simulations of Rotor/Stator Interaction Using Patched and Overlaid Grids", *Journal of Propulsion*, Vol. 3., No. 5, pp. 387-396, 1987.

15. Rai M.M., "Three-Dimensional Navier-Stokes Simulations of Turbine Rotor-Stator Interaction; Part I Methodology and Part II Results", *Journal of Propulsion*, Vol. 5, No. 3, pp. 305-319, 1989.

16. Rai M.M. & Madavan N.K., "Multi-Airfoils Navier-Stokes Simulations of Turbine Rotor-Stator Interaction", *ASME Journal of Turbomachinery*, Vol. 112, pp. 377-384., 1990.

17. Sharma O.P., Pickett G.F. and Ni R.H., "Assessment of Unsteady Flows in Turbines", *ASME Journal of turbomachinery*, Vol. 1 I4, pp. 79-90, 1992.

18. Dawes W.N., "A Simulation of the Unsteady Interaction of a Centrifugal Impeller With Its Vaned Diffuser: Flow Analysis", *ASME Journal of Turbomachinery*, Vol. 117, 1995.

19. Kelecy EJ., Griffin J.W. and Delaney R.A., "The Effect of Vane-Blade Spacing on Transonic Turbine Stage Performance", *AGARD Report CP-510*, 1996.

20. Micklow G.J., Sauve H.S. and Shivaraman K., "Numerical Simulations of Advanced Transonic Compressor Stages Using an Unsteady Quasi-Three-Dimensional Flow Solver", *ASME Paper 95-GT-440*, 1995.

21. McConnaughey H.V. and Griffin L.W., "Numerical Prediction of Axial Turbine Stage Aerodynamics", *AGARD Report CP-468*, 1989.

22. Rangwalla A.A., Madavan N.K. and Johnson P.D., "Application of an Unsteady Navier-Stokes Solver to Transonic Turbine Design", *Journal of Propulsion and Power*, Vol. 8, No. 5, pp. 1079-1086, 1992.

23. Fourmaux A., Billonnet G. Le Meur A. and Lesain A., "Simulation numdrique des dcoulements tridimensionnels et instationnaires dans les turbomachines", *AGARD Report CP-468*, 1989.

24. Lemeur A., "Calculs 3D stationnaire et instationnaire dans un dtage de turbine transsonique", *AGARD Report CP-510*, 1992.

25. Paulon J., Zhang Z., Jia P. & Meng J., "Influence of Unsteady Effects on the measurements in a Transonic Axial Compressor", *ASME Journal of Turbomachinery*, Vol. 114, pp. 510-516, 1992.

26. Billonet G., Fourmaux A., Huard J. and Occhionigro A., "Utilisation de calculs 2,5 D et 3D d'dcoulements instationnaires pour le choix de l'instrumentation d'un banc d'essai de turbine", *AGARD Report CP-510*, 1996.

27. Erdos J.I., Alzner E. and McNally W., "Numerical Solution of Periodic Transonic Flow Through a Fan Stage", *AIAA Journal*, Vol. 15, No. 11, pp. 1559-1568, 1977.

28. Koya M. and Kotake S., "Numericai Analysis of Fully Three-Dimensional Periodic Flows Through a Turbine Stage", *ASME Journal of Engineering for Gas Turbines and Power*, Vol. 107, pp. 945-952, 1985.

29. Lewis J.P., Delaney R.A. and Hall E.J., "Numerical Prediction of Turbine Vane-Blade Interaction", *AIAA Paper 87-2149*, 1987.

30. He L., "An Euler Solution for Unsteady Flows Around Oscillating Blades", *ASME Journal of Turbomachinery*, Vol. 112, pp. 714-722, 1990.

31. He L., "Computational Study of Rotating-Stall Inception in Axial Compressors", *Journal of Propulsion & Power*, Vol. 13, No. 1, pp. 31-38, 1997.

32. He L. and Denton J.D., "Three-Dimensional Time-Marching Inviscid and Viscous Solutions for Unsteady Flows Around Blades", *ASME Journal of Turbomachinery*, Vol. 116, pp. 469-476, 1994.

33. Gerolymos G.A., Vinteler D., Haugeard R., Tsanga G. and Vallet I., "On the Computation of Unsteady Turbomachinery Flows Part 2 - Rotor/Stator Interaction using Euler Equations", *AGARD Report CP-571*, 1996.

34. Giles M.B., "Stator/Rotor Interaction in a Transonic Turbine", *Journal of Propulsion*, pp. 621-627, 1990.

35. Giles M.B. and Haimes R., "Validation of a Numerical Method for Unsteady Flow Calculations", *ASME Paper 9 I-GT-271*, 1991.

36. Jung A.R., Mayer J.F. and Stetter H., "Simulation of 3-D Unsteady Stator/Rotor Interaction in Turbomachinery Stages of Arbitrary Pitch Ratio", *ASME Paper 96-GT-69*, 1996.

37. Jung A.R., Mayer J. and Stetter J., "Calculation and Visualization of the Unsteady Flow in an Axial Turbine Stage", *3rd ECCOMAS Computational Fluid Dynamics Conference*, 1996.

38. Stetter H., Jung A.R. and MAyer J.F., "Numerical Studies of Unsteady Flow Phenomena in Multi-Blade Row Environment", *IMechE Seminar S461*, 1996.

39. Giles M.B., "Generalized conservation Cells for Finite Volume Calculations", *AIAA Paper 87-1118*, 1987.

40. Eulitz F., Engel K. and Pokorny S., "Numerical Investigation of Inviscid and Viscous Interaction in a Transonic Compressor", *AGARD Report CP-57*, 1996.

41. Hodson, H.P., "An Inviscid blade-to-blade Prediction of a Wake-Generated Unsteady Flow", *ASME Paper 84-GT-43*, June 1984.

42. Fourmaux, A., "Unsteady Flow Calculation in Cascades", *ASME Paper 86-GT-178*, 1986.

43. Lewis, J.P., Delaney R.A., and Hall E.J., "Numerical Prediction of Turbine Vane-Blade Interaction", *AIAA Paper 87-2149*, June 1987.

44. Jameson P.C.E., Chima, R.V., "An Explicit Range-Kutta Method for Unsteady Rotor/Stator Interaction", *AIAA Paper 88-0049*, 1988.

45. Chen, Y.S., "3-D Stator-Rotor Interaction of the SSME", *AIAA Paper 88-3095*, 1988.

46. M. F. Peeters, W. G. Habashi, B. Q. Nguyen and P. L. Kotiuga, "Finite Element Solutions of the Navier-Stokes Equations for Compressible Internal Flows", *AIAA Journal of Propulsion and Power*, Vol. 8, No. 1, pp. 192-198, January 1992.

47. NS3D: "Navier-Stokes in 3D Users' Guide, Version 4.2", *Pratt and Whitney Canada*, Sept. 1994.

48. McBride, B. J., Gordon, S., and Reno, M. A., "Coefficients for Calculating Thermodynamic and Transport Properties of Individual Species", *NASA TM 4513*, Oct. 1993.

49. Baker, A. J., *Finite Element Computational Fluid Mechanics*, John Wiley and Sons, 1983.

50. Dhatt, G. and Touzot, G., *The Finite Element Method Displayed*, John Wiley and Sons, 1984.

51. Hughes, T. J. R., *The Finite Element Method: Linear Static and Dynamic Finite Elements*, Prentice-Hall, 1987.

52. Baruzzi, G. S., A Second Order Finite Element Method for the Soluton of the Transonic Euler and Navier-Stokes Equations, Ph.D. thesis, 1995.

53. Brooks, Alexander N. , Hughes, Thomas J. , Streamline Upwind/Petrov-Galerkin Formulations for Convection Dominated Flows with Particular Emphasis on the Incompressible Navier-Stokes Equations, Computer Methods in Applied Mechanics and Engineering, 32, pp. 199-259, 1982.

54. Hughes, Thomas J., "Recent Progress in the Development and Understanding of SUPG Methods with Special Reference to the Compressible Euler and Navier-Stokes Equations", *International Journal for Numerical Methods in Fluids*, Vol. 7, pp. 1261-1275, 1987.

55. Carette, J.C., Deconinck, H. Paillere, H., Roe, P.L., "Multidimensional Upwinding: Its Relation to Finite Elements", *International Journal for Numerical Methods in Fluids*, Vol. 20, pp. 935-955, 1995.

56. Boivin, Sylvain, *Simulation d'écoulements Compressibles à Nombre de Reynolds Élevé*, Ph. D. Thesis, Université Laval, June 1990.

57. Sleiman, M., *A Time-Accurate Finite Element Solution of the Navier-Stokes Equations*, M.A.Sc. Thesis, 1995.

58. H. Manouzi and M. Fortin, "A Treatment of Wall Boundaries For Turbulent Flows by the Use of a Transmission Finite Element Method", *International Journal for Numerical Methods in Engineering*, Vol. 31, pp. 113-126, 1991

59. V. Haroutunian and M. Engelman, "On Modeling Wall-Bound Turbulent Flows Using Specialized Near-Wall Finite Elements and the Standard *k-e* Turbulence Model", *Advances in Numerical Simulation of Turbulent Flows*, pp. 97-105, ASME Conference, 1991.

60. V. N. Nguyen, W. G. Habashi and M. V. Bhat, "Vector-Parallel Gauss Elimination Solver for Large-Scale Finite Element Computational Fluid Dynamics", *Proceedings of the Supercomputing Symposium 1990*, Montreal, pp. 363-369, June 1990.

61. W. G. Habashi, V. N. Nguyen and M. V. Bhat, "Efficient Direct Solvers for Large-Scale Computational Fluid Dynamics Problems", *Computer Methods in Applied Mechanics and Engineering*, Vol. 87, pp. 253-265, 1991.

62. W. G. Habashi, M. Fortin, J. W. H. Liu, M. P. Robichaud, J. S. Strigberger, V. N. Nguyen and W. S. Ghaly, "Large-Scale Computational Fluid Dynamics by the Finite Element Method", *AIAA Paper 91-0120, AIAA 29th Aerospace Sciences Conference*, Reno, January 1991.

63. L. C. Dutto, W. G. Habashi, M. Fortin and M. P. Robichaud, "Parallelizable Block Diagonal Preconditioners for the Compressible Navier-Stokes Equations", *9th International Conference on Finite Element Methods in Flow Problems*, Barcelona, Spain, July 1993.

64. Dring, R. P., VanSeters, R. J. and Zacaharias, R. M., "A Three-Dimensional Navier-Stokes Calculation Applied to an Axial Compressor for Rotor and Stator", 93-GT-113, ASME International Gas Turbine and Aeroengine Congress, May 1993.

65. Dring, R.P. and Joslyn, H.D., "Through-Flow Analysis of a Multistage Axial Compressor: Part I - Aerodynamic Input," and " Part II - Analytical - Experimental Comparisons," *ASME Journal of Turbomachinery*, Vol. 108, pp. 17-31, 1986.

66. Ni, R.H. and Bogoian, J., "Prediction of 3D Multi-Stage Turbine Flow Field Using a Multi-Grid Euler Solver", *AIAA Paper*, 8900091, 1989

67. M. Hammache and M. Gharib, "An experimental study of the parallel and oblique vortex shedding from circular cylinders", *Journal of Fluid Mechanics*, Vol. 232, p. 567, 1991.

68. Li, J., Chambarel, A., Donneaud, M., and Martin, R., "Numerical Study of Laminar Flow Past One and Two Circular Cylinders", *Computers & Fluids*, Vol. 19, pp. 155-170, 1991.

69. P. M. Gresho, S. T. Chan, R. L. Lee, C. D. Upson, " A Modified Finite Element Method for Solving the Time-Dependent, Incompressible Navier-Stokes Equations. Part 2: Applications", *International Journal for Numerical Methods in Fluids*, Vol. 4, 619-640, 1984.

70. Peeters, M., Sleiman, M., Preliminary Unsteady Stage Analyses Using NS3D, Internal Memo, October 28, 1997

71. Justen, F., Ziegler, K., Gallus, H., Experimental Investigation of Unsteady Flow Phenomena in a Centrifugal Compressor Vaned Diffuser of Variable Geometry, *ASME Paper 98-GT-368*

72. Li, Y. W., " JT15D-5 High Compressor Performance Test", *P&WC Engineering Report No. 1372*, April 23, 1985.

73. Hodson, H.P., Huntsman, I., & Steele, A.B., "An Investigation of Boundary Layer Development in a Multistage LP Turbine", *ASME J. of Turbo.*, Vol. 116, pp. 376-383, 1994.

74. Schulte, V., and Hodson, H.P., "Unsteady Wake-Induced Boundary Layer Transition in High Lift LP Turbines", *ASME J. of Turbo.*, Vol. 120, pp.28-35, 1998.

75. Hu, J., and Fransson, H., "Transition Predictions for Turbomachinery Flows Using Navier-Stokes Solver and Experimental Correlation", *AIAA paper 97-2230*, 1997.

76. Eulitz, F., Engel, K., & Gebing, H., "Numerical Investigation of the Clocking Effects in a Multistage Turbine", *ASME paper 96-GT-26*, 1996.

Appendix A

Weak Galerkin Formulation of the Navier-Stokes Equations

The weak Galerkin formulation of the system of equations consisting of the continuity (2.2) and the Navier-Stokes momentum equations (2.3) in cylindrical coordinates will be demonstrated. Each equation is multiplied by a weight function, W, which is identical to the shape function, and integrated over the volume:

$$\int_V W\left[\frac{\partial}{\partial t}(U)+\frac{1}{r}\frac{\partial}{\partial r}(rA)+\frac{1}{r}\frac{\partial}{\partial \theta}(B)+\frac{\partial}{\partial z}(C)+\frac{D}{r}\right]dV=0 \tag{A.1}$$

where

$$U=\begin{bmatrix}\rho\\ \rho u_r\\ \rho u_\theta\\ \rho u_z\end{bmatrix} \tag{A.2}$$

$$A=\begin{bmatrix}\rho u_r\\ \rho u_r^2+p-\sigma_{rr}\\ \rho u_\theta u_r-\sigma_{\theta r}\\ \rho u_z u_r-\sigma_{zr}\end{bmatrix} \tag{A.3}$$

$$B=\begin{bmatrix}\rho u_\theta\\ \rho u_r u_\theta-\sigma_{r\theta}\\ \rho u_\theta^2+p-\sigma_{\theta\theta}\\ \rho u_z u_\theta-\sigma_{z\theta}\end{bmatrix} \tag{A.4}$$

$$C=\begin{bmatrix} \rho u_z \\ \rho u_r u_z - \sigma_{rz} \\ \rho u_\theta u_z - \sigma_{\theta z} \\ \rho u_z^2 + p - \sigma_{zz} \end{bmatrix} \tag{A.5}$$

$$D=\begin{bmatrix} 0 \\ -\rho(u_\theta + \Omega r)^2 - p + \sigma_{\theta\theta} \\ \rho u_r (u_\theta + 2\Omega r) - \sigma_{r\theta} \\ 0 \end{bmatrix} \tag{A.6}$$

$$\sigma_{ij}=\frac{\mu}{Re}\begin{bmatrix} \left(2\frac{\partial u_r}{\partial r}+\Lambda\right) & \left(\frac{1}{r}\frac{\partial u_r}{\partial \theta}+\frac{\partial u_\theta}{\partial r}-\frac{u_\theta}{r}\right) & \left(\frac{\partial u_r}{\partial z}+\frac{\partial u_z}{\partial r}\right) \\ \vdots & 2\left(\frac{1}{r}\frac{\partial u_\theta}{\partial \theta}+\frac{u_r}{r}\right)+\Lambda & \left(\frac{1}{r}\frac{\partial u_z}{\partial \theta}+\frac{\partial u_\theta}{\partial z}\right) \\ \text{sym.} & \cdots & \left(2\frac{\partial u_z}{\partial z}+\Lambda\right) \end{bmatrix} \tag{A.7}$$

$$\Lambda=\frac{\lambda}{\mu}Re\left(\frac{1}{r}\frac{\partial}{\partial r}(ru_r)+\frac{1}{r}\frac{\partial u_\theta}{\partial \theta}+\frac{\partial u_z}{\partial z}\right) \tag{A.8}$$

Subsequent integration by parts yields the weak Galerkin form of the system of equations

$$\int_V\left[-W\frac{\partial U}{\partial t}+\frac{\partial W}{\partial r}A+\frac{1}{r}\frac{\partial W}{\partial \theta}B+\frac{\partial W}{\partial z}C+W\frac{D}{r}\right]dV=\int_S WEdS \tag{A.9}$$

where the surface integral term, E , is of the form:

$$E = \begin{bmatrix} \rho \bar{V} \bullet \vec{n} \\ (\rho u_r^2 + p - \sigma_{rr})\frac{rd\theta dz}{dS} + (\rho u_r u_\theta - \sigma_{r\theta})\frac{drdz}{dS} + (\rho u_r u_z - \sigma_{rz})\frac{rdrd\theta}{dS} \\ (\rho u_\theta u_r - \sigma_{\theta r})\frac{rd\theta dz}{dS} + (\rho u_\theta^2 + p - \sigma_{\theta\theta})\frac{drdz}{dS} + (\rho u_\theta u_z - \sigma_{\theta z})\frac{rdrd\theta}{dS} \\ (\rho u_z u_r - \sigma_{zr})\frac{rd\theta dz}{dS} + (\rho u_z u_\theta - \sigma_{z\theta})\frac{drdz}{dS} + (\rho u_z^2 + p - \sigma_{zz})\frac{rdrd\theta}{dS} \end{bmatrix} \quad \text{(A.10)}$$

Appendix B

Time Discretization and Newton Linearization of the Navier-Stokes Equations

B.1 Time Discretization

The weak Galerkin form of the Navier-Stokes system of equations (A.6-A.7) is discretized in time using the fully implicit Gear scheme, with variable order of time accuracy (k), as follows:

$$\int_V \left[-WU' + \frac{\partial W}{\partial r} A' + \frac{1}{r}\frac{\partial W}{\partial \theta} B' + \frac{\partial W}{\partial z} C' + W\frac{D'}{r} \right] dV = \int_S WE' dS \qquad \text{(B1.1)}$$

where

$$U' = \begin{bmatrix} U'_c \\ U'_r \\ U'_\theta \\ U'_z \end{bmatrix} = \begin{bmatrix} \frac{1}{\Delta t}\left(\alpha_0 \rho^t + \sum_{i=1}^{k} \alpha_i \rho^{t-i\Delta t} \right) \\ \frac{1}{\Delta t}\left(\alpha_0 (\rho u_r)^t + \sum_{i=1}^{k} \alpha_i (\rho u_r)^{t-i\Delta t} \right) \\ \frac{1}{\Delta t}\left(\alpha_0 (\rho u_\theta)^t + \sum_{i=1}^{k} \alpha_i (\rho u_\theta)^{t-i\Delta t} \right) \\ \frac{1}{\Delta t}\left(\alpha_0 (\rho u_z)^t + \sum_{i=1}^{k} \alpha_i (\rho u_z)^{t-i\Delta t} \right) \end{bmatrix} \qquad \text{(B1.2)}$$

$$A' = \begin{bmatrix} A'_c \\ A'_r \\ A'_\theta \\ A'_z \end{bmatrix} = \begin{bmatrix} \rho u_r \\ \rho u_r^2 + p - \sigma_{rr} \\ \rho u_\theta u_r - \sigma_{\theta r} \\ \rho u_z u_r - \sigma_{zr} \end{bmatrix}^t \qquad \text{(B1.3)}$$

$$B' = \begin{bmatrix} B'_c \\ B'_r \\ B'_\theta \\ B'_z \end{bmatrix} = \begin{bmatrix} \rho u_\theta \\ \rho u_r u_\theta - \sigma_{r\theta} \\ \rho u_\theta^2 + p - \sigma_{\theta\theta} \\ \rho u_z u_\theta - \sigma_{z\theta} \end{bmatrix}^t \qquad \text{(B1.4)}$$

$$C' = \begin{bmatrix} C'_c \\ C'_r \\ C'_\theta \\ C'_z \end{bmatrix} = \begin{bmatrix} \rho u_z \\ \rho u_r u_z - \sigma_{rz} \\ \rho u_\theta u_z - \sigma_{\theta z} \\ \rho u_z^2 + p - \sigma_{zz} \end{bmatrix}^t \tag{B1.5}$$

$$D' = \begin{bmatrix} D'_c \\ D'_r \\ D'_\theta \\ D'_z \end{bmatrix} = \begin{bmatrix} 0 \\ -\rho(u_\theta + \Omega r)^2 - p + \sigma_{\theta\theta} \\ \rho u_r (u_\theta + 2\Omega r) - \sigma_{r\theta} \\ 0 \end{bmatrix}^t \tag{B1.6}$$

$$E' = \begin{bmatrix} E'_c \\ E'_r \\ E'_\theta \\ E'_z \end{bmatrix} = \begin{bmatrix} (\rho \vec{V} \bullet \vec{n}) \\ (\rho u_r^2 + p - \sigma_{rr})\frac{rd\theta dz}{dS} + (\rho u_r u_\theta - \sigma_{r\theta})\frac{drdz}{dS} + (\rho u_r u_z - \sigma_{rz})\frac{rdrd\theta}{dS} \\ (\rho u_\theta u_r - \sigma_{\theta r})\frac{rd\theta dz}{dS} + (\rho u_\theta^2 + p - \sigma_{\theta\theta})\frac{drdz}{dS} + (\rho u_\theta u_z - \sigma_{\theta z})\frac{rdrd\theta}{dS} \\ (\rho u_z u_r - \sigma_{zr})\frac{rd\theta dz}{dS} + (\rho u_z u_\theta - \sigma_{z\theta})\frac{drdz}{dS} + (\rho u_z^2 + p - \sigma_{zz})\frac{rdrd\theta}{dS} \end{bmatrix}^t$$

B.2 Newton Linearization

The terms of the discretized matrix and residual equations (2.24-2.27) are written in detail below:

element influence matrices and residual from r-momentum equation

$$\begin{aligned} \left[k^{\rho u_r}{}_{ij}\right]_{\rho u_r} = \int_V \Bigg[& \frac{\alpha_0}{\Delta t} W_i N_j - N_j \left(2u_r^n \frac{\partial W_i}{\partial r} + u_\theta^n \frac{1}{r}\frac{\partial W_i}{\partial \theta} + u_z^n \frac{\partial W_i}{\partial r} \right) \\ & + \frac{\mu}{Re\rho_j}\left(\frac{4}{3}\frac{\partial W_i}{\partial r}\frac{\partial N_j}{\partial r} + \frac{1}{r^2}\frac{\partial W_i}{\partial \theta}\frac{\partial N_j}{\partial \theta} + \frac{\partial W_i}{\partial z}\frac{\partial N_j}{\partial z} \right) \\ & + \frac{2}{3}\frac{\mu}{Re\rho_j}\left(-\frac{N_j}{r}\frac{\partial W_i}{\partial r} - \frac{W_i}{r}\left(\frac{\partial N_j}{\partial r} - 2\frac{N_j}{r} \right) \right) \\ & + \left(W_i^{SHK} + W_i^{SUPG} \right)(CONV)^n - W_i^{SUPG} N_j \left(\frac{\partial u_r}{\partial r} \right)^n \Bigg] dV \end{aligned} \tag{B2.1}$$

$$\left[k^{\rho u_\theta}{}_{ij}\right]_{\rho u_r} = -\int_V \left[N_j u_r^n \frac{1}{r}\frac{\partial W_i}{\partial \theta} + \frac{1}{r}\frac{\mu}{Re\rho_j}\left(\frac{2}{3}\frac{\partial W_i}{\partial r}\frac{\partial N_j}{\partial \theta} - \frac{\partial W_i}{\partial \theta}\frac{\partial N_j}{\partial r}\right) + \frac{\mu}{Re\rho_j}\frac{N_j}{r}\frac{1}{r}\frac{\partial W_i}{\partial \theta} + 2\frac{W_i}{r}\left(N_j u_\theta^n - \frac{2}{3}\frac{\mu}{Re\rho_j}\frac{\partial N_j}{\partial \theta}\right) - W_i^{SUPG} N_j \frac{1}{r}\left(\frac{\partial u_r}{\partial \theta}\right)^n \right] dV \qquad \text{(B2.2)}$$

$$\left[k^{\rho u_z}{}_{ij}\right]_{\rho u_r} = -\int_V \left[+ N_j u_r^n \frac{\partial W_i}{\partial z} + \frac{\mu}{Re\rho_j}\left(\frac{2}{3}\frac{\partial W_i}{\partial r}\frac{\partial N_j}{\partial z} - \frac{\partial W_i}{\partial z}\frac{\partial N_j}{\partial r}\right) + \frac{2}{3}\frac{\mu}{Re\rho_j}\frac{\partial N_j}{\partial z}\frac{W_i}{r} - W_i^{SUPG} N_j \left(\frac{\partial u_r}{\partial z}\right)^n \right] dV \qquad \text{(B2.3)}$$

$$Res_{\rho u_r}^n = \sum_{e=1}^{nelem} \int_V \left\{ - W_i U_r' + A_r' \frac{\partial W_i}{\partial r} + B_r' \frac{1}{r}\frac{\partial W_i}{\partial \theta} + C_r' \frac{\partial W_i}{\partial z} + W_i \frac{D_r'}{r} - \frac{1}{r} W_i^{SUPG}\left(-\rho\Omega^2 r^2 - 2r\Omega\rho u_\theta\right) - (ZMOM) W_i^{SUPG} - (ZCONV) W_i^{SHK} \right\} dV - \int_S W_i \left\{ A_r' n_r + B_r' n_\theta + C_r' n_z \right\} dS \qquad \text{(B2.4)}$$

element influence matrices and residual from θ-momentum equation:

$$\left[k^{\rho u_r}{}_{ij}\right]_{\rho u_\theta} = -\int_V \left[N_j u_\theta^n \frac{\partial W_i}{\partial r} + \frac{\mu}{Re\rho_j}\frac{1}{r}\left(\frac{2}{3}\frac{\partial W_i}{\partial \theta}\frac{\partial N_j}{\partial r} - \frac{\partial W_i}{\partial r}\frac{\partial N_j}{\partial \theta}\right) - \frac{4}{3}\frac{\mu}{Re\rho_j}\frac{N_j}{r}\frac{\partial W_i}{\partial r} + \frac{W_i}{r}\left(-N_j u_\theta^n + \frac{\mu}{Re\rho_j}\frac{1}{r}\left(\frac{\partial N_j}{\partial \theta} - \frac{4}{3}N_j\right)\right) - 2\Omega N_j\left(W_i + W_i^{SUPG}\right) - W_i^{SUPG} N_j \left(\frac{\partial u_r}{\partial r}\right)^n \right] dV \qquad \text{(B2.5)}$$

$$\left[k^{\rho u_\theta}{}_{ij}\right]_{pu_\theta} = \int_V \left[\frac{\alpha_0}{\Delta t}(W_i N_j) - N_j\left(2u_\theta^n \frac{1}{r}\frac{\partial W_i}{\partial \theta} + u_r^n \frac{\partial W_i}{\partial r} + u_z^n \frac{\partial W_i}{\partial z}\right) \right.$$
$$+ \frac{\mu}{Re\rho_j}\left(\frac{4}{3}\frac{1}{r^2}\frac{\partial W_i}{\partial \theta}\frac{\partial N_j}{\partial \theta} + \frac{\partial W_i}{\partial r}\frac{\partial N_j}{\partial r} + \frac{\partial W_i}{\partial z}\frac{\partial N_j}{\partial z}\right)$$
$$- \frac{\mu}{Re\rho_j}\frac{N_j}{r}\frac{\partial W_i}{\partial r} + \frac{W_i}{r}\left(N_j u_r^n - \frac{\mu}{Re\rho_j}\left(\frac{\partial N_j}{\partial r} - \frac{N_j}{r}\right)\right)$$
$$\left. + \left(W_i^{SHK} + W_i^{SUPG}\right)(CONV)^n - W_i^{SUPG} N_j\left(\frac{1}{r}\frac{\partial u_\theta}{\partial \theta}\right)^n \right] dV \qquad \text{(B2.6)}$$

$$\left[k^{\rho u_z}{}_{ij}\right]_{pu_\theta} = -\int_V \left[N_j u_\theta^n \frac{\partial W_i}{\partial z} + \frac{\mu}{Re\rho_j}\frac{1}{r}\left(\frac{2}{3}\frac{\partial W_i}{\partial \theta}\frac{\partial N_j}{\partial z} - \frac{\partial W_i}{\partial z}\frac{\partial N_j}{\partial \theta}\right) \right.$$
$$\left. - W_i^{SUPG} N_j\left(\frac{\partial u_\theta}{\partial z}\right)^n \right] dV \qquad \text{(B2.7)}$$

$$Res_{\rho u_\theta}^n = \sum_{e=1}^{nelem} \int_V \left\{ -W_i U'_\theta + A'_\theta \frac{\partial W_i}{\partial r} + B'_\theta \frac{1}{r}\frac{\partial W_i}{\partial \theta} + C'_\theta \frac{\partial W_i}{\partial z} + W_i \frac{D'_\theta}{r} \right.$$
$$\left. - \frac{1}{r} W_i^{SUPG}\left[2\Omega r \rho u_r\right] - (\theta MOM) W_i^{SUPG} - (\theta CONV) W_i^{SHK} \right\} dV \qquad \text{(B2.8)}$$
$$- \int_S W_i \left\{ A'_\theta n_r + B'_\theta n_\theta + C'_\theta n_z \right\} dS$$

<u>element influence matrices and residual from z-momentum equation:</u>

$$\left[k^{\rho u_r}{}_{ij}\right]_{pu_z} = -\int_V \left[N_j u_z^n \frac{\partial W_i}{\partial r} + \frac{\mu}{Re\rho_j}\left(\frac{2}{3}\frac{\partial W_i}{\partial z}\frac{\partial N_j}{\partial r} - \frac{\partial W_i}{\partial r}\frac{\partial N_j}{\partial z}\right) \right.$$
$$+ \frac{2}{3}\frac{\mu}{Re\rho_j}\frac{N_j}{r}\frac{\partial W_i}{\partial z} - \frac{1}{r}\left(W_i + W_i^{SUPG}\right)\left(N_j u_z^n - \frac{\mu}{Re\rho_j}\frac{\partial N_j}{\partial z}\right)$$
$$\left. - W_i^{SUPG} N_j\left(\frac{\partial u_z}{\partial r}\right)^n \right] dV \qquad \text{(B2.9)}$$

$$\left[k^{\rho u_\theta}{}_{ij}\right]_{pu_z} = -\int_V \left[N_j u_z^n \frac{1}{r}\frac{\partial W_i}{\partial \theta} + \frac{\mu}{Re\rho_j}\frac{1}{r}\left(\frac{2}{3}\frac{\partial W_i}{\partial z}\frac{\partial N_j}{\partial \theta} - \frac{\partial W_i}{\partial \theta}\frac{\partial N_j}{\partial z}\right) - W_i^{SUPG} N_j \frac{1}{r}\left(\frac{\partial u_z}{\partial \theta}\right)^n \right] dV \tag{B2.10}$$

$$\begin{aligned}\left[k^{\rho u_z}{}_{ij}\right]_{pu_z} = \int_V \Bigg[& \frac{\alpha_0}{\Delta t}(W_i N_j) - N_j\left(2u_z^n\frac{\partial W_i}{\partial z} + u_r^n\frac{\partial W_i}{\partial r} + u_\theta^n\frac{1}{r}\frac{\partial W_i}{\partial z}\right) \\ & + \frac{\mu}{Re\rho_j}\left(\frac{4}{3}\frac{\partial W_i}{\partial z}\frac{\partial N_j}{\partial z} + \frac{\partial W_i}{\partial r}\frac{\partial N_j}{\partial r} + \frac{1}{r^2}\frac{\partial W_i}{\partial \theta}\frac{\partial N_j}{\partial \theta}\right) \\ & + \frac{2}{r}W_i^{SUPG}\left(N_j u_r^n - \frac{\mu}{Re\rho_j}\frac{\partial N_j}{\partial r}\right) + \frac{W_i}{r}\left(N_j u_r^n - \frac{\mu}{Re\rho_j}\frac{\partial N_j}{\partial r}\right) \\ & + \left(W_i^{SHK} + W_i^{SUPG}\right)(CONV)^n - W_i^{SUPG} N_j\left(\frac{\partial u_z}{\partial z}\right)^n \Bigg] dV\end{aligned} \tag{B2.11}$$

$$\begin{aligned}Res^n_{\rho u_z} = \sum_{e=1}^{nelem}\int_V \{ & -W_i U_z' + A_z'\frac{\partial W_i}{\partial r} + B_z'\frac{1}{r}\frac{\partial W_i}{\partial \theta} + C_z'\frac{\partial W_i}{\partial z} + W_i\frac{D_z'}{r} \\ & - (ZMOM)W_i^{SUPG} - (ZCONV)W_i^{SHK}\} dV \\ & - \int_S W_i\{A_z' n_r + B_z' n_\theta + C_z' n_z\} dS\end{aligned} \tag{B2.12}$$

where

$$W_i^{SUPG} = \tau_{SUPG}\left(u_r\frac{\partial W_i}{\partial r} + \frac{u_\theta}{r}\frac{\partial W_i}{\partial \theta} + u_z\frac{\partial W_i}{\partial z}\right) \tag{B2.13}$$

$$W_i^{SHK} = \tau_{SHK}\left(u_r\frac{\partial W_i}{\partial r} + \frac{u_\theta}{r}\frac{\partial W_i}{\partial \theta} + u_z\frac{\partial W_i}{\partial z}\right) \tag{B2.14}$$

$$RCONV = u_r\frac{\partial u_r}{\partial r} + \frac{u_\theta}{r}\frac{\partial u_r}{\partial \theta} + u_z\frac{\partial u_r}{\partial z} \tag{B2.15}$$

$$RMOM = \rho\frac{\partial u}{\partial t} + u_r\frac{\partial u_r}{\partial r} + \frac{u_\theta}{r}\frac{\partial u_r}{\partial \theta} + u_z\frac{\partial u_r}{\partial z} + \frac{\partial p}{\partial r} \tag{B2.16}$$

$$\theta CONV = u_r\frac{\partial u_\theta}{\partial r} + \frac{u_\theta}{r}\frac{\partial u_\theta}{\partial \theta} + u_z\frac{\partial u_\theta}{\partial z} \tag{B2.17}$$

$$\theta MOM = \rho\frac{\partial v}{\partial t} + u_r\frac{\partial u_\theta}{\partial r} + \frac{u_\theta}{r}\frac{\partial u_\theta}{\partial \theta} + u_z\frac{\partial u_\theta}{\partial z} + \frac{1}{r}\frac{\partial p}{\partial \theta} \quad \text{(B2.18)}$$

$$ZCONV = u_r\frac{\partial u_z}{\partial r} + \frac{u_\theta}{r}\frac{\partial u_z}{\partial \theta} + u_z\frac{\partial u_z}{\partial z} \quad \text{(B2.19)}$$

$$ZMOM = \rho\frac{\partial w}{\partial t} + u_r\frac{\partial u_z}{\partial r} + \frac{u_\theta}{r}\frac{\partial u_z}{\partial \theta} + u_z\frac{\partial u_z}{\partial z} + \frac{\partial p}{\partial z} \quad \text{(B2.20)}$$

$$CONV = u_r\frac{\partial N_j}{\partial r} + \frac{u_\theta}{r}\frac{\partial N_j}{\partial \theta} + u_z\frac{\partial N_j}{\partial z} \quad \text{(B2.21)}$$

Appendix C

Numerical Discretization of the Energy Equation

The weak Galerkin formulation, time discretization, and Newton linearization of the energy equation (2.4) will be demonstrated. Equation (2.4) is first multiplied by a weight function, *W*, which is identical to the interpolation function, and then integrated over the domain:

$$\int_V \left\{ \rho \frac{DH_0}{Dt} - Ec \frac{\partial p}{\partial t} - \nabla \bullet \left(\frac{\kappa}{PrRe} \nabla T \right) - \nabla \bullet \left(\frac{Ec}{Re} \bar{V} \sigma_{ij} \right) \right\} W dV = 0 \tag{C.1}$$

After integration by parts, the weak Galerkin form of equation (C.1) can be written as:

$$\begin{aligned} &\int_V \left\{ \left[\rho \frac{\partial H_0}{\partial t} - Ec \frac{\partial p}{\partial t} + \rho \bar{V} \bullet \nabla H_0 \right] W + \left[\frac{\kappa}{PrRe} \nabla T + \frac{Ec}{Re} \bar{V} \sigma_{ij} \right] \bullet \nabla W \right\} dV \\ &- \int_S \left\{ \left[\frac{\kappa}{PrRe} \nabla T + \frac{Ec}{Re} \bar{V} \sigma_{ij} \right] \bullet \bar{n} \right\} W dS = 0 \end{aligned} \tag{C.2}$$

The SUPG form of the energy equation can be expanded as:

$$\begin{aligned} \int_V \Bigg\{ &\left[\rho \frac{\partial H_0}{\partial t} - Ec \frac{\partial p}{\partial t} + \rho \bar{V} \bullet \nabla H_0 \right] \left[W + W^{SUPG} \right] \\ &+ \left[\frac{\kappa}{PrRe} \nabla T + \frac{Ec}{Re} \bar{V} \sigma_{ij} \right] \bullet \nabla W \Bigg\} dV \\ &- \int_S \left\{ \left[\frac{\kappa}{PrRe} \nabla T + \frac{Ec}{Re} \bar{V} \sigma_{ij} \right] \bullet \bar{n} \right\} W dS = 0 \end{aligned} \tag{C.3}$$

The time-dependent terms of equation (C.3) is then discretized using Gear scheme as follows:

$$\int_V \left\{ \left[\rho \frac{1}{\Delta t} \left(\alpha_0 H_0^t + \sum_{i=1}^{k} \alpha_i H_0^{t-i\Delta t} \right) - Ec \frac{1}{\Delta t} \left(\alpha_0 p^t + \sum_{i=1}^{k} \alpha_i p^{t-i\Delta t} \right) \right. \right.$$
$$\left. + \left(\rho \bar{V} \bullet \nabla H_0 \right) \right] \left[W + W^{SUPG} \right] + \left[\frac{\kappa}{PrRe} \nabla T + \frac{Ec}{Re} \bar{V} \sigma_{ij} \right]^t \bullet \nabla W \Big\} dV \qquad (C.4)$$
$$- \int_S \left\{ \left[\frac{\kappa}{PrRe} \nabla T + \frac{Ec}{Re} \bar{V} \sigma_{ij} \right]^t \bullet \vec{n} \right\} W dS = 0$$

The Newton method is applied whereby the total enthalpy is expressed in delta form, $\Delta H_0 = H_0{}^{n+1} - H_0{}^n$, and the second order terms are neglected. Upon substitution of equations (2.10) and (2.12) into the Newton linearized equation, the delta form of the energy equation is assembled, over the elements of the domain, in terms of the nodal unknown, ΔH_0:

$$\sum_{e=1}^{nelem} \left[\sum_{j=1}^{ndperl} \left[k_{ij}^{H_0} \right]_{H_0} \Delta (H_0)_j \right] = -Res_{H_0} \qquad (C.5)$$

where the element influence matrices and residual vectors from the energy equation take the form:

$$\left[k_{ij}^{H_0} \right]_{H_0} = \int_V \left\{ \left(\frac{\alpha_0}{\Delta t} \rho N_j + \rho u_r \frac{\partial N_j}{\partial r} + \rho u_\theta \frac{1}{r} \frac{\partial N_j}{\partial \theta} + \rho u_z \frac{\partial N_j}{\partial z} \right) \left(W_i + W^{SUPG} \right) \right.$$
$$+ \left(e_1 \Delta r + \frac{\kappa}{PrRe} \left(\frac{\partial N_j}{\partial r} \frac{\partial W_i}{\partial r} \right) \right) + \left(e_2 r \Delta \theta + \frac{\kappa}{PrRe} \left(\frac{1}{r^2} \frac{\partial N_j}{\partial \theta} \frac{\partial W_i}{\partial \theta} \right) \right.$$
$$\left. \left. + \left(e_3 \Delta z + \frac{\kappa}{PrRe} \left(\frac{\partial N_j}{\partial z} \frac{\partial W_i}{\partial z} \right) \right) \right\} dV \qquad (C.6)$$

$$
\begin{aligned}
Res_{H_0} = \int_V \Bigg\{ \Bigg[\rho \frac{1}{\Delta t}\left(\alpha_0 H_0^t + \sum_{i=1}^{k} \alpha_i H_0^{t-i\Delta t} \right) - Ec \frac{1}{\Delta t}\left(\alpha_0 p^t + \sum_{i=1}^{k} \alpha_i p^{t-i\Delta t} \right) \\
+ \left(\rho \bar{V} \bullet \nabla H_0 \right) \Bigg] \left[W + W^{SUPG} \right] + \left[\frac{\kappa}{PrRe} \nabla T + \frac{Ec}{Re} \bar{\bar{V}} \sigma_{ij} \right]^t \bullet \nabla W \\
+ (e_1 \Delta r) \frac{\partial W}{\partial r} \frac{\partial H_0}{\partial r} + (e_2 r \Delta \theta) \frac{1}{r^2} \frac{\partial W}{\partial \theta} \frac{\partial H_0}{\partial \theta} + (e_3 \Delta z) \frac{\partial W}{\partial z} \frac{\partial H_0}{\partial z} \Bigg\} dV \\
- \int_S \left\{ \left[\frac{\kappa}{PrRe} \nabla T + \frac{Ec}{Re} \bar{\bar{V}} \sigma_{ij} \right]^t \bullet \bar{n} \right\} W dS = 0
\end{aligned}
\tag{C.7}
$$

Appendix D

Weak Galerkin Formulation of the Time-Inclined Navier-Stokes Equations

Consider the following coordinate transformation from (r,θ,z,t), the physical coordinated, to (r',θ',z',t'), the computational coordinates in which t' is constant on each computational time level.

$$\begin{aligned} r' &= r \\ \theta' &= \theta \\ z' &= z \\ t' &= t - \lambda\theta \end{aligned} \tag{D.1}$$

and

$$\lambda = \begin{cases} \dfrac{\Delta T}{\theta_S} & \text{stator} \\ \dfrac{\Delta T}{\theta_R} & \text{rotor} \end{cases} \qquad \Delta T = T_R - T_S = \frac{\theta_R - \theta_S}{\Omega} \tag{D.2}$$

where λ is the inclination parameter, ΔT is the time lag, and θ_S and θ_R denote the stator pitch and the rotor pitch, respectively.

Applying this transformation into Eq. (A.1) and dropping the ' symbol from the equation yields

$$\int_V W\left[\frac{\partial}{\partial t}(Q)+\frac{1}{r}\frac{\partial}{\partial r}(rA)+\frac{1}{r}\frac{\partial}{\partial \theta}(B)+\frac{\partial}{\partial r}(C)+\frac{D}{r}\right]dV = 0 \tag{D.3}$$

where

$$Q = U - \frac{\lambda}{r} B \tag{D.4}$$

In *NS3D,* the choice was to solve for the variable U and this requires a minor modification to the principal algorithm with equal pitches.

The time term $\frac{\partial Q}{\partial t}$ in equation (D.3) can be written as

$$\frac{\partial Q}{\partial t} = \frac{\partial Q}{\partial U}\frac{\partial U}{\partial t} = \left(1 - \frac{\lambda}{r}\frac{\partial B}{\partial U}\right)\frac{\partial U}{\partial t} \tag{D.5}$$

where

$$\left[I - \frac{\partial B}{\partial U}\right] = \begin{bmatrix} 1 & 0 & -\frac{\lambda}{r} & 0 \\ \frac{\lambda}{r}u_r u_\theta & \left(1 - \frac{\lambda}{r}u_\theta\right) & -\frac{\lambda}{r}u_r & 0 \\ \frac{\lambda}{r}\left(u_\theta^2 - RT\right) & 0 & \left(1 - 2\frac{\lambda}{r}u_\theta\right) & 0 \\ \frac{\lambda}{r}u_z u_\theta & 0 & -\frac{\lambda}{r}u_z & \left(1 - \frac{\lambda}{r}u_\theta\right) \end{bmatrix} \tag{D.6}$$

Note that the matrix in (D.6) is derived based on the Euler system of equations for momentum and continuity. The energy equation is solved in a segregated manner and hence the static temperature is lagged by one Newton iteration for a given time level.

The implementation of this modification in the code is extremely simple. It is achieved by modifying the definition of the time terms in the governing flow equations with equal pitches.

Appendix E

Interpolation Procedure at the Rotor-Stator Interface For Equal and Unequal Pitches

Equal Pitches

The rotor grid location at an instant of time t is given by

$$\theta_r(t) = \theta_o + \Omega t \tag{E.1}$$

At every time step the rotor moves by $\Omega\Delta t$ and the new position of the rotor is established with respect to that of the stator by satisfying the following equation

$$\theta_r(t) = \theta_s(t) + \frac{2\pi}{N_b} n \tag{E.2}$$

where N_b is the blade count and n = 0,1,.., N_b is the stator passage index.

Note that the 2nd term on the right hand side of equation (3) is introduced through the spatial periodicity of the flow problem.

Unequal Pitches Algorithm

Viewed in the stator frame of reference as shown in figure (1.7) the rotor pitch lines up with the stator pitch and thus both pitches are identical. For proper interpolation of flow properties across the interface the rotor grid is scaled in the pitchwise direction. The scale factor is the pitch ratio and the new theta-coordinate of the rotor

$$\theta_r(\text{new}) = \frac{P_S}{P_R}\theta_r(\text{old}) \tag{E.3}$$

after scaling becomes identical to that of the stator.

When one transforms equation (E.1) into the time inclined plane

$$\theta'_r(t') = \theta'_o + \Omega(t' + \lambda_r\theta'_r) = \theta'_o + \Omega t' + \Omega\lambda_r\theta'_r \tag{E.4}$$

Equation (E.4) can be recast as follows

$$(1 - \Omega\lambda_r)\theta'_r(t') = \frac{P_S}{P_R}\theta'_r(t') = \theta'_o + \Omega t' \tag{E.5}$$

Substituting equation (E.3) into (E.5) yields the desired equation

$$\theta'_r(\text{new}) = \theta'_o + \Omega t' \tag{E.6}$$

Equation (E.6) is the equivalent of equation (E.1). At each time step, the rotor moves by $\Omega\Delta t'$ and the rotor pitch is identical to the stator pitch.

On an inclined plane, the angular pitch of the rotor is exactly the same as the stator. The interpolation at the interface is exactly as it would be in ordinary time if the two blade pitches were identical.